

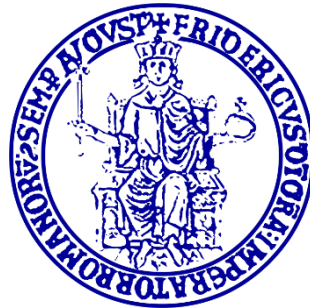
La borsa di dottorato è stata cofinanziata con risorse del  
Programma Operativo Nazionale Ricerca e Innovazione 2014-2020 (CCI 2014IT16M2OP005),  
Fondo Sociale Europeo, Azione I.1 “Dottorati Innovativi con caratterizzazione Industriale”



UNIONE EUROPEA  
Fondo Sociale Europeo



Ministero dell'Università  
e della Ricerca



# Università degli Studi di Napoli “Federico II”

DOTTORATO DI RICERCA IN  
**FISICA**

Ciclo XXXIV

Coordinatore: prof. Salvatore Capozziello

## Gold decorated magnetic nanoparticles for biosensing

Settore Scientifico Disciplinare FIS/07

**Dottorando**  
Raffaele CAMPANILE

**Tutor**  
Prof. Raffaele VELOTTA  
Prof. Vincenzo IANNOTTI

Anni 2019/2021



# Contents

|   |           |
|---|-----------|
| <b>List of abbreviations .....</b>                      | <b>7</b>  |
| <b>Introduction.....</b>                                | <b>11</b> |
| <b>Chapter 1. Principles of Biosensing.....</b>         | <b>15</b> |
| 1.1 Biosensors .....                                    | 16        |
| 1.1.1 Classification.....                               | 17        |
| 1.1.2 Examples of applications .....                    | 19        |
| 1.2 Surface functionalization.....                      | 20        |
| 1.2.1 Antibodies as bioreceptors .....                  | 21        |
| 1.2.2 Conventional immobilization techniques.....       | 23        |
| 1.2.3 Photochemical Immobilization Technique (PIT)..... | 24        |
| 1.3 Nanoparticles.....                                  | 26        |
| 1.3.1 Gold nanoparticles .....                          | 26        |
| 1.3.2 Gold decorated magnetic nanoparticles .....       | 27        |
| <b>Chapter 2. Magnetoelastic biosensor.....</b>         | <b>30</b> |
| 2.1 Overview .....                                      | 31        |
| 2.2 The theory of magnetoelasticity .....               | 33        |
| 2.2.1 Metallic glasses .....                            | 33        |
| 2.2.2 Physical origin of magnetoelasticity.....         | 34        |
| 2.2.3 Thermodynamic approach.....                       | 35        |
| 2.2.4 Acoustic wave equation in air .....               | 38        |
| 2.2.5 Oscillations in liquids.....                      | 39        |
| 2.2.6 Mass sensitivity.....                             | 40        |

|                   |   |           |
|-------------------|---|-----------|
| 2.3               | Materials and methods.....  | 41        |
| 2.3.1             | ME sensors fabrication.....   | 41        |
| 2.3.2             | Antibodies immobilization.....  | 42        |
| 2.3.3             | Synthesis of AuNPs .....  | 42        |
| 2.3.4             | Au coating of Fe <sub>3</sub> O <sub>4</sub> MNPs .....                                   | 43        |
| 2.3.5             | Experimental setup.....   | 43        |
| 2.3.6             | Experimental procedure .....  | 44        |
| 2.4               | Results .....   | 45        |
| 2.4.1             | Characterization of Fe <sub>3</sub> O <sub>4</sub> @Au MNPs.....                          | 45        |
| 2.4.2             | Comparison between AuNPs and Fe <sub>3</sub> O <sub>4</sub> @Au MNPs .....                | 47        |
| 2.4.3             | Detection of Human IgG.....   | 49        |
| 2.4.4             | Specificity assay.....  | 50        |
| 2.5               | Discussion .....  | 50        |
| 2.5.1             | Modeling the interaction among ME sensor and Fe <sub>3</sub> O <sub>4</sub> @Au MNPs..... | 50        |
| 2.5.2             | Future research directions .....  | 54        |
| 2.6               | Conclusions .....   | 55        |
| <b>Chapter 3.</b> | <b>Colorimetric biosensor .....</b>   | <b>57</b> |
| 3.1               | Overview .....  | 58        |
| 3.2               | The theory of plasmonic.....  | 60        |
| 3.2.1             | Maxwells' equations .....   | 60        |
| 3.2.2             | Localized Surface Plasmon Resonance (LSPR) .....  | 63        |
| 3.2.3             | Mie's and Gans' theories .....  | 65        |
| 3.2.4             | Nanoparticles-based sensor.....   | 71        |
| 3.3               | Materials and methods.....  | 74        |
| 3.3.1             | Materials.....  | 74        |
| 3.3.2             | Synthesis of Fe <sub>3</sub> O <sub>4</sub> @Au MNPs.....                                 | 74        |
| 3.3.3             | Functionalization of Fe <sub>3</sub> O <sub>4</sub> @Au MNPs.....                         | 75        |
| 3.3.4             | Rotating magnetic field.....  | 76        |

|                   |  |           |
|-------------------|--|-----------|
| 3.4               | Results .....  | 76        |
| 3.4.1             | Characterization of Fe <sub>3</sub> O <sub>4</sub> @Au MNPs..... | 76        |
| 3.4.2             | Detection of glyphosate .....                                    | 78        |
| 3.4.3             | Specificity assay against AMPA.....                              | 80        |
| 3.5               | Discussion .....   | 81        |
| 3.5.1             | Dose-response curve .....  | 81        |
| 3.5.2             | Micromixing modelling .....                                      | 82        |
| 3.6               | Conclusions .....  | 85        |
| <b>Chapter 4.</b> | <b>Magneto resistive biosensor .....</b>                         | <b>87</b> |
| 4.1               | Overview .....   | 88        |
| 4.2               | The magneto resistive effect.....                                | 90        |
| 4.2.1             | Spin Valve sensors .....   | 90        |
| 4.2.2             | MNPs detection in DC mode .....                                  | 91        |
| 4.2.3             | Considerations on sensitivity .....                              | 94        |
| 4.3               | Materials and Methods .....                                      | 95        |
| 4.3.1             | Reagents and materials.....                                      | 95        |
| 4.3.2             | Synthesis of CSMPs.....  | 95        |
| 4.3.3             | MR sensors fabrication and cleaning .....                        | 96        |
| 4.3.4             | Functionalization protocol .....                                 | 97        |
| 4.3.5             | Biochip experimental setup.....                                  | 98        |
| 4.3.6             | Experimental procedure .....                                     | 99        |
| 4.3.7             | Simulation workspace .....                                       | 102       |
| 4.4               | CSMPs Characterization .....                                     | 103       |
| 4.4.1             | Morphology.....  | 103       |
| 4.4.2             | Optical response .....   | 103       |
| 4.4.3             | Surface charge properties.....                                   | 104       |
| 4.4.4             | Hydrodynamic properties.....                                     | 105       |
| 4.4.5             | Magnetic properties.....   | 105       |

|                      |   |            |
|----------------------|---|------------|
| 4.5                  | Biosensing application .....                      | 107        |
| 4.5.1                | Detection of Human IgG in simulated samples ..... | 107        |
| 4.5.2                | Specificity assay.....                            | 107        |
| 4.6                  | Conclusions .....                                 | 108        |
| <b>Final remarks</b> | .....   | <b>110</b> |
| <b>References</b>    | .....   | <b>112</b> |

# List of abbreviations

|       |                                    |
|-------|------------------------------------|
| ABS   | Acrylonitrile butadiene styrene    |
| Abs   | Antibodies                         |
| AC    | Alternating current                |
| ACoM  | Autonomous communication module    |
| AMPA  | Aminomethylphosphonic acid         |
| AnM   | Analyzer module                    |
| AuNPs | Gold nanoparticles                 |
| BC    | Boundary condition                 |
| BSA   | Bovine serum albumin               |
| CAGR  | Compound Annual Growth Rate        |
| CSMPs | Core@satellite magnetic particles  |
| CTAB  | hexadecyltrimethylammonium bromide |
| Cys   | Cystein                            |
| DC    | Direct current                     |
| DLS   | Dynamic light scattering           |
| ELISA | Enzyme-linked immunosorbent assay  |

|        |   |
|--------|---|
| EM     | Electromagnetic                         |
| Fab    | Fragment antigen-binding                |
| f-AuNP | Functionalized-gold nanoparticle        |
| FDTD   | Finite-difference time-domain           |
| FEM    | Finite element method                   |
| FM     | Ferromagnetic                           |
| FOM    | Figure of merit                         |
| GC     | Gas chromatography                      |
| GUI    | Graphic user interface                  |
| HPLC   | High-performance liquid chromatography  |
| Ig     | Immunoglobulin                          |
| IPA    | Isopropyl alcohol                       |
| LC     | Liquid chromatography                   |
| LC-MS  | Liquid chromatography-mass spectrometry |
| LIF    | Laser induced fluorescence              |
| LOD    | Limit of detection                      |
| LSP    | Localized surface plasmon               |
| LSPR   | Localized surface plasmon resonance     |
| M      | Magnetic                                |
| ME     | Magnetoelastic                          |
| MNPs   | Magnetic nanoparticles                  |

|         |   |
|---------|---|
| MNPs@Au | Gold decorated magnetic nanoparticles               |
| MR      | Magneto resistive                                   |
| MRAM    | Magnetic random access memories                     |
| OD      | Optical density                                     |
| p.p.m   | Parts per million                                   |
| pAb     | Polyclonal antibody                                 |
| PCR     | Polymerase chain reaction                           |
| PD      | Photodetector                                       |
| PDMS    | Polydimethylsiloxane                                |
| PIT     | Photochemical immobilization technique              |
| PML     | Perfectly matched layer                             |
| POC     | Point of care                                       |
| PPPs    | Plant protection products                           |
| QCM     | Quartz Crystal Microbalance                         |
| RT      | Room temperature                                    |
| RT-PCR  | Reverse transcriptase-polymerase chain reaction (RT |
| SAM     | Self-assembled monolayer                            |
| SD      | Standard deviation                                  |
| SPM     | Sensing and processing module                       |
| SV      | Spin valve  |
| TEM     | Transmission electron microscopy                    |

|      |                               |
|------|-------------------------------|
| TFSE | Total-field scattered-field   |
| Trp  | Tryptophan                    |
| VNA  | Vector Network Analyzer       |
| VSM  | Vibrating sample magnetometer |
| WHO  | World Health Organization     |
| XRD  | X-ray diffraction             |

# Introduction

An increasing interest in nanotechnology is crossing more and more fields of application thanks to the properties of metallic nanomaterials that are enhanced by external electromagnetic fields. In particular, the development of controllable objects at the nanoscale, using magnetic fields, is an emerging and steadily-growing phenomenon because of the recent technological advances. Among the many reasons, magnetic nanostructures are redeeming great success for the benefits they bring when combined with biosensors for the detection of several analytes in clinical, food and environmental applications.

Biosensors date back to 1962 when the biochemist Leland C. Clark and his colleagues realized a device called the "enzyme electrode" that was able to detect glucose oxidase [1]. Biosensor-based approaches, including colorimetric, magnetoelastic, and magneto resistive, have been tested to complement – or even replace – the conventional methods in a variety of applications, including food safety [2] and environmental pollution monitoring [3]. The reasons why gold standard laboratory techniques such as liquid chromatography-mass spectrometry (LC-MS), reverse transcriptase-polymerase chain reaction (RT-PCR), high-performance liquid chromatography (HPLC) and the emerging enzyme-linked immunosorbent assay (ELISA), have limited applicability for routinely mass screening applications is because they are expensive and time-consuming in addition to the fact that they require well-equipped laboratory and skilled personnel. On the other hand, to date there are no other approaches that can match their exceptional performance in terms of selectivity, sensitivity, and reliability.

In this regard, biosensors are capable of rapid, practical, and affordable applications in many fields, being particularly attractive for point-of-care testing (POC) and high-throughput analysis. Therefore, the scientific community is investing many resources to improve the applicability of biosensor-based methods overcoming their difficulties in surface functionalization, complex industrial implementation and limited sensitivities [4,5]. In recent years, magnetic sensors have become increasingly popular due to the possibility of combining them with magnetic nanoparticles (MNPs).

MNPs have gained popularity due to the exceptional tunability of their magnetic properties by tailoring their shape and size [6,7] and they are moving towards multifunctional materials with a great potential for biosensors. The majority of MNPs used in biosensors are iron oxides ( $\gamma$ -Fe<sub>2</sub>O<sub>3</sub> and Fe<sub>3</sub>O<sub>4</sub>), because they have highly active surface and fast reaction kinetics [8]. MNPs can respond to a magnetic field and redisperse upon removal of the magnet when their sizes are down to nanometers [9]. For what concern their use for biosensors, their easy magnetic separation and large active surface area allow the immobilization and purification of biomolecules under a magnetic field, as well as a decrease of the matrix effect. Furthermore, MNPs can accelerate the signal transduction and amplify the target recognition, thereby improving the overall detection sensitivity of biosensors. In addition, the intrinsic properties of MNPs make them excellent magnetic probes for the signal readout for ultrasensitive convenient and real-time measurement. Finally, MNPs are particularly suitable for the integration in microfluidic devices to develop lab-on-a-chip bioassays for POC testing [10]. All these inherent merits and advantages render MNPs prominent for easy, reliable, and cost-effective detections for POC diagnostics. However, despite the enormous potential of MNPs, the low electrical conductivity and limited optical properties compromises the ability of MNPs to be the transducing element of a sensor [11]. Another challenge facing the use of MNPs in sensing is due to the large surface area to volume ratio and low surface charge at neutral pH. Because of this, MNPs dispersions typically have low stability and high tendency to non-specific aggregation. Such aggregation can be reduced with appropriate surface chemistry, which is also vital for sensing applications [12]. Therefore, MNPs for biosensing are generally composed of two parts, a magnetic core and a chemical component on the outer surface with bio-recognition properties. Nevertheless, the surfaces of most magnetic materials are not compatible with well-defined surface chemistry such as the alkanethiol system, and complex, expensive and time-consuming procedures are required to link the bioreceptors onto these bioactive surfaces. In addition, the biological layer is generally not sufficient to effectively protect the magnetic core from oxidation.

Other nanostructures that caught the attention of the scientific community include gold nanoparticles (AuNPs) [13]. AuNPs are much simpler to synthesize and have gained popularity for their surface chemistry and biocompatibility [14,15], allowing the adoption of well-known functionalization techniques to link bioreceptors onto the external surface [16]. However, unlike MNPs, AuNPs cannot be manipulated by external magnetic fields to rake the target in solution (preconcentration) or to improve liquid transport properties (nanomixing).

Recently, several protocols have been proposed to decorate MNPs with gold creating the so-called gold decorated structures (MNPs@Au) [17]. The idea behind it, is to gather in a single nanostructure all the advantages of AuNPs and MNPs. However, MNPs@Au are not routinely adopted yet because of their complex fabrication procedures and low availability on the market [17].

The aim of the work in this thesis was to propose novel effective protocols for gold coating of commercial MNPs to improve the applicability of biosensors in environmental control, food safety and clinical analysis. Three different types of gold decorated magnetic nanoparticles were designed and tested in combination with as many types of biosensors. The introduction of MNPs@Au was aimed at improving the performance of already widespread biosensing setups, narrowing the gap in terms of sensitivity and applicability with gold standard techniques.

This thesis work has been organized to provide the reader with the basic theoretical and experimental notions before delving into the innovative content. To this end, Chapter 1 briefly introduces biosensors focusing on the types of transducers exploited in the following part of the work. Then, in the context of functionalization techniques, the main advantages of Photochemical Immobilization Technique (PIT) over conventional methods are listed. In the final part of the Chapter, nanoparticles are introduced, focusing on AuNPs and MNPs@Au.

In Chapter 2 is presented a magnetoelastic (ME) biosensor for wireless detection of analytes in liquid. A new amplification protocol exploiting MNPs@Au is demonstrated to significantly enhance the sensitivity. The superiority of MNPs@Au over AuNPs, has been demonstrated by testing the ME biosensor against Human IgG in the range 0–20  $\mu\text{g}\cdot\text{mL}^{-1}$ . The experimental results show that the ME biosensor works well in water and has a rapid response time, being promising for real-time wireless detection of pathogens in liquids and for real life diagnostic purposes.

In Chapter 3 a simple, easy-to-use and efficient colorimetric immunosensor that exploits spinning MNPs@Au in a rotating magnetic field is presented. The proposed biosensor was tested against glyphosate in tap water, being able to detect the pesticide in concentration lower than the ones legally permitted in food according to several authorities. The excellent result in terms of sensitivity was achieved thanks to the adoption of MNPs@Au, as shown by the comparison made with the AuNPs based biosensor. This performance makes the colorimetric approach described in Chapter 3 an interesting tool for on-site detection or even POC diagnosis.

In Chapter 4 is reported a fast, simple and effective protocol for coating commercial MNP clusters with AuNPs. The resulting core@satellite magnetic particles (CSMPs) consist of isolated gold nanoparticles stuck onto an aggregate of individual iron oxide crystals (core). The CSMPs were used in combination with a powerful MR biochip equipped with a unique highly-portable detection platform properly designed to achieve a POC device. The biosensing setup was tested against Human IgG at concentrations of clinical interest. The novel CSMPs have an enormous potential for excellent sensing applications, especially in the target protein quantitative detection field with quick response (within 1 hour), potential multiplexing analysis (up to 6 different analytes at the same time) and signal redundancy (up to 30 measurements).

The global conclusions of the thesis work are summarized in the final remarks.



# Chapter 1. Principles of Biosensing

The thesis has been organised to gradually introduce the readers into the world of biosensing and throughout the conducted experiments. This introductory Chapter is designed to provide a foundation for later understanding the original content presented in the next three Chapters.

In **Paragraph 1.1**, the concept of a biosensor is introduced. In addition, the transduction methods exploited in this thesis are discussed along with some examples of applications. **Paragraph 1.2** focuses on surface functionalization techniques, introducing the Photochemical Immobilization Technique that has been extensively employed in this thesis. Finally, **Paragraph 1.3** briefly describes the main characteristics of gold nanoparticles and the gold decorated magnetic nanoparticles.

# 1.1 Biosensors

A biosensor is an analytical device able to convert the presence of a chemical substance into a measurable signal. It can be represented schematically as made of three elements (Figure 1.1):

1. a bioreceptor (e.g. enzymes, antibodies, aptamers, cell, receptors) that is able to selectively react and recognize biochemical elements (e.g. small molecules, bacteria, pesticides, proteins, toxins).
2. a physicochemical element (detector or transducer) which converts the recognition event into a measurable signal.
3. an electronic system (including a signal amplifier, processor and display) which analyses the signal and displays a data output.



**Figure 1.1.** Schematic representation of a biosensor.

The digital output represents the interaction between the biological component and the analyte. In general, the aim is to produce an electronic signal that is proportional to the concentration of a specific chemical or group of chemicals.

Biosensors date back to the development of the first enzyme electrode in 1962 [1]. Immobilizing enzymes on electrodes, Clark and his colleagues realized a device called the "enzyme electrode" that was able to detect glucose oxidase by using a dialysis membrane.

Since that time, the scientific community's interest in biosensors has been steadily growing. Thirty years ago, you might have read a paper on biosensors once every 2 years and the total world market was worth less than US\$ 5 million per year. Today, around 4500 papers are published on biosensors each year and worldwide sales of biosensors are worth about US\$ 13 billion (Figure 1.2a) [18]. Government funding for biosensor research has also been increasing for security, health monitoring and food safety applications. For these reasons a double-digit increase is expected for 2023 for the Compound Annual Growth Rate (CAGR) (Figure 1.2b).

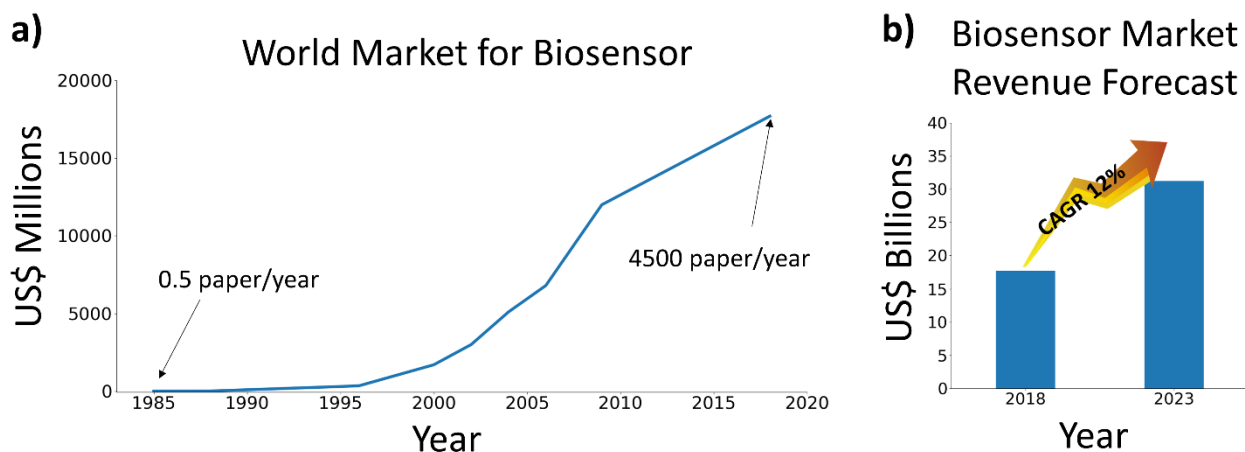


**Figure 1.2.** a) Trends in biosensor market. The global world market for biosensor is steadily increasing since the 80s as well as the interest of the scientific community. According to popular forecasts, the market will continue to grow in double digits through 2023 [18].

In order to evaluate the performance of a biosensor, the following parameters are considered:

- **Limit of detection (LOD):** the lowest concentration of an analyte that can be reliably measured in a sample.
- **Sensitivity:** the ability to distinguish between small differences in analyte concentration.
- **Linear range:** the range of analyte concentrations for which the response changes linearly.
- **Specificity:** the capability of detecting only a specific analyte in a sample containing other contaminants.
- **Reproducibility:** the ability to obtain coherent results when repeated experiments are performed.
- **Stability:** the degree to which the system is susceptible to environmental disturbances (e.g. temperature).

### 1.1.1 Classification

Generally, based on the bioreceptor-antigen interaction process, biosensors can be classified in biocatalytic (enzyme), immunological (antibody) and nucleic acid (DNA) sensors. All three biosensors presented in this thesis are based on the antibody-antigen interaction that are also called immunosensors. Moreover, biosensors are classified according to the transduction principle, which turns out to be a characterizing element. In fact, the transducer-dependent way of converting the antibody-antigen interaction into signal significantly impact the performance of the biosensor. Based on the type of the transducer, biosensors may be classified as optical, electrochemical, calorimetric, piezoelectric or magnetic. In recent years, magnetic sensors have become increasingly popular in particular due to the possibility of combining them with magnetic nanoparticles (MNPs). In this

thesis, three transduction methods were exploited for each of which a specific type of MNPs was developed. Two of the transducers presented belong to the class of magnetic sensors (magnetoelastic and magneto resistive) and the remaining one belongs to the class of optical sensors (colorimetric).

Magnetoelastic (ME) sensors are acoustic-waves/mass-based detection platforms, meaning that they rely on the principle that the output signal, generated by mechanical vibrations of the transducer, is due to mass changes on the sensing platform [19]. The most common type of magnetoelastic sensor is a ribbon-like thick-film strip made of amorphous ferromagnetic alloys, such as  $\text{Fe}_{40}\text{Ni}_{40}\text{P}_{14}\text{B}_6$  (Metglas 2826). The operating principle is based on the Joule magnetostriction of the ME material, which can vibrate longitudinally at a characteristic resonance frequency when subjected to a variable magnetic field. The adhesion of a small mass to the surface of the material involves a change of the resonance frequency, which can therefore be used as a sensing parameter. The magnetic flux generated by the elastic waves in a ME material is detectable remotely. Magnetic field telemetry enables contact-less, remote-query operation that has enabled many practical uses of the sensor platform. The main advantages of the resulting device are its cheapness, given the low production costs, and the possibility of creating a multiplexing scheme, considering the small size of the sensor [19]. To cite one of the many applications that are now widespread, ME sensors with a size of approximately  $4\text{ cm} \times 6\text{ mm} \times 25\text{ }\mu\text{m}$  are widely used as anti-theft markers. In Chapter 2 is proposed a ME biosensor based on antibody-antigen interaction for wireless detection of pathogens in liquid [20]. For the first time, the performance of this type of sensor has been improved by means of core@shell MNPs.

A colorimetric sensor based on metal nanoparticles is able to detect the color change in a colloidal suspension that is caused by changes in the refractive index of the surrounding environment and plasmon coupling between the particles [21–25]. Gold nanoparticles (AuNPs) (diameter from 15 to 35 nm) exhibiting wine-red colour with a localized surface plasmon resonance (LSPR) wavelength lying in the range 520-530 nm are the most popular for this kind of applications [26]. The aggregation of AuNPs results in a large red-shift of the LSPR peak that leads to a colour change from red to blue [21]. Such an unique feature has been exploited to develop aggregation-based colorimetric assays for detecting proteins [27], small molecules [28], inorganic ions [29], oligonucleotides [30] and viruses [31]. Colorimetric immunosensors based on colloidal solution of functionalized AuNPs are very attractive since they provide a fast and accurate response with a very high sensitivity and easiness-of-use. In Chapter 3 is proposed a nanoparticles-based biosensor for the detection of glyphosate in tap water. For the first time, instead of using simple AuNPs, the sensor was made using core@shell MNPs. This innovation has led to a significant improvement of the performance of the colorimetric sensor making it interesting for more challenging applications.

Magneto resistive (MR) sensors exploit the change of resistance under the influence of an external magnetic field. Sensors based on the MR effect have been successfully implemented thanks to the capacity of some stratified structured material to convert magnetic signals to electrical signals. So far, MR sensors have been used for a wide variety of applications, such as magnetic random-access-memory (MRAM) [32], hard disk drives [33], position sensing [34,35], pressure measurement [36,37]. MR biosensors date back to 1998 when the first application to detect a biological signal was proposed [38], since then they have been widely used in the detection of proteins, bacteria, and DNAs. The main advantages of MR biosensors are the low background noise, the high sensitivity and the stability with respect to environmental parameters (i.e. pH and temperature), as well as the possibility to detect very weak magnetic fields (nT) at room temperature [39]. In addition, nanofabrication technologies allow the integration of multiple MR sensors on a single chip. This feature makes MR sensor chips very attractive platforms for potential multiplexing measurements and biomarker panel analysis [40]. Last but not least, since MR biosensor chips can be miniaturized, they are particularly suitable to be integrated on point-of-care (POC) devices for rapid, portable and on-site diagnosis [41,42]. In Chapter 4 a high-performance MR biochip is presented. In combination with specially designed and manufactured core@satellite magnetic particles, the sensor was tested for detection of Human IgG in simulated samples.

### **1.1.2 Examples of applications**

Due to their multiple advantages (robustness, fast response, real time detection, low cost, stability, sensitivity, selectivity and reproducibility) biosensors have a variety of applications in different fields including agriculture, food industries, environmental pollution monitoring and medical diagnosis. For instance, interesting areas for biosensing are the food quality, which requires rapid and low cost methods to evaluate the presence of contaminants, and the biomedical field where real-time and in situ analysis of clinical samples are key objectives.

In recent years, food safety has become an issue of public importance due to the enormous changes that have affected the food system characterized no longer by a close relationship between production and consumption but by the globalization of food, i.e. trade, traveling goods and exotic products from countries where food and agricultural legislation may not be as stringent as the European one. Food safety is really guaranteed only if food, before being released on the market, is subjected to precise controls following proper practices which establish a series of prevention measures. If these measures are not correctly applied, food can be contaminated by various pathogenic microorganisms (bacteria, viruses and parasites) capable of causing a high number of infections, sometimes even fatal. The incidence of these infections has significantly increased in recent years and, currently, foodborne diseases, but also waterborne diseases, are ranked among the most significant problems in the world

as they negatively affect human health. Some infections can result from untreated water or water contaminated by human or animal sewage, others from common foods such as milk, cheese, meat, chicken, fruits and raw vegetables contaminated during the preparation process. Thus, monitoring water and food is essential to ensure that they are safe and fit for consumption, meaning that both pathogenic microorganisms and their toxins are absent. This is crucial to preserve the well-being of the population, but despite advances in health care, such diseases are still a global problem to such an extent that the World Health Organization has placed food safety among its top eleven priorities. In order to prevent the growth and evolution of food- and water-borne diseases, it is important to develop new rapid and cost-effective technologies for the detection and quantification of the most common pathogens.

All three biosensors developed in this thesis can be applied to food safety or water quality control problems. In particular, the capability of the colorimetric biosensor presented in Chapter 3 to deal with this type of problem was directly demonstrated with the detection of glyphosate in tap water.

## **1.2 Surface functionalization**

An important component of a biosensor device is the biological recognition element, or bioreceptor. Choosing the biorecognition element is one of the most important steps in the design of a biosensor. The key features of an ideal bioreceptor are high selectivity and specificity for the molecule of interest among the matrix of other biological components. Due to their ability to bind to a wide variety of substances, antibodies (Abs) are the most chosen over other bioreceptors as aptamers, DNA, cells and enzymes. Moreover, the analytical performance of a biosensor are strongly influenced by the way the Abs are immobilized on the surface, making the choice of the functionalization procedure a key factor in the development of a biosensor [43]. Over the years, a wide range of immobilization methods have been investigated and the choice of the most suitable depends on the nature of the bioreceptor, the transduction principle and the target molecule.

Abs (Figure 1.3) are characterized by two binding sites (antigen binding sites) that are responsible for selective recognition of the analyte (antigen). For an efficient biosensing, Abs (Figure 1.3) should be correctly immobilized on the biosensor surface in order to retain their biological function, which means that their binding sites should remain unobstructed and available to bind the target molecule. This makes functionalization of the transducer surface a critical step in biosensor development. Over the years, many functionalization methods have been proposed. The simplest method is to immobilize the antibody on the sensor surface by adsorption. Depending on the type of interaction that occurs between the antibody and the surface, adsorption can be defined as physisorption (physical) if weak

intermolecular bonds (van der Waals bonds) are involved or chemisorption (chemical) if strong intramolecular bonds are involved. Other immobilization methods exploit the specific interaction between two molecules (e.g. avidin/streptavidin and biotin), covalent bonds (e.g. sulfur-gold bonds), or entrapment in polymer matrices. Although these approaches provide effective immobilization of the antibody, they are time-consuming and laborious procedures applicable only in the laboratory setting as they require chemical treatments and several purification steps. In addition, the toxicity of some chemical reagents used could change the biological properties of Abs, including the ability to recognize the specific antigen. These problems motivated the introduction of a new surface functionalization named Photochemical Immobilization Technique (PIT) [44] that allows proper immobilization of the antibody while retaining its biological and analyte binding properties in order to achieve better sensitivity and lower detection limits. In the next paragraphs the most conventional functionalization techniques are listed, before delving into the characteristics of PIT.

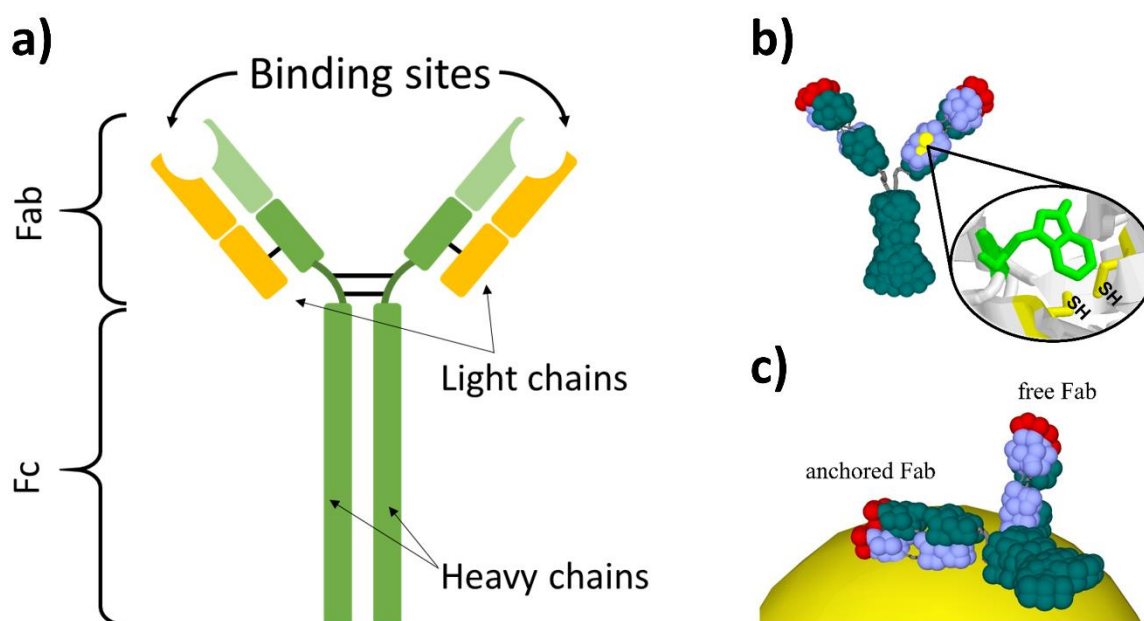


**Figure 1.3.** a) Schematic representation of the structure of an IgG antibody consisting of four peptide units, two heavy chains and two light chains. b) The UV irradiation protocol leads to the selective production of thiol groups, two of them are highlighted in the figure. c) Schematic representation of an antibody linked to a curve gold surface. Thanks to the position of the thiols that reacts with the gold surface, the antibody is immobilized with one binding site exposed to the surrounding medium.

### 1.2.1 Antibodies as bioreceptors

In the following paragraph, the main features of the antibodies will be briefly discussed since they were used as bioreceptor for all the sensors presented in thesis.

Monoclonal and polyclonal antibodies are among the most commonly used sensing elements as they can be prepared for a large number of analytes. Abs, also known as immunoglobulins (Ig), are glycosylated proteins that play a key role in the immune system since they are capable of tagging and neutralizing foreign substances that invade the body such as toxins or viruses. The immune system

recognizes extraneous substances as alien when they enter the body and starts to produce Abs in order to remove the infection. Different Abs are characterized by distinct antigen-binding sites produced and secreted by a peculiar B lymphocyte (white blood cells). Immunoglobulins make up approximately 20% of the total protein in plasma by mass, thus constituting the most abundant component of the blood. In particular, IgG, widely used in this thesis, represents the most abundant antibody isotype in blood which, approximately, accounts for the 75% of human adult serum immunoglobulins. It is the main effector molecule of the B cell activity against invading pathogens. In view of their properties, in particular the high specificity and avidity, immunoglobulins are commonly used as powerful bio-recognition element in biosensors development.

Abs consist of four polypeptide chains: two identical light chains of about 25 kDa and two identical heavy chains of about 50 kDa for a total of 150 kDa (Figure 1.3). Each polypeptide chain presents a specific region that is different for each antibody and a common region which does not vary significantly among Abs. The four chains are connected by a combination of disulphide bonds and non-covalent interactions (i.e. salt bridges, hydrophobic interactions and hydrogen bonds). The antigen binding sites of the antibody are at the end of the light chains.

Each part of an antibody has a different function. The top part, containing the two antigen binding sites, endows the antibody with specificity towards a particular segment of the target. This region, called Fab (antigen binding fragment), corresponds to the upper part of the structure and consists of one constant and one variable domain for each heavy and light chain of the antibody. The lower part of the structure plays a role in modulating immune cell activity and it is also the site of binding for secondary Abs.

In the biomedical and bio-sensing fields, as well as in diagnostic testing, and therapy, antibodies can be produced in several ways. The easiest way to achieve an efficient production is to immunize mammalian species such as mouse, rabbit, and goat. Immunization strategies are highly dependent on the properties of the antigen, such as its nature, solubility, purity, and availability. Immunizing mammals requires injecting a foreign antigen into the host so that, upon receiving such an injection, the immune system will produce an abundance of Abs. Blood samples are generally collected during the experiment so that the antibody response can be monitored. When the antibodies produced meet predetermined quality criteria they are purified by chromatography.

The Abs produced by several B cells clones against an injected antigen are called polyclonal antibodies (pAbs). pAbs possess the ability to bind different regions of the antigen. On one hand, this property provides a fast and efficient neutralization of the target. On the other hand, it may happen that the antibody recognizes non-specifically biomolecules that show similar parts to those of the target. Clearly, the risk of an a-specific detection is negligible with small molecules but increases in the detection of large-sized antigens (like bacteria). For this reason, monoclonal antibodies (mAbs)

are often preferred over pAbs for biosensing experiments. mAbs they are produced by identical B cell which are clones from a single parent cell implying that they are able to recognize only a specific region of an antigen. Unlike pAbs, which are produced in alive animals, mAbs are produced *ex vivo* using tissue-culture techniques. Since the procedure to produce mAbs are more time-consuming and complicated, they are more expensive than pAbs. A polyclonal antiserum can be obtained within a short time (4-8 weeks) with a modest financial investment whereas the production of mAbs takes about 3-6 months and requires more advanced techniques. Thus, the use of pAbs or mAbs depends on the time and money available for the production [45].

### **1.2.2 Conventional immobilization techniques**

In this Paragraph the most popular conventional immobilization techniques are listed before introducing the innovative Photochemical Immobilization Technique (PIT) used throughout the thesis work and presented in the next paragraph.

Physical adsorption of Abs onto a solid surface after a prolonged incubation is the easiest immobilization method [46,47]. This method results into weak and non-covalent interactions (electrostatic or ionic bonds, hydrophobic interactions and van der Waals forces) between Abs and the surface [48,49]. While the adsorption does not require any chemical modifications, resulting in an easy immobilization technique, weak bonds can be quickly dissolved by changes in environmental parameters (i.e. pH or temperature), making the surface coverage not stable over time. Furthermore, in the absence of privileged binding points, the Abs are orientated arbitrarily on the substrate often compromising their functionality.

Affinity interaction is a non-covalent method based on the specific interaction between two molecules, one linked to the sensor surface and the other to the molecule that should be immobilized. An example is the specific interaction between streptavidin and biotin [50,51]. The streptavidin, which has high affinity to biotin, can be covalently linked to surfaces functionalized with amino groups by cross-linking its amino or carboxyl functions. Then, biotinylated antibodies can bind the streptavidin-functionalized substrates with high affinity. This method has several advantages such as the great availability of pre-functionalized Abs with biotin. In fact, this strategy is particularly popular for functionalizing magnetic nanoparticles since some types of commercial magnetic nanoparticles coated with streptavidin are available on the market. On one hand, the biotinylation of Abs does not prejudice their functional activity but on the other hand the process is expensive and time-consuming. Moreover, as in the case of the adsorption method, the interaction biotin-streptavidin can be easily denatured by changes in pH or temperature.

Another methods to immobilize Abs is to exploit two intermediate binding proteins: protein A and protein G [52–56]. Such proteins are able to bind to the Fc region of antibodies leaving the antigen-binding sites free for binding to antigen molecules. Even if the tertiary structure of both proteins is very similar, they have inherent differences such as the optimal pH binding conditions which is 8.2 for protein A and 5 for protein G. Although these biomolecules recognize the Fc region of most immunoglobulins IgG, this interaction is not stable enough for most applications.

Several chemical strategies have been developed to covalently bind Abs molecules on a substrate. The most popular covalent immobilization methods require the surface to be modified with functional groups to which the antibodies will be attached. In recent years, a lot of attention has been given to the functionalization of noble metal surfaces with organic molecules in order to form self-assembled monolayers (SAMs) that provide oriented antibodies immobilization, ensuring the antibody binding sites are accessible. In thiols based monolayers, sulphur compounds adsorb onto gold surfaces by means of the formation of the strong bond S-Au, resulting in highly oriented and densely packed monolayers [57,58]. In spite of the many advantages, SAMs offer, there are several issues that should be considered in order to correctly assess their applicability [57,59,60]. The structure of SAMs on gold surfaces is usually described as a perfect monolayer, with molecules packed tightly together. In everyday life however, this model often deviates from reality. The realization of a well-assembled monolayer is essential to benefit from the advantages offered by the technique. The quality of SAMs is a key point in many applications and it strongly relies on factors that are difficult to control. For example the purity of the solutions used and the presence of even a low amount of contaminants, as for instance thiolated precursor molecules that are the typical impurities in thiol compounds, can lead to a non-uniform and, hence, non-ideal monolayer [61]. In addition, the sensor surface plays an important role in the realization of SAMs. In particular, several studies have shown that the roughness of the sensor surface to be functionalized significantly impacts the quality of the SAM layer, in several cases impairing functionality [62].

### **1.2.3 Photochemical Immobilization Technique (PIT)**

To overcome the issues outlined in the previous Paragraph, the well-established Photochemical Immobilization Technique (PIT) was adopted for antibody functionalization in this thesis. PIT is a fast, effective and easy to use strategy to tether Abs directly on noble metal surfaces (such as gold) in a proper orientation, that is with their binding sites well exposed upright to the environment (Figure 1.3c) [63–65]. This technique exploits UV irradiation of Abs that induce selective photoreduction of the disulfide bridge in specific cysteine-cysteine/tryptophan (Cys-Cys/Trp) triads [66]. Every immunoglobulin G has twelve triads but it has recently been demonstrated that only two of them are involved in this process [65]. The breakage of such Cys-Cys bonds in both Ab Fab fragments is by

solvated electrons generated by the UV excitation (Figure 1.4) of the trp. The whole process produces four free thiol groups (Figure 1.3b) two of which are able to interact with gold surfaces giving rise to a covalent Ab tether. Moreover, PIT was also successfully applied to functionalize AuNPs in colloidal solutions to provide either colorimetric transducers [14,27] or a ballasting tool for mechanical platforms [20].

Practically, the Abs solutions are irradiated for 30-60 s, according to the UV lamp used (for protocol details see Paragraph 2.3.2, 3.3.3 and 4.3.4). This time is the result of an optimized protocol that, as confirmed by the Ellman's assay [67], produces a high concentration of UV-activated antibodies while guaranteeing no denaturation of the antibodies as evidenced by their selectivity and efficiency in antigen binding in the developed biosensors. Compared to the conventional methods, PIT is a quick and user-friendly immobilization method which does not require a previous modification of the surface.

In previous works, PIT has been used in a number of experiments to develop sensitive and selective biosensor (i.e. QCM-based [68–71] and colorimetric biosensors [14,27,72]) assuring both close-packing and control over the orientation of the immobilized Abs [65,73].

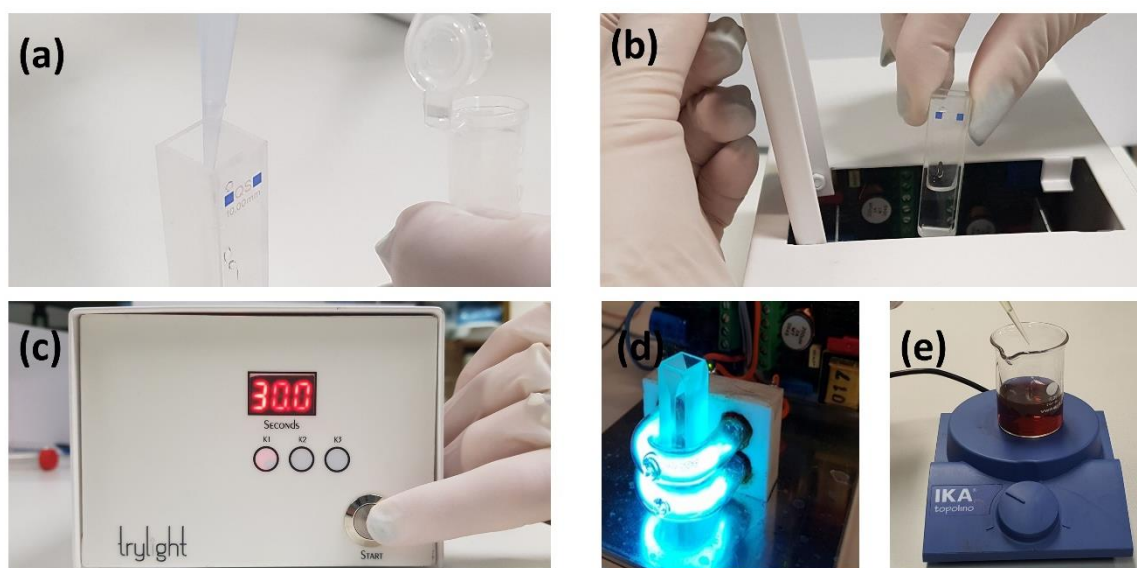


**Figure 1.4.** Example of use of the Photochemical Immobilization Technique (PIT). a) 1 mL of Ab solution at  $25 \mu\text{g}\cdot\text{mL}^{-1}$  was pipetted in a standard quartz cuvette. b) The cuvette was placed into the lamp and c) irradiated for 30 s. d) Detail of the UV lamp when turned on. e) Functionalization of a colloidal solution of nanoparticles. The Abs solution, previously the irradiated, was spiked into the solution with nanoparticles while magnetically stirred.

## 1.3 Nanoparticles

### 1.3.1 Gold nanoparticles

Nanoparticles technologies enabled a revolution in the field of sensing tools, providing opportunities and possibilities. A major research line in the last decade has been the use of functionalized AuNPs for sensing selective biomolecules. Because of their unique tunable optical properties, AuNPs are being extensively investigated in various fields, including sensing, detecting, and imaging. To date, advances in AuNPs synthesis have led to better control over their size and shape, establishing them as an increasingly useful tool. AuNPs are being largely used in biosensing thanks to their inertness and plasmonic properties, which make them highly exploitable in manifold ways. Moreover, they are widely used due to their biocompatibility and their large specific surface area on which bioreceptors such as Abs can be properly immobilized Figure 1.5.

AuNPs exhibit unique plasmonic properties due to their capability to confine the electromagnetic (EM) waves within the near-field region close to the surface. This provides them with unique features; such as extremely large electric field enhancements [74], nano-antenna [75], huge light scattering and absorption [76], and striking photothermal conversion capabilities [77]. In the last years, considerable efforts have been performed in order to exploit plasmonic properties of the nanostructures in the biosensing field. Several different plasmonic biosensors were developed to improve the sensitivity and to reduce the response-time [78–80]. One of the most attractive are AuNPs-based colorimetric biosensors since they are cheap, simple to manufacture and can be extremely sensitive. The absorbance wavelengths of noble metal nanospheres (gold and silver) are in the visible region thereby giving rise to the vivid colors of their colloidal solutions. The color depends both on their diameter and on the surrounding medium [21]. Gold is generally preferred to silver because of its biocompatibility [81], inertness [82] and surface chemistry [16].

Another popular use of AuNPs is as ballasting tool for mass-based biosensors, in the process known as biological signal amplification [20]. The amplification of the response signal via AuNPs exploits the typical sandwich-assay scheme, in which AuNPs, functionalized with bioreceptors (e.g. Abs), bind to the couple target-bioreceptor (e.g. Antigen-Ab) steering on the sensor surface. Thus, the mass loading on the sensor surface increases, enhancing its sensitivity of detection.

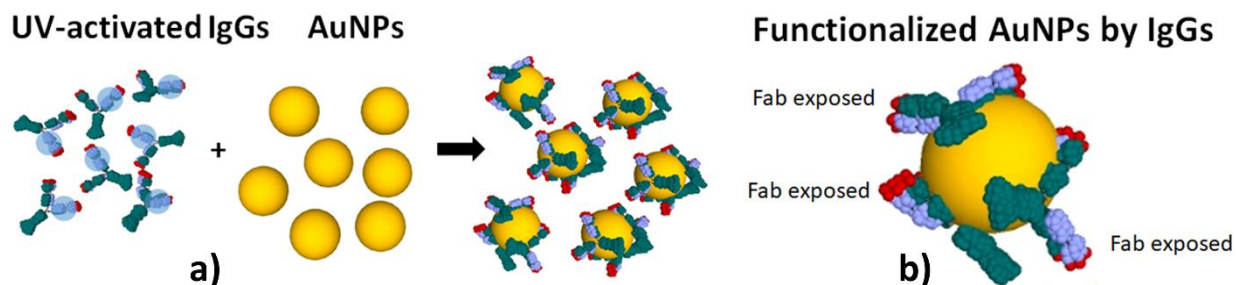


**Figure 1.5.** a) Schematic representation of the functionalization process involving AuNPs and UV-activated antibodies. b) Detail of a single functionalized gold nanoparticle with three Abs. Adapted from [25].

### 1.3.2 Gold decorated magnetic nanoparticles

Magnetic nanostructures are currently a topic of great interest for the scientific community as evidenced by the growing number of scientific publications on the subject (Figure 1.6) [83]. The ability to manipulate and control the properties of nanoscale objects through an external magnetic field has already been exploited in several fields from diagnostic imaging to biosensing [83,84].

Among these materials, magnetic nanoparticles (MNPs) have gained popularity due to their exceptional magnetic properties and the ability to adjust them by changing shape and size [6,7]. MNPs are generally composed of two entities, a central core made in most cases of magnetite or maghemite and a chemical component on the outer surface with bio-recognition properties. The most important disadvantages of such a setup, is that the procedures employed to link the bioreceptor to the metallic core are complicated, expensive and time-consuming. Furthermore, the biological layer is often not sufficient to effectively protect the magnetic core from oxidation.

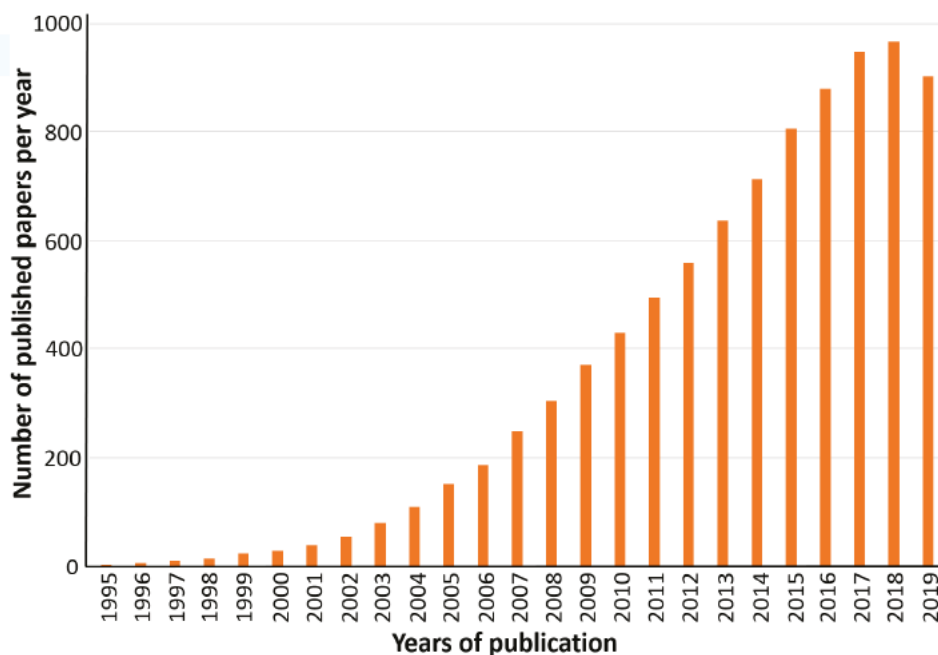


**Figure 1.6.** The number of published papers mentioning “magnetic nanoparticles” derived from statistics (Web of Science), the statistics for 2019 is not complete. The image is reproduced from [83].

To overcome such issues, protocols have recently been studied to cover the magnetic core with a coating of noble metal. The outer layer, usually gold or silver, endows the nanoparticle with superior stability and durability making it possible for biosensing applications. The presence of gold makes the structure biocompatible and allows the use of well-known powerful functionalization techniques to link the bioreceptor to the gold decorated magnetic structure.

Gold coated magnetic nanoparticles have been recognized and applied in analytical chemistry mostly for bio-separation and the development of electrochemical and optical sensors [85,86]. Applications of these particles in biomedicine, including magnetic resonance imaging contrast agents [87] and targeted drug delivery [88] have also been explored. The reason that these particles can be used for so many applications is because they are highly versatile; the optical and magnetic properties of the particles can be tuned and tailored to applications by changing their size, gold shell thickness, shape, charge, and surface modification. One of the major issues with gold decorated magnetic nanoparticles is that being a relatively new topic there are not yet many products on the market and the protocols available in the literature require expensive laboratory equipment or are complex and time-consuming.

Gold decorated magnetic nanoparticles can be assembled in several ways. They can be classified as core@shell, core@satellite, nanodumbbells and hybrid structures [17]. In this paragraph the core@shell and the core@satellite, that have been exploited for sensing purposes in this thesis, are briefly discussed.

Core@shell nanoparticles are characterized by the presence of a uniform gold coating around the magnetic core (Figure 1.7a). In this configuration the magnetic core does not come into contact with the external environment resulting in a high stability of the structure. Moreover, the fact that the surface is entirely covered with gold allows to maximize the presence of Abs per particle. One of the disadvantages of this configuration is that the diamagnetic nature of gold causes the outer shell to shield the magnetic field produced by the core with the result that the magnetic properties of the core@shell structure are weakened.

Core@satellite magnetic particles (CSMPs) have a single magnetic core with the binding by covalent bonds of numerous AuNPs similar to satellites (Figure 1.7b). The CSMPs comprise a residually exposed magnetic core surface suitable for magnetic resonance imaging and further functionalization. In addition, the CSMPs structure consists of many peripheral AuNPs with a large surface area of the satellite nanoparticle that is advantageous for imaging as well as photothermal capabilities [89]. This configuration is particularly suitable for applications where the magnetic properties of nanoparticles are to be exploited to the fullest. In fact, the AuNPs around the magnetic surface do not shield the field as much as in the case of core@shell structures.

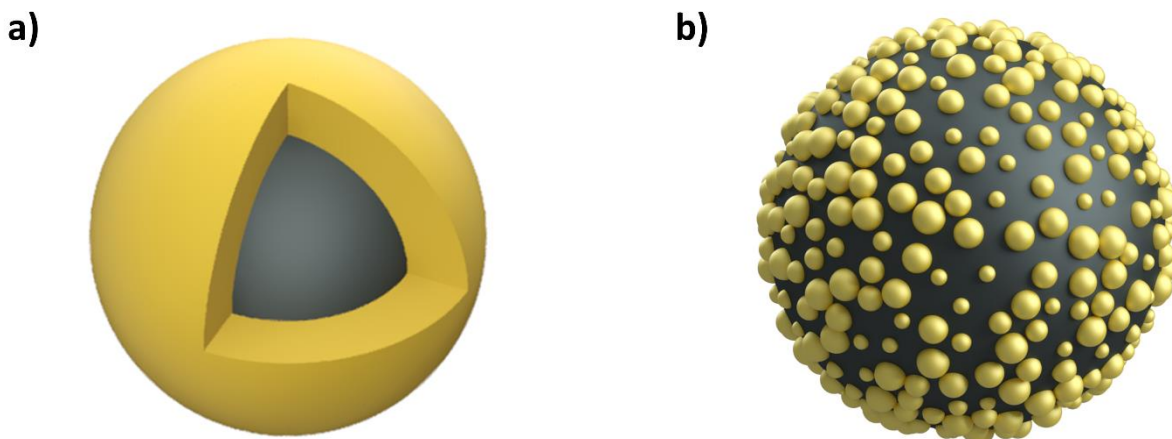


**Figure 1.7.** Schematic representation a) of a core@shell structure and b) a core@satellite structure.

## Chapter 2. Magnetoelastic biosensor

In this Chapter a magnetoelastic (ME) biosensor for wireless detection of analytes in liquid is described. The ME biosensor was tested against Human IgG in the range 0–20  $\mu\text{g}\cdot\text{mL}^{-1}$ . The sensing elements, anti-Human IgG produced in goat, were immobilized on the surface of the sensor by using a recently introduced Photochemical Immobilization Technique (PIT), whereas a new amplification protocol exploiting gold coated magnetic nanoparticles ( $\text{Fe}_3\text{O}_4@\text{Au}$  MNPs) is demonstrated to significantly enhance the sensitivity. In particular, the gold nanoflowers grown on the magnetic core allowed us to tether anti-Human IgG on the nanoparticles so to exploit the sandwich detection scheme. The experimental results show that the 6 mm  $\times$  1 mm  $\times$  30  $\mu\text{m}$  ME biosensor with an amplification protocol that uses magnetic nanoparticles has a limit of detection (LOD) lower than 1 nM, works well in water and has a rapid response time of few minutes. Therefore, the ME biosensor is promising for real-time wireless detection of pathogens in liquids and for real life diagnostic purpose.

**Paragraph 2.1** contains an overview of the content outlined in the Chapter, highlighting the novelty points and scope of the work. **Paragraph 2.2** summarize the most important features of the theory of the magnetoelasticity. The materials and methods exploited to build the biosensor and to analyze the data are reported in **Paragraph 2.3**. In **Paragraph 2.4** are presented the results related to the advantages of using  $\text{Fe}_3\text{O}_4@\text{Au}$  MNPs as well as the biosensing performance of the magnetoelastic biosensor. In **Paragraph 2.5** the interaction among  $\text{Fe}_3\text{O}_4@\text{Au}$  MNPs is modeled and the dose-response curve is analyzed. The conclusions of the work are drawn in the **Pragraph 2.6**.

Some of the content included in this chapter has been published on Nanomaterials from MDPI.

## 2.1 Overview

In recent years biosensors have proven to be an interesting platform for developing sensitive and portable devices devoted to detecting biological or chemical entities for a variety of applications, such as monitoring of environmental pollutants, food and water safety and biomedicine [18].

Recently, among the magnetic biosensors [90–92], magnetoelastic materials (ME) have emerged as interesting acoustic-wave transducers for development of high-sensitive biosensors [19]. ME sensors can be placed in a vibration condition due to magnetostriction effect, at the characteristic resonance frequency  $f_0$ , employing time-varying magnetic fields. The attaching of a small mass to the surface of the material involves a shift of the resonance frequency, which can therefore be used as sensing parameter. In fact, the mass addition dampens the resonance behaviour of the resonant sensor. The principal competitive advantage of ME biosensors is that they are wireless, namely there is no physical connection between the detection electronics and the sensor. Wireless sensing turns out to be a very interesting feature for applications as point of care testing, especially by considering that most of the other devices require complex wiring for power and measurement. Furthermore, ME transducers are composed by a low-cost raw material, and their compact size make them suitable for multiplexing schemes. However, sensitivity remains the main drawback of these transducers. Recent attempts to enhance sensitivity rely on several strategies such as the reduction of the size of ME platforms [93], and the amplification of the signal response by using gold nanoparticles (AuNPs) [94]. It should be noted that the attempt of reducing the dimension of sensor platforms is limited by manufacturing difficulties and loss of the intensity of the signal that occur when the microscale is reached [95,96].

AuNPs are widely used in biosensing due to their high chemical stability, biocompatibility and large specific surface area on which bioreceptors such as Abs can be properly immobilized. In the case of a ME sensor, the amplification of the response signal via AuNPs exploits the typical sandwich-assay scheme, in which AuNPs, functionalized with bioreceptors (e.g., Abs), bind to the target-bioreceptor pair (e.g., antigen-Ab) on the sensor surface. Thus, the mass loading on the ME sensor surface increases, enhancing its sensitivity of detection.

Besides AuNPs, magnetic nanoparticles have also found application as signal labels in biosensing systems, such as molecular detection and related strategies that rely on ligand-receptor binding. In particular, iron oxide magnetic nanoparticles (MNPs), such as magnetite ( $\text{Fe}_3\text{O}_4$ ) and maghemite ( $\gamma\text{-Fe}_2\text{O}_3$ ), are particularly appealing due to their magnetic properties, tunable size, and greater ease of synthesis than other magnetic materials [83,97,98]. Indeed, recent studies have shown how to use magnetic nanoparticles to improve the efficiency of the functionalization process [99], to realize multiplexing immunoassays [100] and for magnetic detection [92,101,102].

In this Chapter, we describe how core@shell magnetic nanoparticles ( $\text{Fe}_3\text{O}_4@Au$ , i.e., gold nanoflower grown on a magnetic core) can be used to amplify the signal from a ME biosensor for wireless detection of contaminants in liquid. The use of the magnetic properties of nanoparticles is a current and relevant topic for scientific community, although the tendency to aggregation is an obstacle to their applications. In our case, the  $\text{Fe}_3\text{O}_4$  MNPs gold coating and functionalization protocols employed for signal amplification have also the effect to prevent nanoparticles aggregation, so that other complex and time-consuming techniques can be avoided [103,104]. The sensor platform is a low-cost and commercially available ME material (Metglas 2826), shaped in a ribbon of small size ( $6\text{ mm} \times 1\text{ mm} \times 30\text{ }\mu\text{m}$ ). We propose the synergy of two strategies to increase the performance of this sensor: (i) a new amplification procedure that exploits gold coated nanoparticles with magnetic core (ii) the use of reliable, quick and easy-to-use antibody functionalization procedure. We observed that the signal amplification obtained with  $\text{Fe}_3\text{O}_4@Au$  was significantly higher than that obtained using AuNPs. The fact that in our case both the magnetic sensitive platform and magnetic nanoparticles contribute to the measurements process is an element of novelty in comparison with standard configurations, widely discussed in literature [105,106]. It should be noted that the amplification of the shift of the resonance frequency of the ME sensor is due to the mass of magnetic nanoparticles and does not depend directly on their magnetic properties. Indeed, the advantage of the magnetic core of the nanoparticles relies in its coupling with the local magnetic field, which in turn leads to an increase of the local density at proximity of the ribbon surface. Such an effect can be well understood by working out the magnetic field produced by the magnetized ribbon and comparing its action on a magnetic nanoparticle with the thermal energy (Brownian motion).

Regarding the functionalization procedure, the Photochemical Immobilization Technique (PIT) recently introduced by Della Ventura et al. [65] not only was used for the first time to functionalize a ME material (coated with gold), but also the gold nanoflowers grown on the magnetic nanoparticles. This technique, based on a controlled UV-activation of Abs, has proven to be an effective [28,68,73,107–109] and competitive methodology since it is rapid and user-friendly and leads to strong (covalent) and conveniently oriented bonds of Abs on the sensor surfaces, without affecting the intrinsic selectivity of the antibodies.

The experimental results show that the proposed ME biosensor has a reliable stability in liquid, a quick response to antigen exposure and exhibits a limit of detection (LOD) lower than 1 nM.

## 2.2 The theory of magnetoelasticity

### 2.2.1 Metallic glasses

The constituent materials of the magnetoelastic sensor belong to the class of amorphous solids. A solid is amorphous when it does not show long-range order, thereby it is impossible to find a clear structure above the atomic scale. The elementary building block in the amorphous solids are arranged irregularly, they do not possess any kind of definite geometry and have a short-range order. The amorphous state (also called the glassy state) is characterized by a brusque transition that the material undergoes when it is rapidly cooled down. Typically, the materials that exhibit this behavior are composed of elements belonging to the 4<sup>th</sup>, 5<sup>th</sup> and 6<sup>th</sup> column of the periodic table of elements, e.g. SiO<sub>2</sub>, of which the common glass is mostly composed. In Figure 2.1a, a schematic representation of the crystallographic structures of crystalline and amorphous materials is shown. It is possible to assess the nature of the structure of a material by X-ray diffraction (XRD) [110]. The resulting intensity of the diffraction peaks  $I(K)$  is given by the following equation:

$$I(K) = \sum_m \sum_n f_m f_n \frac{\sin(Kr_{mn})}{Kr_{mn}}, \quad 2.1$$

where  $f$  is the atomic form factor,  $K = |\Delta\mathbf{k}| = \mathbf{k}' - \mathbf{k}$  with  $\mathbf{k}'$  and  $\mathbf{k}$  being the wavevector of the outgoing and ingoing beam respectively and lastly  $r_{mn} = |\mathbf{r}_m - \mathbf{r}_n|$  the modulus of the difference between the position vectors of two atoms in the position  $m$  and  $n$  respectively. A crystalline structure will be characterized by a spectrum with sharp peaks corresponding to the directions in which the interference among the ingoing and the outgoing beam is constructive. On the other hand, the spectrum of an amorphous material will be characterized by broader peaks because of the random positioning of atoms or molecules in the structure. To better understand the amorphous structure, it is possible to calculate the Fourier transform of the XRD distribution, obtaining the radial distribution  $4\pi r^2 \rho(r)$ , where  $\rho(r)$  is the concentration of atoms at distance  $r$ . The profiles of the radial distribution of atoms for a solid in the amorphous state to the one for a liquid it turns out to be in agreement and for this reason the glassy phase is often described as an extrapolation of the liquid phase [111].

Metallic glasses can be produced through different techniques, but all of them use the rapid cooling of the liquid phase, so that the atoms do not have enough time to rearrange themselves to form a crystal lattice. The most spread technique is the one called *planar-flow casting* that exploits cooling rates around  $10^4$ - $10^5$  K·s<sup>-1</sup>. One of the effects of rapid cooling is that the short time taken for solidification, forces the material to remain in the glassy state, although the crystalline state is more favorable from an energetic point of view. This happens because this time is not sufficient to allow

the reorganization of the strong covalent bonds (i.e. in the case of common glass SiO<sub>2</sub>, Si-Si or Si-O bonds) into an ordered long-range structure (Figure 2.1b) [112].

Providing a detailed description of the properties of solid amorphous metals and their fabrication processes is beyond the scope of this work, which focused on applications of these materials in the field of biosensing. A complete discussion of amorphous metals can be found in [113].

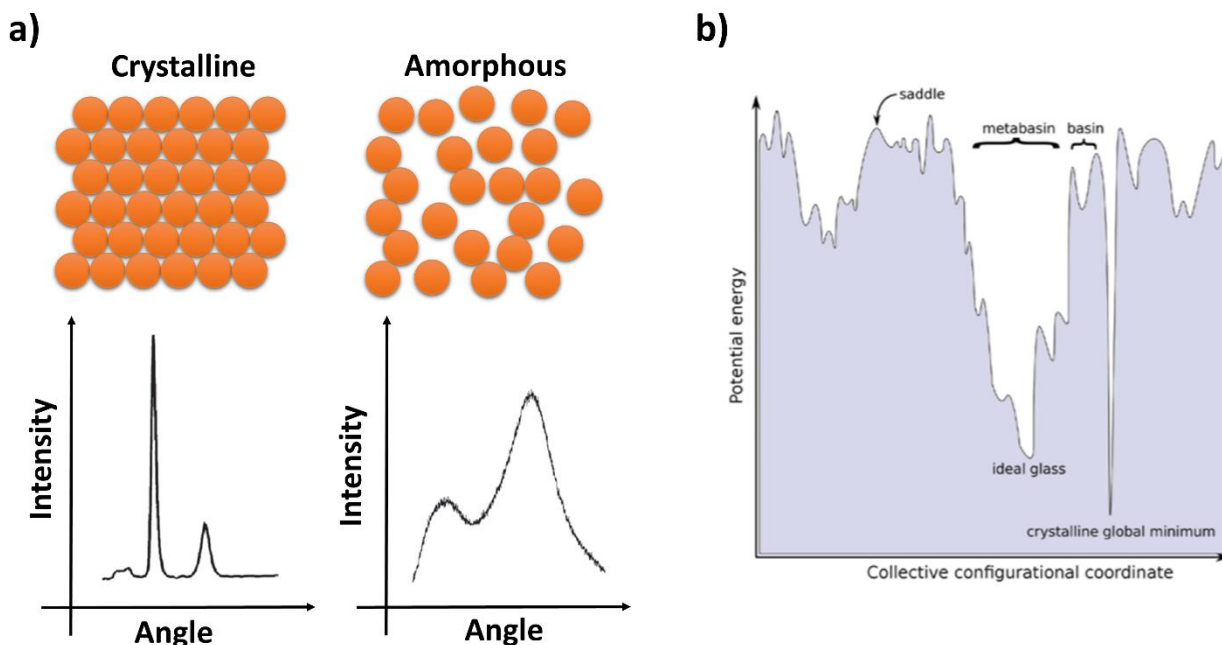


**Figure 2.1.** a) Schematic representation of the structure of a crystalline and amorphous solid and the associated X-ray diffraction (XRD) spectra. b). Schematic representation of potential energy of amorphous and crystalline state for an amorphous solid (glassy phase). Rapid cooling forces the material to remain in the glassy state, although the crystalline state is more favorable from an energetic point of view. The figures are adapted from [110] and [112].

### 2.2.2 Physical origin of magnetoelasticity

The elastic and magnetic properties of matter are linked so that when a material is subjected to a magnetic field, it undergoes a change in its shape, while if it is subjected to external stress, a change in its magnetization occurs. These two effects are called respectively direct magnetoelastic (magnetostrictive) effect and inverse magnetoelastic (magnetomechanical) effect. Although this effect is negligible in most materials, this is not true for some types of metallic glasses. In this work we will focus on the magnetostrictive effect, whose working mechanism is depicted in Figure 2.2, because it was the one exploited for the magnetoelastic sensor discussed in this Chapter. The physical origin of the magnetostrictive effect lies in the spin-orbit coupling of the electrons. The effective strain  $\Delta L \cdot L^{-1}$ , enlarged for visual reasons in Figure 2.2, is due to the reorientation of the electrons' spins along the direction of the external magnetic field which also involves a reconfiguration of the orbits with a consequent structural deformation. Typical values of magnetostriction are around units or a few tens of parts per million (p.p.m), i.e. for Metglas 2826 is  $11 \cdot 10^{-6}$ , which leads to a strain of  $66 \mu\text{m}$  for a 6 mm long ribbon [114].

There are several approaches to study magnetostriction, but the most spread out are the group theory and the thermodynamic description, both phenomenological. In this work it has been chosen to illustrate the thermodynamic approach which is most suitable for describing applications in the field of biosensing because with this method it is easier to solve the wave equation and obtain the resonant frequencies of the ME ribbon.

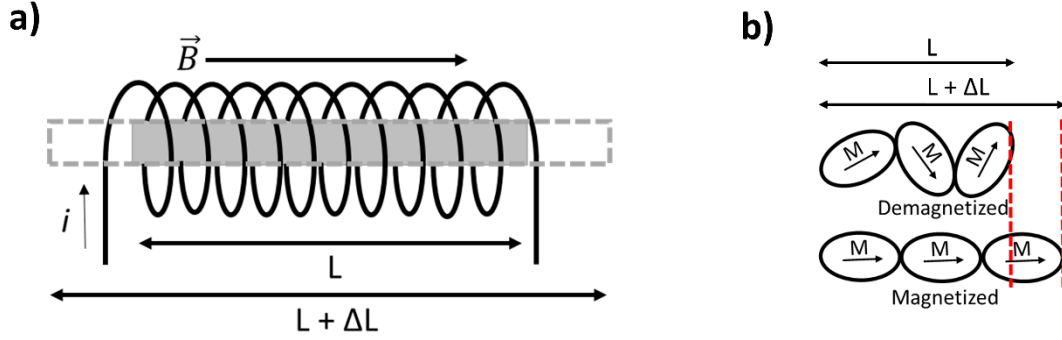


**Figure 2.2.** Schematic representation of direct magnetoelastic (magnetostrictive) effect. In panel a) a magnetoelastic ribbon is magnetized by means of an external magnetic field generated by a coil which increases the length of the ribbon by a quantity  $\Delta L$ . In panel b) a schematic representation of how the physical principle of the magnetostrictive effect works. The external magnetic field causes a reorientation of the electrons' spins which also involves a reconfiguration of the orbits and a consequential structural deformation.

### 2.2.3 Thermodynamic approach

In the thermodynamic framework it is possible to derive constitutive equations of magnetoelasticity from the internal energy choosing as extensive parameter: entropy, strain and flux density, i.e.  $U(S, \gamma, B)$ . From the first law of thermodynamics:

$$dU = \delta L + \delta Q, \quad 2.2$$

where  $\delta L$  is the infinitesimal work done by external forces and  $\delta Q$  is the heat absorbed by the body. In this case, the external forces are due to the shear stress  $\tau_{ij}$  [115] induced by the magnetic field  $H_i$ . When an external force is applied to the material, for example in the  $z$  direction, the following equation holds true:

$$F_z = \rho \frac{\partial^2 u_z}{\partial t^2} = \left( \frac{\partial \tau_{zx}}{\partial x} + \frac{\partial \tau_{zy}}{\partial y} + \frac{\partial \tau_{zz}}{\partial z} \right). \quad 2.3$$

By combining Equation 2.2 with the second law of thermodynamics for reversible processes, it is obtained:

$$dU = T\delta S + \tau_{ij}d\gamma_{ij} + H_i dB_i, \quad 2.4$$

where  $S$  is the system entropy,  $\gamma_{ij}$  the symmetric terms of the deformation tensor [115] and  $B_i$  the magnetic induction. Using the definition of internal energy, it is possible to derive the following relation:

$$\left(\frac{\partial U}{\partial B_i}\right)_{\gamma_{kl}} = H_i \left(\frac{\partial U}{\partial \gamma_{ij}}\right)_{B_k} = \tau_{ij} \quad 2.5$$

The eight magneto-elastic coefficients, which are third-order tensors two by two identical, can be obtained as in [116]:

$$\left(\frac{\partial H_k}{\partial \gamma_{ij}}\right)_{B_l} = \left(\frac{\partial \tau_{ij}}{\partial B_k}\right)_{\gamma_{mn}} = -h_{ijk} \quad 2.6$$

$$-\left(\frac{\partial H_k}{\partial \tau_{ij}}\right)_{B_l} = \left(\frac{\partial \gamma_{ij}}{\partial B_k}\right)_{\tau_{mn}} = g_{ijk} \quad 2.7$$

$$\left(\frac{\partial B_k}{\partial \tau_{ij}}\right)_{H_l} = \left(\frac{\partial \gamma_{ij}}{\partial H_k}\right)_{\tau_{mn}} = d_{ijk} \quad 2.8$$

$$\left(\frac{\partial B_k}{\partial \gamma_{ij}}\right)_{H_l} = -\left(\frac{\partial \tau_{ij}}{\partial H_k}\right)_{\gamma_{mn}} = e_{ijk} \quad 2.9$$

Each of the four quantities  $B_i, H_i, \gamma_{ij}, \tau_{ij}$  can be written as a function of a magnetic term and a mechanical term, giving rise to four pairs that give the constitutive equations of magneto-elasticity as reported in [117].

$$\begin{cases} \gamma_{ij} = s_{ijmn}^{H_k} \tau_{mn} + d_{ij} H_l \\ B_i = d_{imn} \tau_{mn} + \mu_{il}^{\tau_{kh}} H_l \end{cases} \quad 2.10$$

$$\begin{cases} \tau_{ij} = c_{ijmn}^{B_k} \gamma_{mn} - h_{ijl} B_l \\ H_i = -h_{imn} \gamma_{mn} + v_{il}^{\gamma_{kh}} B_l \end{cases} \quad 2.11$$

$$\begin{cases} \gamma_{ij} = s_{ijmn}^{B_k} \tau_{mn} + g_{ijl} B_l \\ H_i = -g_{ijmn} \tau_{mn} + v_{il}^{\tau_{kh}} B_l \end{cases} \quad 2.12$$

$$\begin{cases} \tau_{ij} = c_{ijmn}^{H_k} \gamma_{mn} - e_{ijl} H_l \\ B_i = e_{imn} \gamma_{mn} + \mu_{il}^{\gamma_{kh}} H_l \end{cases} \quad 2.13$$

Table 2.1 Fundamental magnetoelastic constants

|                                  |                          |                             |
|----------------------------------|--------------------------|-----------------------------|
| Constant flux density <b>B</b>   | $c_{ijmn}^{B_k}$         | Specific elastic stiffness  |
|                                  | $s_{ijmn}^{B_k}$         | Specific elastic compliance |
| Constant field strength <b>H</b> | $c_{ijmn}^{H_k}$         | Specific elastic stiffness  |
|                                  | $s_{ijmn}^{H_k}$         | Specific elastic compliance |
| Constant strain $\gamma$         | $\mu_{il}^{\gamma_{kh}}$ | Permeability                |
|                                  | $\nu_{il}^{\gamma_{kh}}$ | Reluctivity                 |
| Constant stress $\tau$           | $\mu_{il}^{\tau_{kh}}$   | Permeability                |
|                                  | $\nu_{il}^{\tau_{kh}}$   | Reluctivity                 |

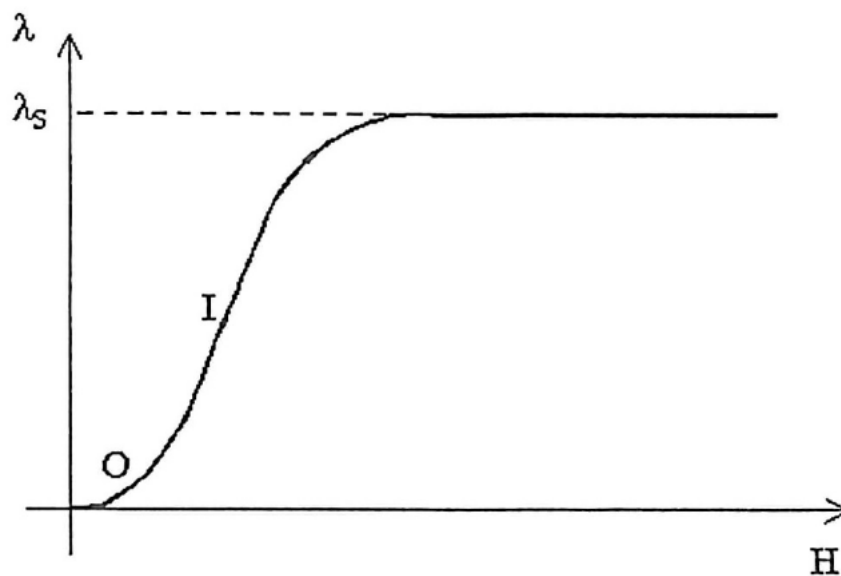


**Figure 2.3.** Schematic representation of a  $\lambda$  vs  $H$  curve of an amorphous ferromagnetic material. Values of  $H$  in correspondence to the (O) region and the saturation plateau lead to no magnetoelastic effect because small variations of the field do not cause relevant variations for  $\lambda$ . On the contrary, if they occur in proximity of the region (I), which has the maximum slope, the material undergoes the magnetoelastic effect.

Equations from 2.10 to 2.13 only holds for small perturbations (e.g. small deformations) around equilibrium values where the material behavior can be considered linear and almost reversible. These conditions are satisfied for amorphous ferromagnetic materials mainly due to their soft magnetic properties, in fact the linearity condition of the direct magnetoelastic effect occurs if the external polarizing field  $H$  is located next the inflection point (I) of the  $\lambda(H)$  curve shown in Figure 2.3 where

$\lambda$  is the magnetoelastic coefficient [118]. Thus, in proximity of the region (I) it is possible to replace the infinitesimal value  $dX$  with the finite value  $X$ , where  $X = (\mathbf{B}, \mathbf{H}, \gamma, \tau)$ :

Table 2.1 shows the roles of the constants obtained.

#### 2.2.4 Acoustic wave equation in air

In the thin beam approximation it is possible to derive the equation of motion for the displacements involved in Equation 2.3 by using the first equation of 2.10 [117]:

$$(s_{33}^{-1})_H \left[ \frac{\partial^2 u_z}{\partial z^2} - g_{33} \frac{\partial H_z}{\partial z} \right] = \rho \frac{\partial^2 u_z}{\partial t^2}. \quad 2.14$$

By combining Equations 2.14 and 2.9 it is obtained the following relationship:

$$(s_{33}^{-1})_H [1 - e_{33} g_{33}] \frac{\partial^2 u_z}{\partial z^2} = \rho \frac{\partial^2 u_z}{\partial t^2}, \quad 2.15$$

which is the wave equation of an acoustic oscillatory phenomenon with propagation velocity

$$v = \sqrt{\frac{(s_{33}^{-1})_H [1 - e_{33} g_{33}]}{\rho}} = \sqrt{\frac{E}{\rho}}. \quad 2.16$$

By imposing the free-standing boundary conditions  $\partial_z u_{z=0} = 0$  and  $\partial_z u_{z=L} = 0$ , (where  $L$  is the length of the rod) the following harmonic frequencies are obtained [115]:

$$f_n = \frac{1}{2L} \sqrt{\frac{E}{\rho}} n = f_0 n. \quad 2.17$$

The magnetoelastic biosensor discussed in this chapter exploits a ribbon with width/length ration of 1:6. For this ratio the beam approximation fails implying that the equations 2.15 and 2.17 must be modified. A better approximation can be obtained by introducing the Poisson's ratio ( $\sigma$ ) in the model [106,119,120]:

$$\frac{\partial^2 u_z}{\partial z^2} - \frac{\rho(1 - \sigma^2)}{E} \frac{\partial^2 u_z}{\partial t^2} = 0, \quad 2.18$$

$$f_n = \frac{1}{2L} \sqrt{\frac{E}{\rho(1 - \sigma^2)}} n = f'_0. \quad 2.19$$

### 2.2.5 Oscillations in liquids

As described in this Chapter, ME biosensors operating principle is based on the Joule magnetostriction of magnetic materials, which can vibrate longitudinally at a characteristic frequency, depending not only on physical parameters of the materials but also on the external environment. For a ribbon shaped sensor, that undergoes a plane-stress or biaxial state, the fundamental resonance frequency in air,  $f_{air}$ , is given by equation:

$$f_{air} = \frac{1}{2L} \sqrt{\frac{E}{\rho(1 - \sigma^2)}}, \quad 2.20$$

where  $L$  is the length of the ribbon,  $E$  its Young's modulus,  $\rho$  its density and  $\sigma$  the Poisson's ratio [120], while in low viscosity liquids the resonance frequency,  $f_{liq}$ , is given by equation:

$$f_{liq} = f_{air} - \frac{\sqrt{\frac{\eta_{liq}\rho_{liq}}{\pi}}}{2\rho d} \cdot \sqrt{f_{air}}, \quad 2.21$$

where  $\eta_{liq}$  and  $\rho_{liq}$  are the dynamic viscosity and density of the liquid (Figure 2.4). The relationship 2.21 is obtained by approximating the ribbon to a thin beam, a valid approximation when the thickness is negligible with respect to the other two dimensions involved. The length to width ratio is needed to be greater than five for a good magnetoelastic response of the material, the latter being further improved for ratios greater than fourteen [121]. In our case we chose a length to width ratio of six because, as the length and mass of the sensor increases, the mass sensitivity ( $S_m$ ) decreases [122].

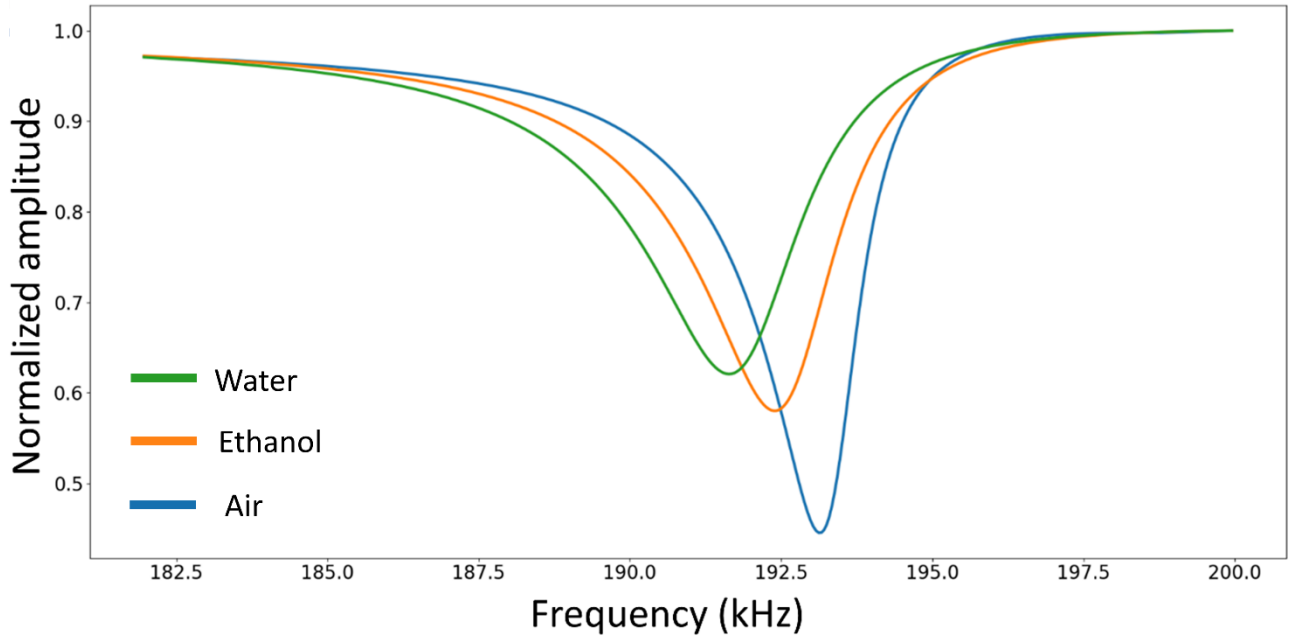


**Figure 2.4.** Resonance frequency of a magnetoelastic ribbon in different media.

### 2.2.6 Mass sensitivity

When the testing temperature, humidity and other environmental parameters are constant, the resonance frequency change of the magnetoelastic sensor depends only on the mass change on its surface (Figure 2.5). In the approximation of small mass loading ( $\Delta m \ll M_{ME}$ ) uniformly distributed on the ribbon surface, the shift in resonance frequency in low viscosity liquids is given by equation:

$$\Delta f_{liq} = -\frac{5f_{liq} - 3f_{air}}{4M_{ME}} \Delta m, \quad 2.22$$

where  $f_{liq}$  is the initial resonance frequency in liquid,  $\Delta f_{liq}$  its variation due to the detection of antigens of mass  $\Delta m$  and  $M_{ME}$  is the initial mass of the ribbon [122]; thus, the sensitivity of the sensor is:

$$S_m = -\frac{\Delta f_{liq}}{\Delta m} = \frac{5f_{liq} - 3f_{air}}{4M_{ME}}. \quad 2.23$$

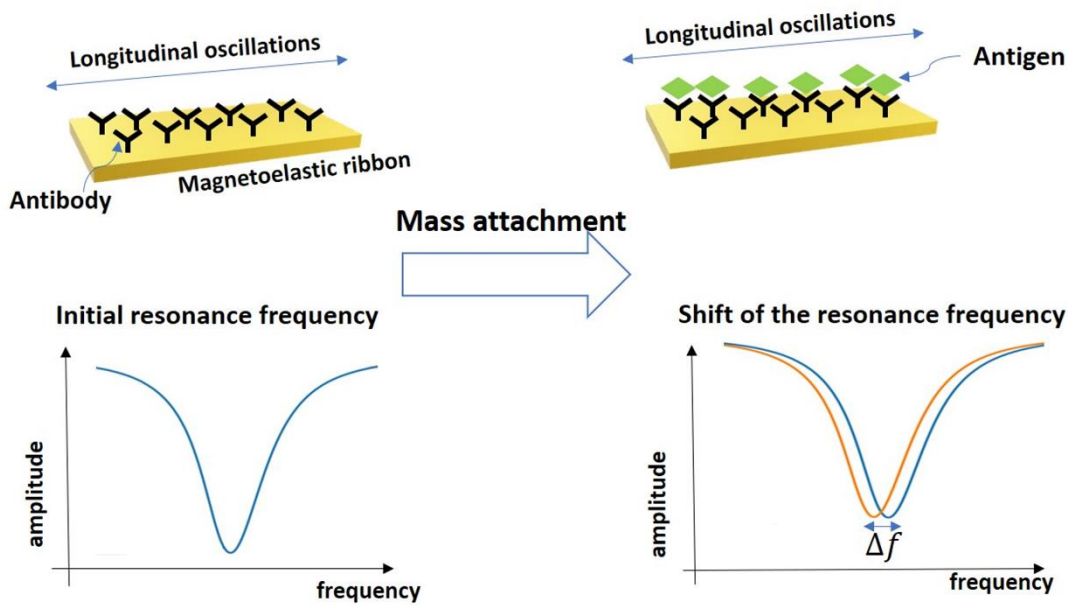


**Figure 2.5.** When environmental parameters are constant, the resonance frequency change of the magnetoelastic sensor depends only on the mass change on its surface and in this particular case by the recognition of the target. In the approximation of small mass loading ( $\Delta m \ll M_{ME}$ ) uniformly distributed on the ribbon surface, the shift in resonance frequency in low viscosity liquids can be calculated.

## 2.3 Materials and methods

### 2.3.1 ME sensors fabrication

ME sensors platforms, composed of Metglas alloy 2826 ( $\text{Fe}_{40}\text{Ni}_{40}\text{P}_{14}\text{B}_6$ ), were purchased from Honeywell Corporation (Morriston, NJ, USA) in the form of roll and cut in ribbon form with the dimensions  $6 \text{ mm} \times 1 \text{ mm} \times 30 \text{ }\mu\text{m}$  using a computer-controlled laser cutting machine. The ME ribbons were ultrasonically cleaned sequentially in ethanol and distilled water each for 20 min, then dried in an inert atmosphere.

The surfaces of the cleaned ME ribbons were covered with a layer of titanium (Ti) in thickness of 30 nm, followed by a layer of gold (Au) in thickness of 100 nm. The titanium inner layer was used to improve the adhesion of the gold film on the sensor surfaces, while the gold layer was exploited to enhance the immobilization process of sensing-elements (i.e., antibodies in this study) on the sensor surfaces and also to protect the ME ribbons from corrosion.

Compared with other works found in literature [123,124], polishing and annealing of the ME ribbons were not needed in our procedure

### 2.3.2 Antibodies immobilization

The ME sensor surfaces coated with gold and washed sequentially in ethanol and ultrapure water were functionalized by means of Antibodies (Abs) Human IgG produced in Goat, purchased by ImmunoReagents Inc. (Raleigh, NC, USA).

The adopted functionalization procedure was the Photochemical Immobilization Technique (PIT) [65], a powerful and quick methodology based on an appropriate UV-activation of Abs, whose effectiveness was already confirmed in several application for biosensing [28,68,73,107–109]. It was demonstrated that this method leads at the same time to a strong (covalent) binding of Abs onto gold surfaces while orienting Abs with one fragment antigen-binding site (Fab) exposed to the solution. As an immediate consequence, the antigen detection efficiency of the immunosensor is enhanced. The functionalization procedure via PIT involved the following steps: the ME sensor was mounted into a fluidic circuit and immersed in MilliQ water; a quartz cuvette containing 1 mL of Abs dissolved in ultrapure water ( $25 \mu\text{g}\cdot\text{mL}^{-1}$ ) was irradiated by UV light (lamp Trylight<sup>®</sup>) for 30 s, which is the optimal irradiation time for PIT; since the Abs binding sites remain active for about five minutes, immediately after the irradiation, the activated Abs solution was placed in the fluidic circuit and conveyed onto the ME sensor surfaces. The solution flowed into the closed fluidic circuit for several minutes.

In this study gold nanoparticles (AuNPs) and core@shell ( $\text{Fe}_3\text{O}_4\text{@Au}$ ) MNPs were used to amplify the biosensor response, in order to determine, for the same mass of the nanoparticles, whether the magnetic action produces an improvement in the sensitivity of the biosensor. The functionalization was again achieved by PIT for both types of nanoparticles (NPs). A volume of 1 mL of suspended NPs in MilliQ water was prepared, whereas a volume of 100  $\mu\text{L}$  of Abs solution ( $25 \mu\text{g}\cdot\text{mL}^{-1}$ ), irradiated by UV-light for 30 s, was added in twenty spikes (5  $\mu\text{L}$  each) to the NPs solution and gently stirred in order to avoid aggregation. The absorbance spectra of the functionalized NPs, characterized by the UV/vis spectrophotometer (model 6715 Jenway, Cole-Parmer<sup>®</sup> Company, Illinois USA), showed a red-shift of 3 nm of the LSPR wavelength, in accordance with the change of both types of NPs refractive index due to immobilization of antibody onto gold layer [28].

### 2.3.3 Synthesis of AuNPs

The AuNPs were synthesized by chemical reduction of tetrachloroauric(III) acid trihydrate ( $\text{HAuCl}_4\cdot 3\text{H}_2\text{O}$ ) through sodium citrate ( $\text{Na}_3\text{C}_6\text{H}_5\text{O}_7$ ) [125]. A solution of 50 mL of ultrapure water and 0.5 mL solvated  $\text{HAuCl}_4\cdot 3\text{H}_2\text{O}$  (24 mM) was heated up at 150 °C and stirred constantly. Afterwards, 6 mL of sodium citrate dihydrate (39 mM) was added into the boiling solution to achieve particle nucleation.

To further increase particle growth, another 4.2 mL of  $\text{HAuCl}_4 \cdot 3\text{H}_2\text{O}$  (24 mM) was added after 2 min. The color of the solution changed from transparent to black to finally move to bright red in few minutes. As final step, the solution was let cool down for 2 hours keeping the same stirring. In order to employ AuNPs as signal amplification factor, it was necessary to remove the sodium citrate, in which they were suspended to avoid aggregation, during the functionalization of the surface with Abs. The centrifuge protocol working conditions for 1 mL of citrate AuNPs (the dilution: 200  $\mu\text{L}$  of citrate AuNPs and 800  $\mu\text{L}$  of ultrapure water) was achieved through two steps: (a) 15 min at 9000 g, and (b) 10 min at 5000 g. After each centrifugation, the pellet was re-suspended in 1 mL ultrapure water.

The resulting optical density (OD) was  $\simeq 1.0$  that corresponds to  $\simeq 10^{11}$  AuNPs $\cdot\text{mL}^{-1}$  with average diameter of 40 nm [126].

#### **2.3.4 Au coating of $\text{Fe}_3\text{O}_4$ MNPs**

The magnetic  $\text{Fe}_3\text{O}_4$  nanoparticles (average diameter 30 nm) were purchased by MERCK (catalog number 747327) and gold coated as follows. 100  $\mu\text{L}$  of magnetic nanoparticles were added to a solution containing 50 mL of MilliQ water and sodium citrate (10  $\text{mg}\cdot\text{mL}^{-1}$ ) and they were heated until 90 °C with vigorous stirring. Once the temperature was reached, 50  $\mu\text{L}$  of  $\text{HAuCl}_4 \cdot 3\text{H}_2\text{O}$  (10  $\text{mg}\cdot\text{mL}^{-1}$ ) was added to the solution for four times every ten minutes. At this point the solution was let to cool down until it reached the room temperature keeping the same stirring. As a result of such a procedure a colloidal solution of 50 mL of  $\text{Fe}_3\text{O}_4$ @Au MNPs was obtained.

#### **2.3.5 Experimental setup**

The ME biosensor was mounted into a fluidic circuit by inserting it in a 3D printed Acrylonitrile butadiene styrene (ABS) cell that was subsequently placed in a glass tube to be connected to a fluidic continuous pump Figure 2.6.

Two identical home-made Helmholtz coils were mounted at a distance equal to their radius and employed to produce a static and uniform magnetic field in the central region between them, where the glass tube, enclosing the ME sensor, was placed.

A vector network analyzer (VNA) (E5071C ENA series, Keysight Technologies) was connected to a home-made cylindrical coil wound around the glass tube containing the ME sensor. The cylindrical single layer coil was made with 80 consecutive windings, using a copper wire (diameter of 0.1 mm), for a length of 8 mm and a diameter of 3.5 mm. The VNA, operating using S-parameters [127], was employed to provide an AC field to excite the ribbon and monitor the reflected signal from the

cylindric coil around the sensor. The reflection coefficient  $S_{11}$ , i.e., the ratio between the amplitude of the reflected signal and the amplitude of the incident one, is commonly used to monitor the resonance frequency of a ME resonator [19]. In fact,  $S_{11}$  signal reaches its minimum at a frequency corresponding to the resonance frequency,  $f_0$ , of the sensor.

The error of the experimental setup on a resonance frequency measure, extracted by fitting the signal obtained by the VNA, is of the order of  $10^{-2}$  Hz, much smaller than the error related to stability fluctuation over time of  $f_0$  (3 Hz as estimated in Paragraph 2.3.6).

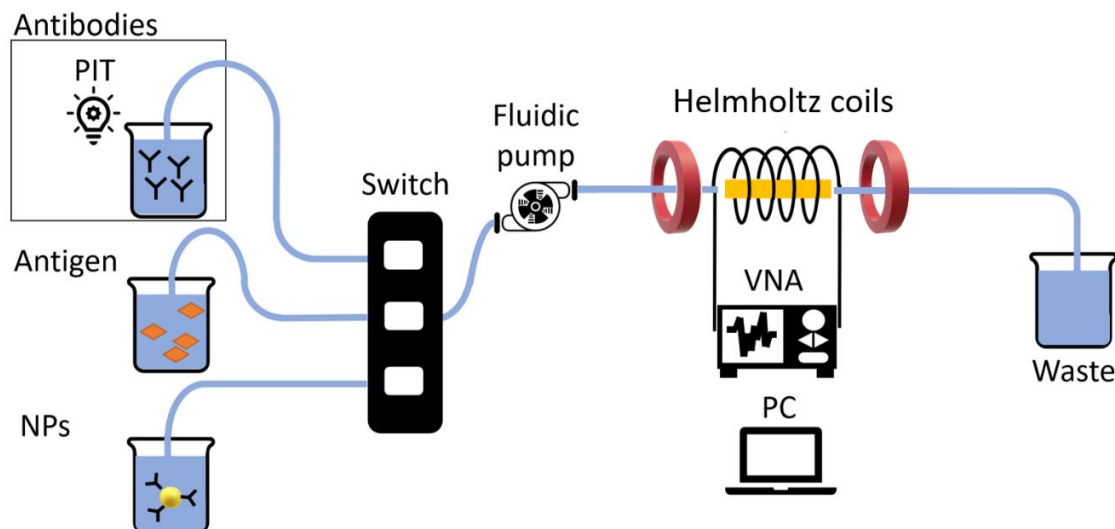


**Figure 2.6.** Schematic representation of the experimental setup. From left to right: the solution containing antibodies (activated via PIT), antigens and functionalized nanoparticles, fluidic channels and switch, fluidic (continuous) pump, Helmholtz coils, the ribbon enclosed by the cylindrical coil, the VNA connected to the PC and the flush out container (waste). A flow rate of  $5 \mu\text{L}\cdot\text{s}^{-1}$  was used in order to ensure laminar flow over the magnetoelastic sensor. Resonance frequencies were continuously monitored and recorded by the analyzer (VNA) and computer system (PC). Finally, the waste analyte was collected in the flush out container for disposal. Reproduced from [20].

### 2.3.6 Experimental procedure

Before starting the sample injection, the fluidic circuits (flow rate of about  $5 \mu\text{L}\cdot\text{s}^{-1}$ ) and the ME sensor were rinsed with MilliQ water.

A typical sensorgram reporting all the measurement steps is shown in Figure 2.7. In first step (I) a solution of  $25 \mu\text{g}\cdot\text{mL}^{-1}$  of UV-activated antibodies (anti-Human IgG produced in Goat) was conveyed to the cell for the surface functionalization (PIT). The decrease of the resonance frequency of the sensor makes evident that the functionalization took place correctly in just ten minutes. After the stabilization, the fluidic circuit was rinsed for five minutes with MilliQ water to remove the unbound Abs (II). Subsequently, a bovine serum albumin solution ( $50 \mu\text{g}\cdot\text{mL}^{-1}$ ) flowed into the fluidic circuit for five minutes to fill possible free space left by Abs on the gold surface (blocking, step III). In the step IV a solution of target antigen (Human IgG) flowed into the circuit for fifteen minutes. After the rinse (step V) a solution (1 mL) of functionalized  $\text{Fe}_3\text{O}_4\text{@Au}$  MNPs was conveyed to the cell (step VI). As it can be noticed looking at Figure 2.7, the  $\text{Fe}_3\text{O}_4\text{@Au}$  MNPs play an important role since the

ME sensor response is eventually amplified by a factor slightly greater than 3 at this intermediate concentration. We highlight that all the steps were carried out until the equilibrium condition was reached thereby making more robust the whole approach. For each detection step the time to achieve a reliable stability was approximately five minutes, thus we carried out long term stability measurements (blue line in Figure 2.7), which we used to analyze the distribution of the means of the resonance frequency measured over intervals of five minutes. It turned up that the standard deviation ( $\bar{\sigma}_f$ ) of such a distribution was 1 Hz so that 3 Hz (3 SD) was used to determine the threshold to establish the occurrence of a signal (limit of detection).

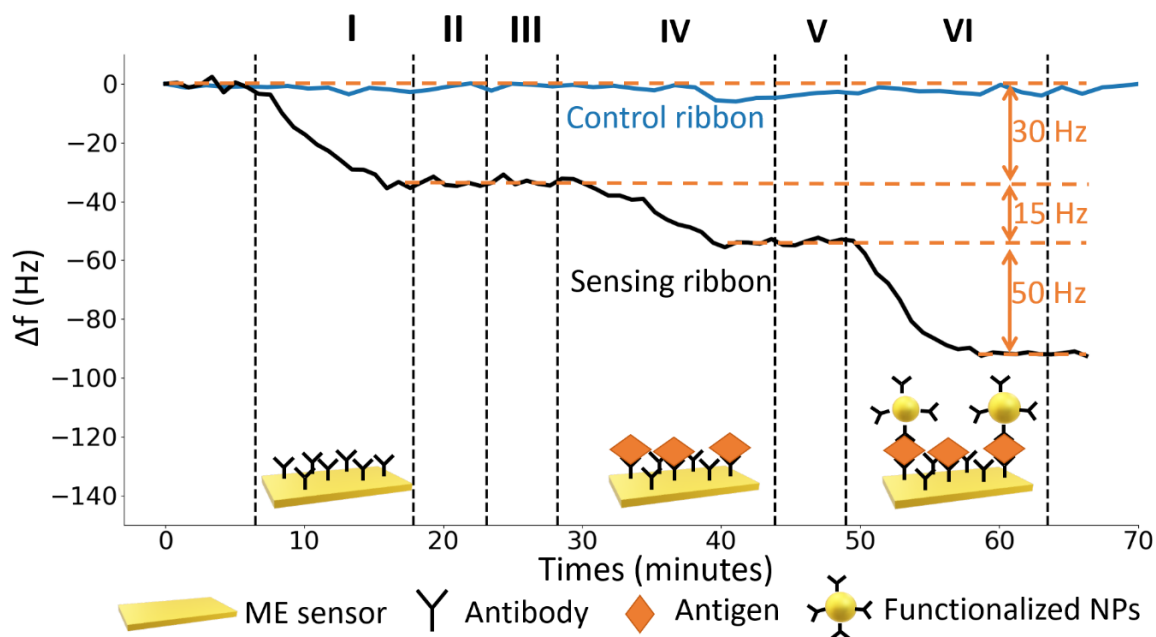


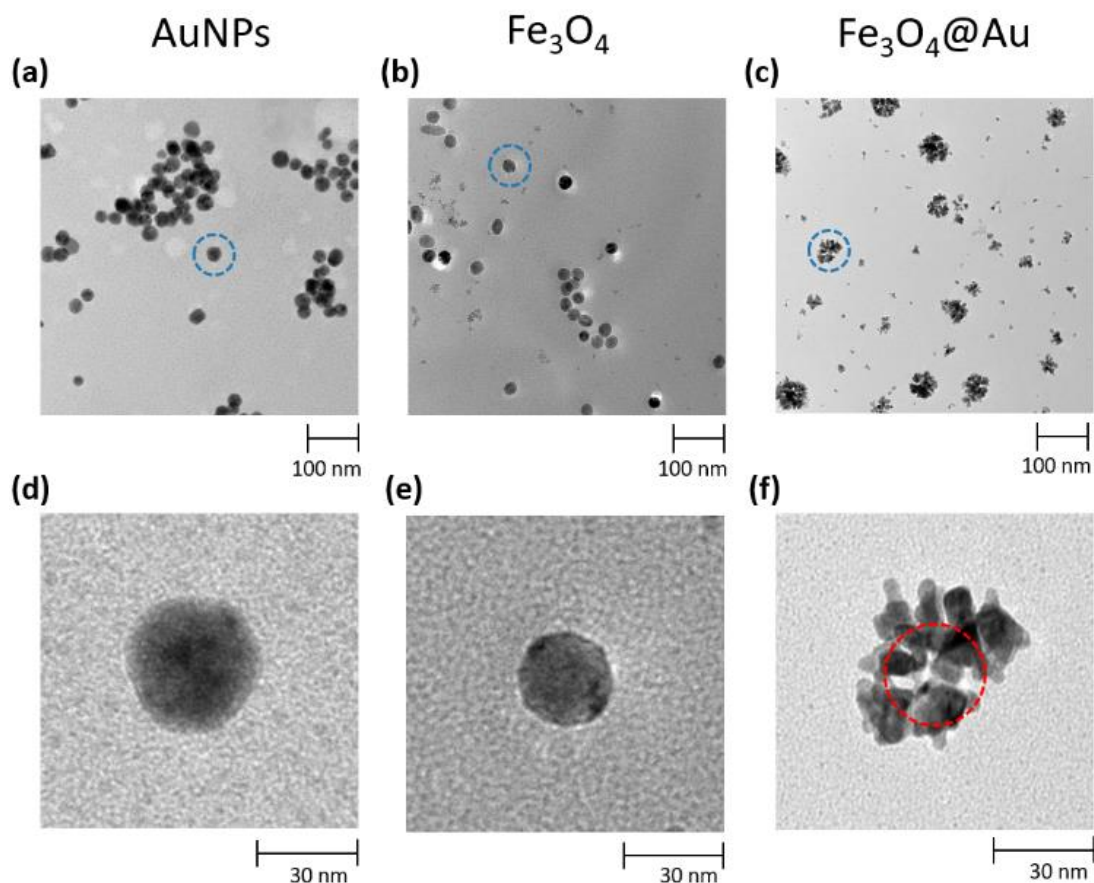
**Figure 2.7.** Typical dynamic response of the ME biosensor. On the y-axis the shift of the resonance frequency  $f_0$  due to the mass loading and on the x-axis the time interval. The black line represents the response of the sensing ribbon in each of the following steps: (I) functionalization with a solution of  $25 \mu\text{g}\cdot\text{mL}^{-1}$  of UV-activated antibodies, (II) rinse with MilliQ water, (III) flowing of bovine serum albumin solution ( $50 \mu\text{g}\cdot\text{mL}^{-1}$ ), (IV) flowing of target antigen solution ( $5 \mu\text{g}\cdot\text{mL}^{-1}$ ), (V) rinse with MilliQ water, (VI) amplification with core@shell magnetic MNPs ( $\text{Fe}_3\text{O}_4@Au$ ). The control ribbon, that was employed to estimate the noise level, is represented by a blue line. Reproduced from [20].

## 2.4 Results

### 2.4.1 Characterization of $\text{Fe}_3\text{O}_4@Au$ MNPs

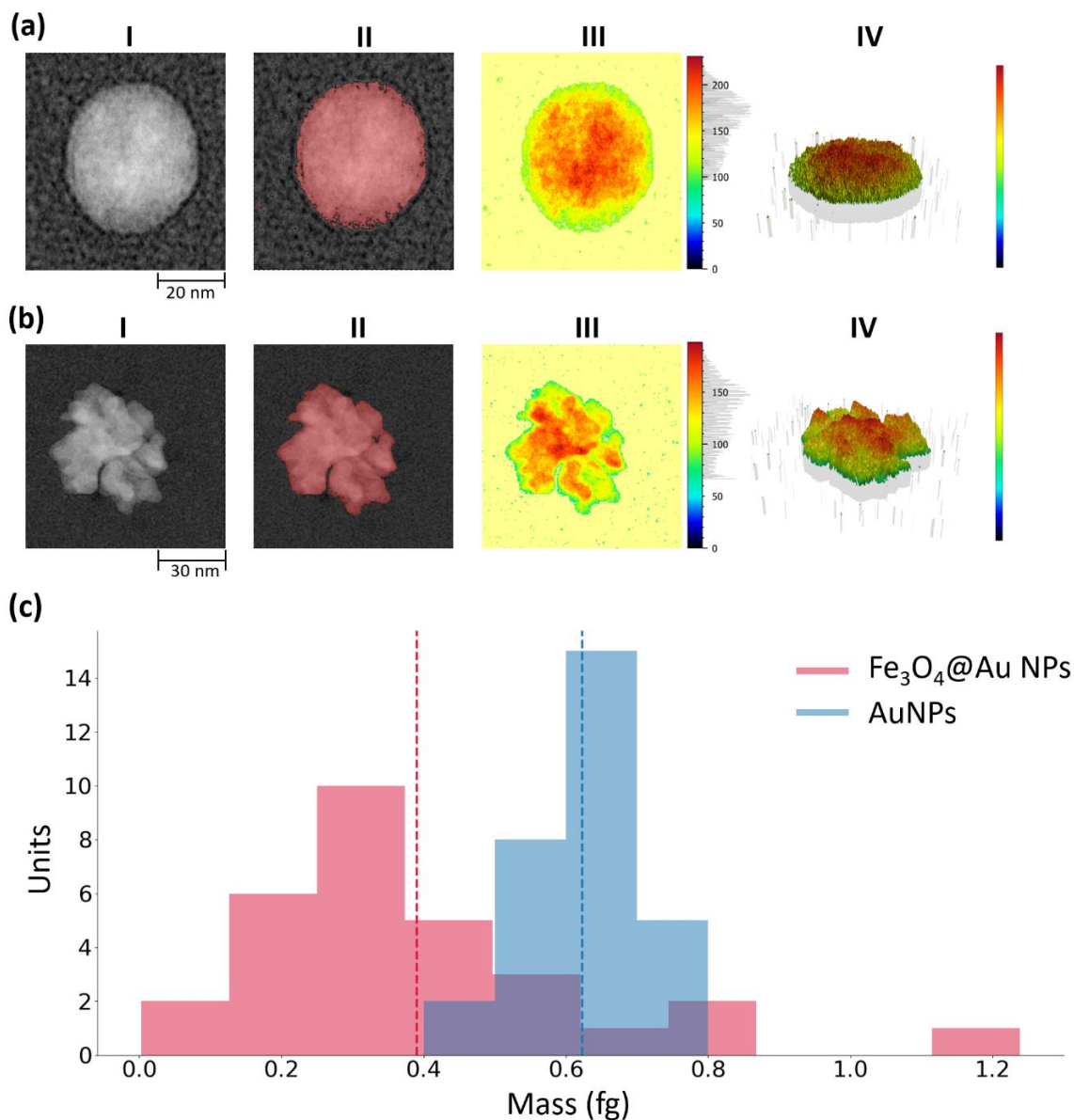
Transmission electron microscopy (TEM) micrographs were collected using a FEI Tecnai G2 S-twin apparatus (University of Naples Federico II, Italy) operating at 200 kV (LaB6 source). The particle powder samples were transferred on carbon-coated copper grids (200 mesh) by dispersing them in ethanol and then adding one drop on the copper grid and evaporating the solvent.

Figure 2.8 shows the TEM micrograph of AuNPs synthesized according to the abovementioned protocol (a) as well as the  $\text{Fe}_3\text{O}_4$  MNPs before (b) and after (c) the gold coating ( $\text{Fe}_3\text{O}_4@Au$  MNPs).



**Figure 2.8.** TEM micrographs of (a) AuNPs, (b)  $\text{Fe}_3\text{O}_4$  NPs and (c)  $\text{Fe}_3\text{O}_4@Au$  core@shell MNPs.  $\text{Fe}_3\text{O}_4$  (gold nanoflower grown on a magnetic core). In the lower part of the figure the circled portions in panels (a,b,c) are respectively reported in detail in panels (d,e,f). In panel (f) the magnetic core is highlighted with a red circle. Reproduced from [20].

The mass distribution of the AuNPs and  $\text{Fe}_3\text{O}_4@Au$  NPs, which was crucial in order to construe the results related to signal amplification, was assessed by applying the software SPIP Mountains 8 to the TEM micrographs (Figure 2.9a,b). The nanoparticle of interest was considered and extracted from the collective TEM micrograph (I), the contour of the nanoparticles was detected and distinct by the background (II), then the particle surface (III) together with its 3D rendering (IV) were generated. The latter was employed to estimate the volume of the object. Once the volume of the nanoparticle had been estimated, its mass was obtained by multiplying by the density of the  $\text{Fe}_3\text{O}_4$ . In Figure 2.9 the mass distribution of AuNPs (blue histogram) and of  $\text{Fe}_3\text{O}_4@Au$  MNPs (red histogram) are compared. Each nanoparticle employed for the mass analysis was extracted randomly from collective TEM micrographs. The two mass distributions (Figure 2.9c) turned out to be unimodal distributions with the picks around the value 0.4 fg for  $\text{Fe}_3\text{O}_4@Au$  NPs (red histogram) and 0.63 fg for AuNPs (blue histogram). The standard deviations are respectively 0.2 fg and 0.09 fg. Thus, the masses of AuNPs and  $\text{Fe}_3\text{O}_4@Au$  NPs result to be of the same order of magnitude.



**Figure 2.9.** The steps of the protocol employed to estimate the mass of AuNPs (a) and Fe<sub>3</sub>O<sub>4</sub>@Au NPs (b) using the software SPIP Mountains 8. The nanoparticle of interest was considered and extracted from the collective TEM micrograph (I), the contour of the nanoparticles was detected and distinct by the background (II), then particle surface (III) and its 3D rendering (IV) were generated. The latter was employed to estimate the volume of the object. (c) Mass distribution of AuNPs and Fe<sub>3</sub>O<sub>4</sub>@Au NPs (core@shell NPs). The mean and the standard deviation for the mass distributions were  $0.4 \pm 0.2$  fg for Fe<sub>3</sub>O<sub>4</sub>@Au NPs and  $0.63 \pm 0.09$  fg for AuNPs. Each nanoparticle employed for the mass analysis was extracted randomly from collective TEM micrographs. Reproduced from [20].

#### 2.4.2 Comparison between AuNPs and Fe<sub>3</sub>O<sub>4</sub>@Au MNPs

The idea of taking advantage of the magnetic interaction between magnetite nanoparticles and ME ribbons has already been employed in the past to detect bacteria [128]. In that case, Fe<sub>3</sub>O<sub>4</sub> nanoparticles were modified by using chitosan, a linear polysaccharide, so that their surface was charged positively. In this way, in specific conditions, the nanoparticles bind to negatively charged bacteria as *E. coli* and therefore, thanks to magnetic attraction, they also bind to the surface of the ME sensor giving rise to a signal enhancement. This approach has several drawbacks. Firstly, the chitosan coating and the *E. coli* binding process are expensive and time consuming (several hours);

and furthermore, the whole procedure has to be carried out under controlled conditions, this preventing the application to complex matrices. Secondly, since the adhesion between bacteria and nanoparticles results from the electrostatic interaction between bacteria and the chitosan, it is expected that the specificity will be greatly compromised when other gram-negative bacteria are present in the sample. To circumvent such limitations, we functionalized the gold surface of  $\text{Fe}_3\text{O}_4@Au$  MNPs with the antibodies targeting antigen, in this way achieving high specificity for the nanoparticle-antigen interaction.

Moreover, the magnetic core of the nanoparticles still played an important role since the (specific) nanoparticle-antigen bond is somehow catalyzed and enforced by the interaction between the magnetic dipole moment of the  $\text{Fe}_3\text{O}_4@Au$  MNPs and the strong local magnetic field. The occurrence of the latter process can be deduced by the results shown in Figure 2.10, in which the response signals obtained by exposing the sensor to  $1 \mu\text{g}\cdot\text{mL}^{-1}$  of antigen solution and amplifying once with AuNPs (blue line) and once with  $\text{Fe}_3\text{O}_4@Au$  MNPs (red line) are reported. Even though their mass was smaller (Figure 2.9c),  $\text{Fe}_3\text{O}_4@Au$  MNPs were able to amplify the frequency shift by a larger amount (Figure 2.10) thereby demonstrating the higher sensitivity that can be achieved when the additional tool provided by magnetic moment is exploited.

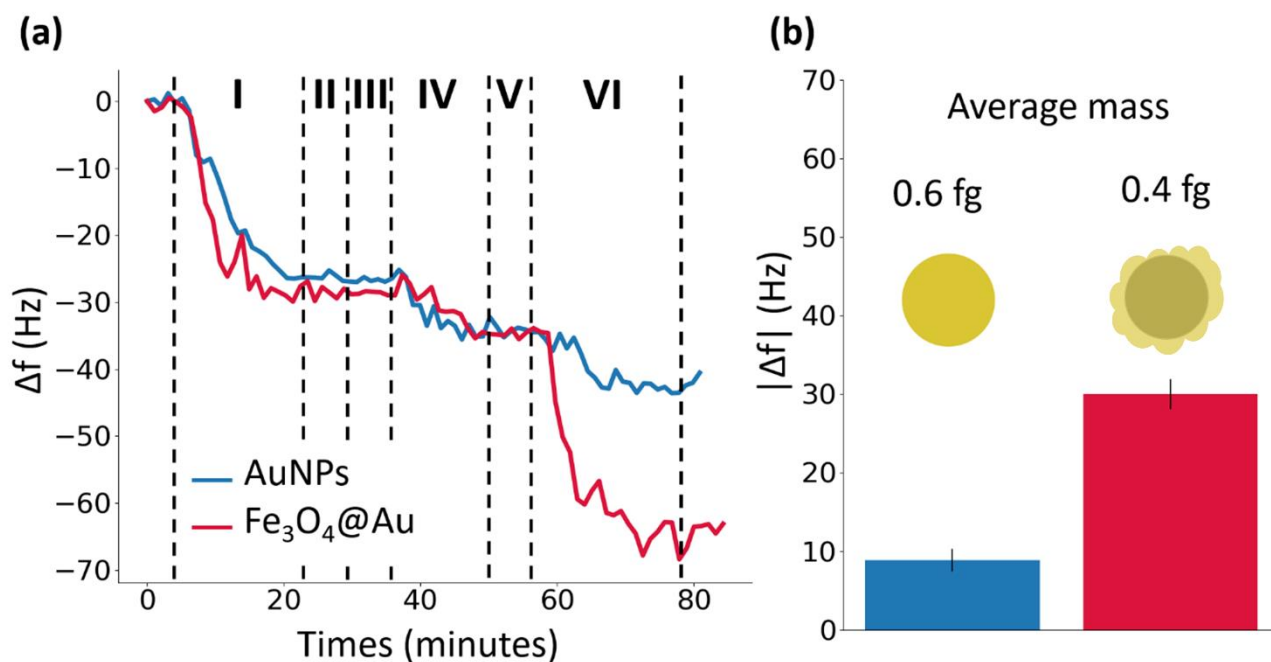


**Figure 2.10.** Comparison between the amplification effects due to AuNPs and  $\text{Fe}_3\text{O}_4@Au$  MNPs. (a) The blue and the red lines represent the response of the sensing ribbon to the following steps: (I) functionalization with  $25 \mu\text{g}\cdot\text{mL}^{-1}$  of UV-activated antibodies (anti-Human IgG) which causes a shift of the resonance frequency  $\Delta f \approx 30$  Hz; (II) rinse with MilliQ water; (III) flowing of bovine serum albumin solution ( $50 \mu\text{g}\cdot\text{mL}^{-1}$ ); (IV) exposure to the antigen solution (Human IgG) which causes a shift  $\Delta f \approx 10$  Hz; (V) rinse with MilliQ water; (VI) amplification with AuNPs for the blue line and amplification with  $\text{Fe}_3\text{O}_4@Au$  MNPs for the red line. The former causes a shift  $\Delta f = 9 \pm 1$  Hz while the latter causes a shift  $\Delta f = 30 \pm 2$  Hz. (b) A direct comparison between the amplification of the response signal due to AuNPs (blue) and  $\text{Fe}_3\text{O}_4@Au$  MNPs (red). Reproduced from [20].

### 2.4.3 Detection of Human IgG

The dose–response curve, i.e., resonance frequency shifts  $\Delta f$  versus Human IGg concentrations, is reported in Figure 2.11 together with the best fit of the experimental data provided by a Langmuir isotherm curve [129]:

$$f(x) = a \frac{x}{x + C} \quad 2.24$$

where  $a = 68.9 \pm 0.5$  Hz and  $C = 1.25 \pm 0.04$   $\mu\text{g mL}^{-1}$  are the asymptotic value, and the concentration at which the frequency shift reaches the 50% of its maximal value, respectively. We carried out every experiment with a different ribbon obtaining coherent results. This is a strong confirm of the robustness of the experimental setup with respect to fluctuations related to differences in the fabrication process of ME sensors. The dose-response curve exhibits signal saturation at concentrations larger than  $10 \mu\text{g}\cdot\text{mL}^{-1}$ , thus showing that the ME immunosensor is able to provide a quantitative measurement over two decades. The error on each experimental point of the dose response curve was estimated by propagating the errors of the resonance frequency values in the equilibrium states before and after the amplification with  $\text{Fe}_3\text{O}_4@Au$  MNPs. The error of the resonance frequency of an equilibrium state was estimated as the standard deviation of the measured values in a time interval of five minutes. The limit of detection (LOD) was assessed inserting the error estimated in Section 3.6 ( $3 \cdot \bar{\sigma}_f = \pm 3$  Hz) in Equation 2.24 and turned up to be lower than  $0.1 \mu\text{g}\cdot\text{mL}^{-1}$  (0.66 nM).

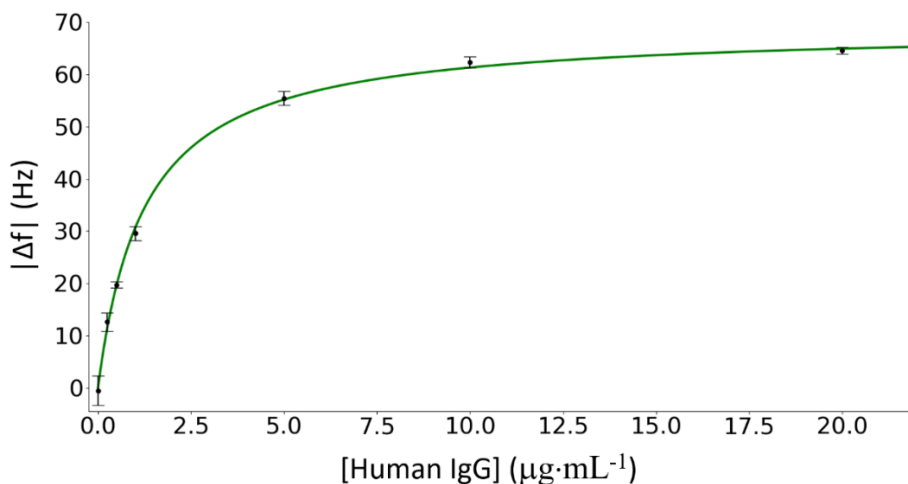


**Figure 2.11.** Dose–response curve, i.e., resonance frequency shifts  $\Delta f$  versus Human IGg concentrations. Experimental data are fitted by Langmuir isotherm curve (Equation 2.24). The range of tested concentrations varies from the zero concentration to  $20 \mu\text{g}\cdot\text{mL}^{-1}$ . Each concentration has been tested using different ribbons. Reproduced from [20].

## 2.4.4 Specificity assay

To ascertain the sensor specificity, the same experimental procedure was used to test the ME sensor with similar compounds. In the present case, we measured the response of the immunosensor to a mixture Rabbit IgG produced in sheep and Mouse IgG produced in goat at a concentration of  $20 \mu\text{g}\cdot\text{mL}^{-1}$  each, whose sensorgram is shown in Figure 2.12. As it is clearly visible, only the shift resulting from the surface functionalization is visible, whereas no additional frequency shift is measured as a result of the presence of Rabbit and Mouse IgGs. This is true even when  $\text{Fe}_3\text{O}_4\text{@Au}$  MNPs are conveyed into the interaction cell (step VI). The high specificity of the immunosensor is largely a consequence of the excellent biorecognition properties of the antibodies.

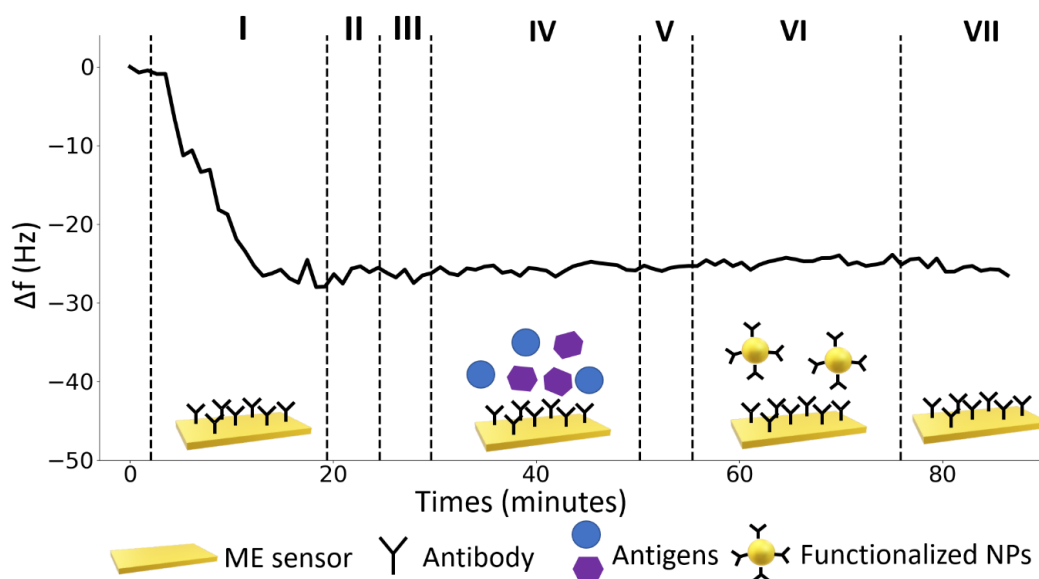


**Figure 2.12.** Sensor specificity. ME sensor responses to a mixed solution of Rabbit IgG produced in sheep and Mouse IgG produced in goat. The black line represents the response of the sensing ribbon in each of the following steps: (I) functionalization with a solution of  $25 \mu\text{g}\cdot\text{mL}^{-1}$  of UV-activated antibodies, (II) rinse with MilliQ water, (III) flowing of bovine serum albumin solution ( $50 \mu\text{g}\cdot\text{mL}^{-1}$ ), (IV) flowing of Rabbit IgG produced in sheep and Mouse IgG produced in goat solution both at a concentration of  $20 \mu\text{g}\cdot\text{mL}^{-1}$ , (V) rinse with MilliQ water, (VI) amplification with  $\text{Fe}_3\text{O}_4\text{@Au}$  MNPs, (VII) rinse with MilliQ water. Reproduced from [20].

## 2.5 Discussion

### 2.5.1 Modeling the interaction among ME sensor and $\text{Fe}_3\text{O}_4\text{@Au}$ MNPs

The magnetic force acting on each  $\text{Fe}_3\text{O}_4\text{@Au}$  MNP is:

$$\mathbf{F}(\mathbf{r}) = \nabla(\mathbf{m} \cdot \mathbf{B}_{\text{tot}}) \quad 2.25$$

where  $\mathbf{m}$  is the magnetic moment of a  $\text{Fe}_3\text{O}_4\text{@Au}$  MNP and  $\mathbf{B}_{\text{tot}} = \mathbf{B}_H + \mathbf{B}$  is the magnetic induction field generated by the Helmholtz coils ( $\mathbf{B}_H$ ) and the ME ribbon ( $\mathbf{B}$ ), respectively. The magnetic induction field produced by Helmholtz coils is directed along the  $z$ -axis (Figure 2.13a) and

can be considered uniform in the region around the ribbon. On the contrary, the magnetic induction field produced by the ME ribbon is not uniform and can be worked out by considering the ribbon as rectangularly shaped permanent magnet whose significant components can be written as [100,130]:

$$B_x(x, y, z) = \frac{\mu_0 M}{4\pi} \sum_{k=1}^2 \sum_{m=1}^2 (-1)^{k+m} \ln \left[ \frac{(y - y_1) + [(x - x_m)^2 + (y - y_1)^2 + (z - z_k)^2]^{\frac{1}{2}}}{(y - y_2) + [(x - x_m)^2 + (y - y_2)^2 + (z - z_k)^2]^{\frac{1}{2}}} \right] \quad 2.26$$

$$B_z(x, y, z) = \frac{\mu_0 M}{4\pi} \sum_{k=1}^2 \sum_{n=1}^2 \sum_{m=1}^2 (-1)^{k+m+n} \tan^{-1} \left[ \frac{(x - x_n)(y - y_m)}{(z - z_k)[(x - x_n)^2 + (y - y_m)^2 + (z - z_k)^2]^{\frac{1}{2}}} \right] \quad 2.27$$

where  $\mu_0$  is the magnetic permeability of free space,  $x_1, x_2, y_1, y_2, z_1, z_2$  are the positions of the edges of the ribbon with respect to  $x, y$  and  $z$ -axis (Figure 2.13a).

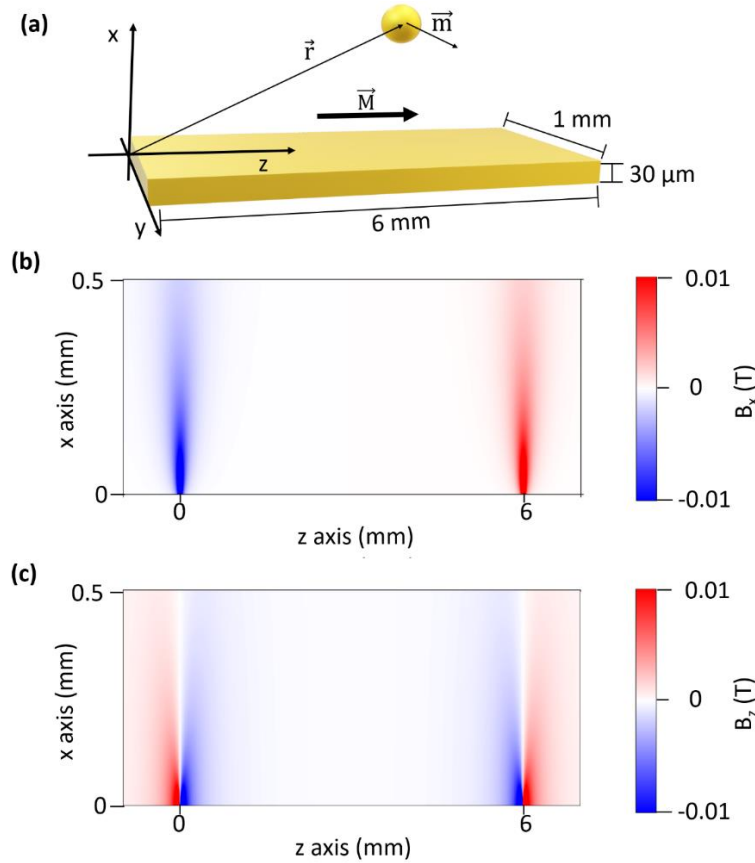


**Figure 2.13.** a) Schematic representation of the interaction among the  $\text{Fe}_3\text{O}_4\text{@Au}$  MNP magnetic nanoparticle and the magnetoelastic ribbon.  $\vec{M}$  is the magnetization of the ME ribbon,  $\vec{m}$  is the magnetic moment of the  $\text{Fe}_3\text{O}_4\text{@Au}$  MNP and  $\vec{r}$  indicates the position in the chosen reference system. b) and c) Intensity of the  $x$  and  $z$  components of the magnetic induction field ( $B_x$  and  $B_z$ ) in the symmetry plane  $x$ - $z$  of the ribbon ( $y = 0.5$  mm). Reproduced from [20].

The saturation magnetization  $\vec{M}$  of the ribbon is oriented along the  $z$ -axis and the value of  $\mu_0 \vec{M}$  is approximately 0.2 T for Metglas [131]. The component  $B_y$ , can be neglected since it is always much smaller than  $B_x$  and  $B_z$  while the latter are of the same order of magnitude and reach their maximum nearby the ribbons ends (Figure 2.13b). The dependence of  $B_x$  and  $B_z$  on  $x, y$  and  $z$  variables in Figure

2.13 suggests that the significant magnetic interactions are limited to a region with volume  $S_{xyz} = 100 \mu\text{m} \times 1 \text{mm} \times 100 \mu\text{m}$  close to the ends of the ribbon. In this region the magnetic field produced by the Helmholtz coils is negligible with respect to  $B_x$  and  $B_z$  and does not contribute significantly to the nanoparticles' magnetization ( $B_H \approx 50 \text{ Oe}$ ).

The magnetic moment,  $\mathbf{m}$ , of a  $\text{Fe}_3\text{O}_4@Au$  MNP is the product of its magnetization,  $\mathbf{M}_{NP}$ , and volume,  $V_m = \frac{4}{3}\pi R_m^3$ , where  $R_m$  is the radius of its magnetic core,  $\mathbf{m} = \mathbf{M}_{NP} V_m$ . The volumetric magnetization is induced by the external magnetic induction field,  $\mathbf{M}_{NP} = \frac{\Delta\chi}{\mu_0} \mathbf{B}$ , where  $\Delta\chi = \chi_{MNP} - \chi_{water} \approx \chi_{MNP}$  is the effective susceptibility of a magnetic nanoparticle with respect to the medium (water). Since the component of the magnetic induction field along the  $y$ -axis is negligible, the magnetic moment of a  $\text{Fe}_3\text{O}_4@Au$  MNP lies on the  $x$ - $z$  plane. The order of magnitude of the magnetic moment can be retrieved by the hysteresis cycles of  $\text{Fe}_3\text{O}_4$  superparamagnetic nanoparticles provided by the seller and reported in Figure 2.14, also considering the effect of the diamagnetic gold shell that weakens magnetic properties [132].

## Hysteresis loop of $\text{Fe}_3\text{O}_4$ NPs

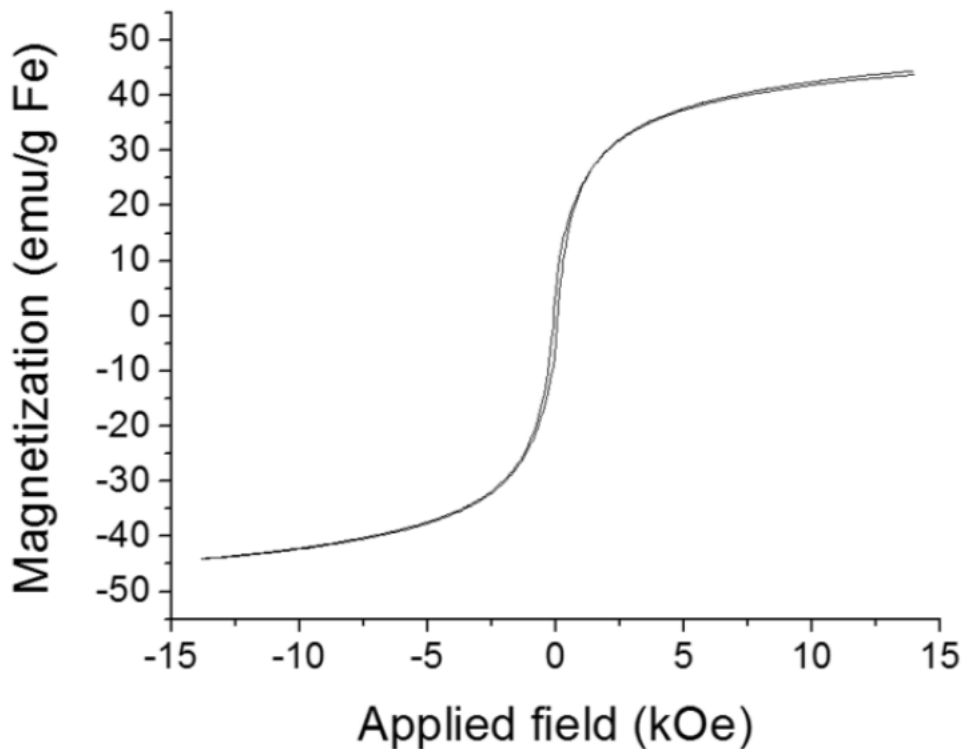


**Figure 2.14.** Room-temperature M-H curve of the magnetite samples [supplied by the nanoparticles manufacturer (Ocean Nano Tech, LLC)] measured by cycling the external magnetic field between  $-14000 \text{ Oe}$  and  $14000 \text{ Oe}$ . This magnetization curve shows a very small hysteresis behavior for the samples and exhibits small values of coercive field and remnant magnetization. This indicates that the nanoparticles can safely be considered as superparamagnetic. Reproduced from [20].

The intensity of external magnetic induction field was high enough to induce significant magnetization, but only in the linear range of the magnetic response so the magnetic susceptibility could be considered constant in our case.

Thus, the attractive magnetic force between the ribbon and a Fe<sub>3</sub>O<sub>4</sub>@Au MNP is:

$$F_x(x, y, z) = -\frac{\partial(-\mathbf{m} \cdot \mathbf{B})}{\partial x} = \frac{V_m \Delta \chi}{\mu_0} \left( 2B_x \frac{\partial B_x}{\partial x} \cos \theta + 2B_z \frac{\partial B_z}{\partial x} \sin \theta \right) \quad 2.28$$

where  $\theta$  denotes the angle between the magnetic moment  $\mathbf{m}$  and the  $x$ -axis. From the analysis of Equations 2.26 and 2.27 along the  $x$ -axis, we have  $B_x \approx B_z$ , Figure 2.13b,c which entails  $\cos \theta \approx \sin \theta \approx \frac{\sqrt{2}}{2}$  and  $\frac{\partial B_x}{\partial x} \approx \frac{\partial B_z}{\partial x} \approx 1 \text{ T} \cdot \text{mm}^{-1}$ ; thus Equation 2.28 can be approximated as follows:

$$F_x(x, y, z) \approx 2\sqrt{2} \frac{V_m \Delta \chi}{\mu_0} B_x(x, y, z) \left[ \frac{\partial B_x}{\partial x} \right]. \quad 2.29$$

The force in Equation 2.29 bends the nanoparticles velocity field lines towards the ribbon thereby increasing the local density of the Fe<sub>3</sub>O<sub>4</sub>@Au MNP. The order of magnitude of the bending can be estimated as the displacement induced by  $F_x(x, y, z)$  acting on a nanoparticle in the region where the force is non-vanishing, i.e. the region  $S_{xyz}$  previously defined. The mean force  $\bar{F}_x$  acting on a Fe<sub>3</sub>O<sub>4</sub>@Au MNP can be evaluated by averaging  $F_x(x, y, z)$  in the region  $S_{xyz}$ . According to the Stokes law, for a spherical particle with radius  $r$ , the displacement caused by the mean force  $\bar{F}_x$  is:

$$\Delta s_m \approx \mu \bar{F}_x t_l, \quad 2.30$$

where  $\mu = (6\pi\eta r)^{-1}$  is the mobility,  $t_l$  the time during which the interaction takes place. It should be noted that this approach is valid in the approximation that the motion is uniform along  $x$ , a condition well satisfied in our case since the limit velocity is reached within a very short time-interval ( $\tau \approx 10^{-6}$  s). The time  $t_d$  in which the magnetic interaction takes place can be estimated as  $t_d = d \cdot v_{flux}^{-1} \approx 1$  s, where  $v_{flux} \approx 100 \mu\text{m} \cdot \text{s}^{-1}$  is the longitudinal velocity of the liquid inside the channel and  $d \approx 100 \mu\text{m}$  the size of  $S_{xyz}$  along  $z$ -axis. Eventually, Equation 2.30 provides  $\Delta s_m \approx 20 \mu\text{m}$  that leads to an increase of the frequency collision between nanoparticles and the ribbon surface whereby more antigens (Human IgGs) captured on the surface are ballasted by nanoparticles.

The significance of such a bend arises from its comparison to the Brownian motion displacement [133]

$$\Delta s_B = \sqrt{2Dt_D}, \quad 2.31$$

where  $D$  is the diffusion coefficient ( $D = \mu k_b T \approx 10 \text{ m}^2 \cdot \text{s}^{-2}$ ) and  $t_D$  the diffusion time, which we can estimate by requiring  $\Delta s_B \approx \Delta s_m$ . Thus, from Equations 2.30 and 2.31, we obtain  $t_D \approx 40 \text{ s}$ , a time much longer than the transit time of the  $\text{Fe}_3\text{O}_4@Au$  MNPs over the ME ribbon, which implies that the velocity field lines remain bent by magnetic force along the whole length of the ribbon. This view is confirmed by the analysis of the energy scales involved. The binding energy between the antibodies and the antigen is of the order of  $1.6 \cdot 10^{-19} \text{ J}$  (1 eV), which is larger than the thermal energy at room temperature ( $k_B T = 0.04 \cdot 10^{-19} \text{ J} = 0.025 \text{ eV}$ ). Interestingly, the potential well due to the magnetic induction field averaged over the region of interest  $S_{xyz}$ , is of the order of  $k_B T$  thus making consistent the description about the role played by the strong magnetic induction field at the edge of the ribbon in bending the velocity field lines and increasing the “effective” nanoparticle density, but without giving rise to any non-specific interaction with nanoparticles and the surface of the ribbon.

### 2.5.2 Future research directions

The ME-based biosensor presented here has proven to be a high-performing, rapid and reliable sensing technology that works effectively in water with a limit of detection (LOD) lower than 1 nM for an antigen as Human IgG.

Compared with other sensing technologies, the ME-based sensor takes advantage of some features common to all magnetoelastic sensors. Indeed, they are simple in design and can be produced in small size using standard manufacturing procedures; they are very inexpensive so that the cost of manufacturing of these sensors is mainly the sensing element (i.e., antibody in this study), which is the same for all biological detection technologies. Therefore, these sensors can be used as disposable sensors. Furthermore, they are wireless, eliminating the need for direct physical contacts, thus favoring their use in real time applications such as detection in conductive liquids or in sealed and opaque containers, and biological experiments such as monitoring of blood flow chemistry. In addition to these features, the ME-based biosensor presented in this study, profits from the synergy with PIT allows a fast and efficient functionalization, contributing to the rapidity of the detection measure, which lasts approximately one hour. Moreover, PIT does not require complex chemical procedures, skilled personnel or laboratories, thus increasing the possibility of turning the biosensor into a portable device, suitable to perform real time and in situ detections.

It should be mentioned that the possibility to functionalize surfaces in few minutes and not in laboratory conditions are key features that are not common to other experimental setups. Among all the possible functionalization strategies, self-assembled monolayers (SAMs) is currently one of the most widespread methods. Despite the advantages they offer in many applications, there are important drawbacks that should be considered to correctly evaluate their potential for on field applications. Firstly, despite SAMs on gold surfaces are often usually represented as compact monolayers, the

realization of a well-assembled monolayer strongly relies on attention to details (i.e., the purity of the solutions used and the presence of even a low amount of contaminants [61]), that makes it not suitable for on field applications. On the other hand, an on field SAMs functionalization before detection would take several hours to be implemented.

In this scenario, the advantages of combining PIT and the ME-based immunosensor are of great interest for environmental control and food safety applications, such as the detection of pesticides in water samples. Among the different pesticides, the glyphosate [(N-(phosphonomethyl)glycine)] is the most used herbicide worldwide. Due to its high solubility in water, there is a need of investigating its residual applications directly in fields for monitoring the contamination of aquatic environments [134]. Currently, there exist several high-sensitive analytical techniques to detect pesticides, including glyphosate, mostly based on gas and liquid chromatography coupled with mass spectrometry [135]. However, their complexity prevents the opportunity of performing in situ and real-time analysis. Therefore, several types of biosensor-based technologies have emerged as promising tools for rapid on-site analysis of samples [136,137]. Among all types of biosensors, immunosensors techniques have already gained attention in the last decade, proving their effectiveness in this field.

The stability in water of the ME biosensor, the rapidity of sample analysis and the possibility of turning the sensor into a portable device are essentials characteristics for future applications in detecting glyphosate. In addition, a sensitivity adequate to the legal limits of glyphosate concentrations is required. The European Union settled the maximum residue limit of glyphosate in drinking water to  $0.1 \mu\text{g}\cdot\text{L}^{-1}$  (i.e., 0.5 nM), while in the United State of America the established limit is  $700 \mu\text{g}\cdot\text{L}^{-1}$  (i.e., 4  $\mu\text{M}$ ) [Directive 2006/118/EC, Directive 2006/118/EC, USEPA. EPA 816-F-09-004]. The ME immunosensor shows a LOD of 0.66 nM for the tested antigen, which is well below the maximum concentration allowed in the United State of America and of the same order of magnitude of the European one, thereby suggesting future applications to the detection of pesticides in water.

## 2.6 Conclusions

In this Chapter a high-performance magnetoelastic (ME) biosensor for wireless recognition of antigens in liquid is presented. The surface of the biosensor is functionalized with antibodies by using a very effective immobilization technique (Photochemical Immobilization Technique, PIT). The performances of the device were tested with Human IgG and different ribbons were used for each measurement. An innovative signal amplification method has also been introduced which exploits

core@shell magnetic nanoparticles ( $\text{Fe}_3\text{O}_4@\text{Au}$ ) so to exploit both the magnetic effect due to the core and the gold nanoflowers on the surface, the latter being effective in tethering antibodies by PIT. The results obtained with magnetic nanoparticles have been compared with those obtained with gold nanoparticles, showing that the magnetic character of the former plays a crucial role for improving the performance.

PIT was used here for the first time to functionalize a ME biosensor, allowing us to carry out the whole measurement in about 1h. The limit of detection (LOD) lower than 1 nM paves the way to its applications to environmental and food safety for on field measurements.

## Chapter 3. Colorimetric biosensor

In this Chapter a simple, easy-to-use and efficient colorimetric immunosensor that exploits spinning gold coated magnetic nanoparticles (MNPs@Au) in a rotating magnetic field is presented. The proposed biosensor was tested against glyphosate in tap water. Glyphosate is the most widely used herbicide in the world and increasingly sensitive methods are studied to detect it. On one hand, the gold shell of the MNPs@Au provided a sensitive optical transduction of the biological signal – through the shift of the local surface plasmon resonance (LSPR) entailed by the nanoparticle aggregation –, but it also allowed us to use an effective photochemical immobilization technique to tether oriented antibodies onto nanoparticles directly to its surface. While such a feature led to aggregates in which the nanoparticles were at close proximity to each other so that the resonance shift could take place, the magnetic properties of the core offered us an efficient tool for self-assembly of nanoparticles in chain-like agglomerates and for stirring the solution by a rotating magnetic field. The dynamic motion of these non-spherical agglomerates under the magnetic field torques induced a turbulent flow enhancing the mixing performance of the system. The resulting micromixing inherently facilitated the encounters among nanoparticles and glyphosate, as well as the specific aggregation among nanoparticles, with significant advantages for target recognition. As a matter of fact, the combination of these features allowed us to reach a limit of detection of  $20 \text{ ng}\cdot\text{L}^{-1}$ , the latter being lower than that legally permitted in food according to several authorities. As for most immunosensors, the recognition of targets by antibodies warrants high specificity and the whole procedure can be easily extended to similar analytes making the colorimetric approach described here an interesting tool for on-site detection or even POC diagnosis.

**Paragraph 3.1** contains an overview of the content outlined in the Chapter highlighting the novelty points and scope of the work. **Paragraph 3.2** provides the theoretical basis for understanding the phenomenon of the LSPR. The materials and methods exploited to carry out the experiments are described in **Paragraph 3.3**. In **Paragraph 3.4** are presented the results related to core@shell MNPs characterization and biosensing. **Paragraph 3.5** is devoted to the discussion of the results: a semi-quantitative interpretation of the micromixing effect obtained by means of core@shell MNPs is proposed and the dose-response curve is analyzed. The conclusions of the work are drawn in the **Paragraph 3.6**.

### 3.1 Overview

Since several decades, the glyphosate (*N*-(phosphonomethyl)glycine) is the most frequently used nonselective herbicide. It is a powerful inhibitor of 5-enolpyruvylshikimate-3-phosphate synthase (EPSPS), an enzyme involved in the shikimate pathways, which catalyzes the reaction of shikimate-3-phosphate (S3P) and phosphoenolpyruvate to form 5-enolpyruvyl-shikimate-3-phosphate (EPSP), a precursor of aromatic amino acids such as phenylalanine, tyrosine and tryptophan in plants and microorganisms [138–140] and it is an active substance used in Plant Protection Products (PPPs) for plants control [141].

Glyphosate has a high herbicidal activity and relatively low toxicity for humans because the shikimate pathway does not exist in the mammalian genome. However, concern is rising about the possible effects on human health due to the exposure to glyphosate since evidence of increased risk for diseases like non-Hodgkin lymphoma has been highlighted for workers in the agricultural sector compared to other sectors [142]. In fact, several studies have shown that glyphosate can be absorbed in the gastrointestinal tracts of humans and mammals and its effects on mice and rats include gastric diseases, kidneys damage, enlargement of the liver, and inflammation [143–145]. Thus, most of the countries set the upper limits to the presence of glyphosate in drinking water in the range 10-700  $\mu\text{g}\cdot\text{L}^{-1}$ , whereas European Union adopted the stricter level of 0.1  $\mu\text{g}\cdot\text{L}^{-1}$  (for all the pesticides) as being as low as reasonably achievable [146].

The content of glyphosate is usually assessed by means of the standard laboratory procedures like gas chromatography (GC) and liquid chromatography (LC) coupled to various detection systems [147–152]. However, the detection of glyphosate may be difficult due to its high solubility in water and insolubility in organic solvents as well as for the lack of intrinsic chromophore or fluorophore groups in its structure that inhibits the possibility to use photometric and fluorometric detection in LC techniques. Currently, to improve the sensitivity a pre- or post-column derivatization – consisting in the conversion of glyphosate into a sufficiently volatile and thermally stable derivative – is adopted [152–154]. However, these derivatization procedures lead to unstable byproducts, require special equipment and are time-consuming [155,156]. Even alternative approaches to derivatization like high performance liquid chromatography (HPLC) [157], capillary electrophoresis combined with enrichment step [158] or coupled to detecting techniques like indirect laser-induced fluorescence (LIF) [151] or mass spectrometry [152,159] cannot be considered appropriate if quick and simple methods are sought. Electrochemical biosensors are usually based on enzymatic reaction and are promising candidates for rapid detection of glyphosate since they can reach low limit of detections [145,160–163]. Nevertheless, their complexity still prevents them from being used in practical conditions.

Immunosensors can be considered a suitable tool for simple and rapid detection of glyphosate [164], and the colorimetric ones are often preferred for their simple readout. One of the major limitations that affects these biosensors when compared to laboratory biochemical analysis is their relatively poor sensitivity. In an effort to improve the performances of a colorimetric immunosensor, we placed core@shell nanoparticles (magnetic core) in a rotating magnetic field so to realize a self-assembly of nanoparticles in chain-like structures whose rotational dynamics produce a mixing efficiency enhancing. This micromixing increases their diffusion properties in the solution leading to a higher encounter rate among nanoparticles and glyphosate. More specifically,  $\text{Fe}_3\text{O}_4$  nanoparticles (MNPs) are gold coated so to have  $\text{Fe}_3\text{O}_4@Au$  nanoparticles, in which we are able to exploit both (i) the localized surface plasmon resonance (LSPR) of the gold shell and (ii) the magnetic properties of the core ( $\text{Fe}_3\text{O}_4$ ) (Figure 3.1a). Since passive mixing by the simple diffusion takes long time, we introduced an active micromixing method (effective even in a volume as small as 100  $\mu\text{L}$ ) by exposing the solution to a rotating magnetic field [165]. The rotating external magnetic field used to induce “microstirring” was produced through a custom-device (scheme in Figure 3.1b).

Magnetic stirring is considered the most convenient mixing method, thanks to the magnetic fields ability to penetrate non-magnetic or weakly magnetic materials allowing an effective contactless handling [165–168]. In this regard, the use of rotating magnetic fields is already widespread in the literature [165–170]. In particular, the external magnetic field induces the provisional formation of chain-like agglomerates which, under suitable conditions, rotate synchronously with the field [171]. The rotational motion of the structures significantly improves their diffusion within the solution [165].

Although the use of MNPs under an external rotating magnetic field as a fluid mixing strategy has already been verified and confirmed [165,168], so far no other approach has shown that MNPs allow for an efficient colorimetric biosensor. The comparison of the limit of detections (LOD) obtained with the magnetic field off and on shows that in the latter case an improvement of two orders of magnitude emerges, which we explain as the result of a better interaction due to the mixing at the microscale. For futuristic scopes,  $\text{Fe}_3\text{O}_4@Au$  MNPs could also be employed to pre-concentrate or separate analytes in complex matrices.

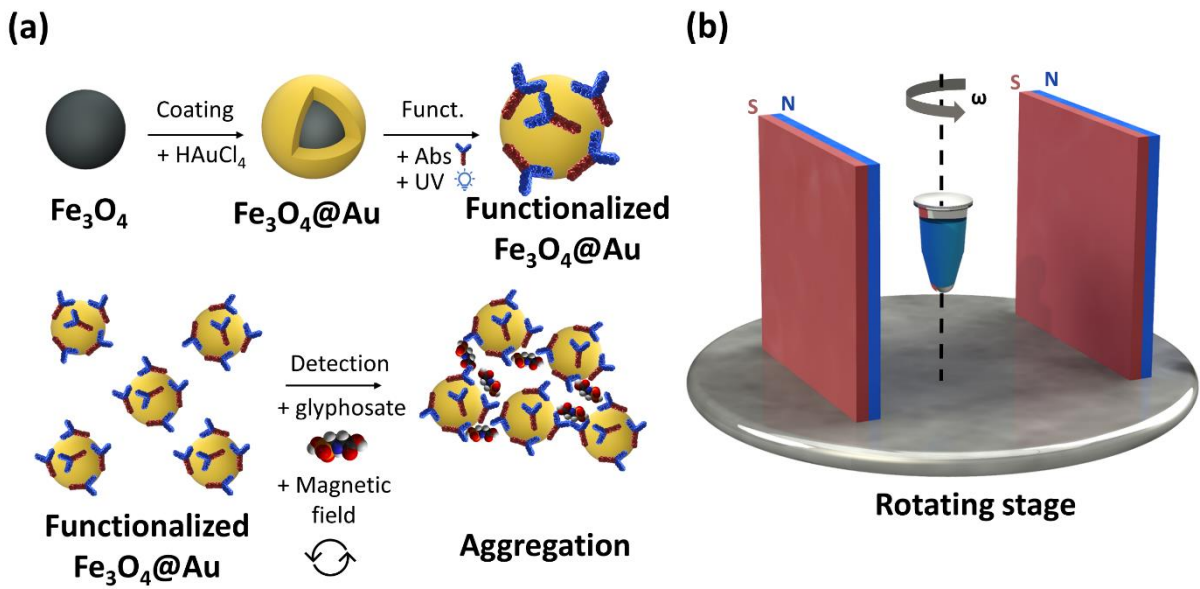


**Figure 3.1.** a) The MNPs are coated with gold and then functionalized with antibodies (IgG-EPSPS) by means of UV light (PIT, Figure 1.4). The glyphosate molecules act as linkers among the nanoparticles causing aggregation. The complexation is facilitated by a rotating external magnetic field that enhances the nanoparticle diffusion. b) Scheme of the wheel used to yield a rotating uniform magnetic field distribution. The wheel rotates at a frequency of approximately five rounds per second. The poles are 4 cm apart (2 cm from the center).

## 3.2 The theory of plasmonic

### 3.2.1 Maxwells' equations

The local surface plasmon resonance (LSPR), originated by the interaction between EM waves and metals, is the phenomenon at the basis of the colorimetric sensor described in this Chapter. The goal of this Paragraph is to briefly outline the theories underlying the phenomena involving the interaction of EM radiation with matter that give rise to the LSPR.

For the purposes of this work, the macroscopic Maxwell's Equations can be considered to describe EM waves within a classical framework:

$$\nabla \cdot \mathbf{D} = \rho_{\text{ext}} \quad 3.1 \qquad \nabla \cdot \mathbf{B} = 0 \quad 3.2$$

$$\nabla \times \mathbf{E} = -\partial_t \mathbf{B} \quad 3.3 \qquad \nabla \times \mathbf{H} = \mathbf{J}_{\text{ext}} + \partial_t \mathbf{D} \quad 3.4$$

Here, the macroscopic fields  $\mathbf{D}$  (dielectric displacement),  $\mathbf{B}$  (magnetic induction),  $\mathbf{E}$  (electric field), and  $\mathbf{H}$  (magnetic field) are driven by the external charge density  $\rho_{\text{ext}}$  and current density  $\mathbf{J}_{\text{ext}}$ . In addition,  $\mathbf{D}$ ,  $\mathbf{B}$ ,  $\mathbf{E}$  and  $\mathbf{H}$  are related to the polarization  $\mathbf{P}$  and the magnetization  $\mathbf{M}$  fields through the following constitutive relations:

$$\mathbf{D} = \varepsilon_0 \mathbf{E} + \mathbf{P} \quad 3.5$$

$$\mathbf{H} = \frac{1}{\mu_0} \mathbf{B} - \mathbf{M}, \quad 3.6$$

where  $\varepsilon_0$  and  $\mu_0$  are the electric permittivity and magnetic permeability of vacuum, respectively.

Metals exhibit different optical behaviour depending on the frequency  $\omega$  of the interacting electromagnetic (EM) field. In the infrared region a negligible fraction of the incident radiation penetrates the bulk and hence the metals can be approximated as perfect conductors showing high reflectance. The EM field propagation through metals becomes prominent in the near infrared and visible regions, resulting in increased dissipation effects, and finally, in the ultraviolet region of the spectrum, the EM perturbations can propagate into the metals with degrees of attenuation that depend on the electronic configuration of the atom. For instance, in noble metals there is a strong absorption of the incident radiation due to the occurrence of interband transitions, whereas alkali metals show an ultraviolet transparency thus their response can be retrieved by considering a free-electron-like model.

Future considerations will be limited to frequency of interacting radiation far from the range of interband transitions, thereby ignoring the fundamental interactions among charged particles, and to nonmagnetic media because electric polarization effects are the most important in order to understand the optical properties of metals.

As a result of the external electric field, the microscopic dipoles inside the medium align, resulting in a macroscopic polarization field described as an electric dipole moment per unit volume. By taking into account the charge conservation  $\nabla \cdot \mathbf{J} = -\partial_t \rho$ , the polarization can be related to the charge density  $\rho_P$  and current density  $\mathbf{J}_P$  by

$$\nabla \cdot \mathbf{P} = -\rho_P \quad 3.7 \quad \mathbf{J}_P = \partial_t \mathbf{P}. \quad 3.8$$

For linear, isotropic, and nonmagnetic ( $\mu = 1$ ) media, the constitutive Equations 3.5 and 3.6 become

$$\mathbf{D} = \varepsilon_0 \varepsilon \mathbf{E} \quad 3.9 \quad \mathbf{B} = \mu_0 \mathbf{H}, \quad 3.10$$

where  $\varepsilon$  is the relative permittivity of the medium. By combining Equations 3.5 and 3.9, it is found that polarization and electric fields are linearly related through the dielectric susceptibility  $\chi$

$$\mathbf{P} = \varepsilon_0 \chi \mathbf{E}. \quad 3.11$$

In the case of ohmic and isotropic metals, the current density is proportional to the electric field by the conductivity  $\sigma$

$$\mathbf{J}_P = \sigma \mathbf{E}. \quad 3.12$$

Equations 3.9 and 3.12 are strictly valid for linear and non-dispersive media.

The non-locality in time and space of metals has to be recovered because of the strong dependence of the optical response on the frequency of the electromagnetic wave impinging on the metal, thus it results [172,173]:

$$\mathbf{D}(\mathbf{r}, t) = \varepsilon_0 \int dt' d\mathbf{r}' \varepsilon(\mathbf{r} - \mathbf{r}', t - t') \mathbf{E}(\mathbf{r}', t'), \quad 3.13$$

$$\mathbf{J}(\mathbf{r}, t) = \int dt' d\mathbf{r}' \sigma(\mathbf{r} - \mathbf{r}', t - t') \mathbf{E}(\mathbf{r}', t'). \quad 3.14$$

In frequency domain, the convolutions 3.13 and 3.14 can be simplify by decomposing the fields into individual plane wave components of wavevector  $\mathbf{k}$  and frequency  $\omega$ .

$$\tilde{\mathbf{D}}(\mathbf{k}, \omega) = \varepsilon_0 \tilde{\varepsilon}(\mathbf{k}, \omega) \tilde{\mathbf{E}}(\mathbf{k}, \omega) \quad 3.15$$

$$\tilde{\mathbf{J}}(\mathbf{k}, \omega) = \tilde{\sigma}(\mathbf{k}, \omega) \tilde{\mathbf{E}}(\mathbf{k}, \omega) \quad 3.16$$

The fundamental relationship between optical dispersion – described by the dielectric function  $\varepsilon$  – and the electric conductivity  $\sigma$  can be obtained by combining the Fourier transform of Equations 3.5 and 3.8 with Equations 3.15 and 3.16. In order to simplify the notation, the symbol  $\sim$  indicating the Fourier transform will be omitted from now on:

$$\varepsilon(\mathbf{k}, \omega) = 1 + \frac{i\sigma(\mathbf{k}, \omega)}{\varepsilon_0 \omega} \quad 3.17$$

Maxwell's Equations 3.3 and 3.4 can be combined to obtain the wave equation describing the propagation of EM field inside the medium in absence of external source ( $\rho_{\text{ext}} = 0$  and  $\mathbf{J}_{\text{ext}} = 0$ ) in the time and frequency domain:

$$\nabla \times \nabla \times \mathbf{E} = -\mu_0 \frac{\partial^2 \mathbf{D}}{\partial t^2}, \quad 3.18$$

$$\mathbf{k}(\mathbf{k} \cdot \mathbf{E}) - k^2 \mathbf{E} = -\varepsilon(\mathbf{k}, \omega) \frac{\omega^2}{c^2} \cdot \mathbf{E} \quad 3.19$$

In Equation 3.19 the constant  $c = 1/\sqrt{\varepsilon_0 \mu_0}$  is the speed of light in vacuum. For transverse waves ( $\mathbf{k} \cdot \mathbf{E} = 0$ ), the Equation 3.19 yields the dispersion relation 3.20, whereas for longitudinal waves, the condition 3.21 defines the frequencies that allow the occurrence of longitudinal collective oscillation [172,173]

$$k^2 = \varepsilon(\mathbf{k}, \omega) \frac{\omega^2}{c^2}, \quad 3.20 \quad \varepsilon(\mathbf{k}, \omega) = 0. \quad 3.21$$

### 3.2.2 Localized Surface Plasmon Resonance (LSPR)

The optical properties of metals can be described by considering a free electron-like system – in which electron-electron interactions and lattice potential are not taken into account – at frequencies far from the interband transitions [172–174]. The oscillations of electrons in such a system are driven by impinging electromagnetic waves and dampened by collisions in the plasma with a characteristic frequency  $\gamma = 1/\tau$ , where  $\tau$  is the relaxation time of the free electron gas. Single electron motion can be described by the following equation in the time domain:

$$m\ddot{\mathbf{x}} + m\gamma\dot{\mathbf{x}} = -e\mathbf{E}. \quad 3.22$$

Where  $m$  and  $e$  are the effective mass and the charge of the conduction electron, respectively. By considering the assumption that the external stimulus has a harmonic time dependence, Equation 3.22 in the frequency domain become

$$\mathbf{x}(\omega) = \frac{e}{m(\omega^2 + i\gamma\omega)} \mathbf{E}(\omega) \quad 3.23$$

The displacement of the electrons gives rise to a macroscopic polarization that can be expressed by the following equation:

$$\mathbf{P}(\omega) = -\frac{ne^2}{m(\omega^2 + i\gamma\omega)} \mathbf{E}(\omega), \quad 3.24$$

where  $n$  is the number density of free electrons. By replacing the Equation 3.24 into the Fourier transform of the constitutive relation 3.5, the dielectric displacement results

$$\mathbf{D}(\omega) = \varepsilon_0 \left( 1 - \frac{\omega_p^2}{\omega^2 + i\gamma\omega} \right) \mathbf{E}(\omega) \quad 3.25$$

$$\omega_p^2 \equiv \frac{ne^2}{\varepsilon_0 m} \quad 3.26$$

where  $\omega_p$  is defined as the plasma frequency of the free electron gas. Therefore, the comparison between Equations 3.9 and 3.25 provides the dispersion relation for a metal in the plasma model approximation.

$$\varepsilon(\omega) = 1 - \frac{\omega_p^2}{\omega^2 + i\gamma\omega} \quad 3.27$$

$$\varepsilon'(\omega) = 1 - \frac{\omega_p^2}{\gamma^2 + \omega^2} \quad 3.28$$

$$\varepsilon''(\omega) = \frac{\omega_p^2\gamma}{\omega(\gamma^2 + \omega^2)} \quad 3.29$$

When metals interact with external perturbations, the coupling between EM field and conduction electrons can lead to the excitation of propagating surface waves called surface plasmon polaritons (SPPs) [173–176]. SPPs are EM waves – produced by the oscillation of conduction electrons – traveling at the conductor/dielectric interface, evanescently confined in the normal direction. The SPP features can be investigated by considering the Maxwell's Equations (from 2.1 to 2.4) in the case of a flat metal/dielectric interface. Although electromagnetic radiation can also interact with the inner part of the metal producing volume plasmons, the latter will not be discussed here since they are not necessary to illustrate the mechanism of operation of the biosensor discussed in this Chapter.

In absence of external stimuli ( $\rho_{\text{ext}} = 0$  and  $\mathbf{J}_{\text{ext}} = 0$ ) and by using the vector identities  $\nabla \times \nabla \times \mathbf{E} \equiv \nabla(\nabla \cdot \mathbf{E}) - \Delta \mathbf{E}$  and  $\nabla \cdot (\varepsilon \mathbf{E}) \equiv \mathbf{E} \cdot \nabla \varepsilon + \varepsilon \nabla \cdot \mathbf{E}$ , the electric wave 3.18 turns into

$$\nabla \left( -\frac{1}{\varepsilon} \mathbf{E} \cdot \nabla \varepsilon \right) - \Delta \mathbf{E} = -\mu_0 \varepsilon_0 \varepsilon \frac{\partial^2 \mathbf{E}}{\partial t^2} \quad 3.30$$

$$\Delta \mathbf{E} - \frac{\varepsilon}{c^2} \frac{\partial^2 \mathbf{E}}{\partial t^2} = 0 \quad 3.31$$

where Equation 3.31 is retrieved by assuming a negligible variation of the dielectric function over distances comparable with the optical wavelength ( $\nabla \varepsilon = 0$ ). In the case of harmonic time dependence of the electric field  $\mathbf{E}(\mathbf{r}, t) = \mathbf{E}(\mathbf{r})e^{-i\omega t}$ , Equation 3.31 becomes the Helmholtz equation [172,173]

$$\Delta \mathbf{E} + k_0^2 \varepsilon \mathbf{E} = 0 \quad 3.32$$

where  $k_0 = \omega/c$  is the wavevector of the propagating wave in vacuum.

The interaction of EM waves with non-extended metal nanoparticles results in stationary (non-propagating) oscillations of the conduction electrons against the positive core of the nanostructure. This stationary surface mode is called localized surface plasmon (LSP) and shows up when the size of the nanoparticles are on the same order of magnitude of the wavelength of the incident radiation [173,176–178]. In particular, while the external electric field induces the oscillation of the conduction electrons, the surface curvature of the nanoparticle exerts a restoring force on the displaced electrons yielding a localized surface plasmon resonance (LSPR) that enhances the field both inside and in the near region outside the particle. A formal solution of the scattering problem is only possible for restricted geometries of nanoparticles and within an electrostatic framework [173,176,179].

### 3.2.3 Mie's and Gans' theories

For spherical nanoparticles, the scattering problem can be conveniently addressed exploiting the symmetries of the system. By introducing the vector spherical harmonics  $\mathbf{M}$  and  $\mathbf{N}$  that satisfy the wave Equation 3.32, Equations 3.33 and 3.34 can be retrieved [177,178,180]:

$$\mathbf{M}_{lm} = \nabla \times (r\psi_{lm}) \quad 3.33 \quad \mathbf{N}_{lm} = \frac{1}{nk} (\nabla \times \mathbf{M}_{lm}) \quad 3.34$$

In this framework the problem simplified to finding the solutions of the scalar wave Equation 3.35 in spherical coordinates:

$$\Delta\psi + k^2\psi = 0. \quad 3.35$$

Equation 3.35 can be solved by separating the wave equation for the three spherical components using the ansatz  $\psi(r, \theta, \varphi) = R(r)S(\theta)T(\varphi)$ . The general solution is given by a linear combination of even and odd generating function [180]:

$$\psi_{lm}^{\text{even}} = \cos(m\varphi) P_l^m(\cos \theta) z_l(kr) \quad 3.36$$

$$\psi_{lm}^{\text{odd}} = \sin(m\varphi) P_l^m(\cos \theta) z_l(kr) \quad 3.37$$

Here,  $P_l^m(\cos \theta)$  are the associated Legendre functions of the first kind of degree  $l$  and order  $m$ , whereas the symbol  $z_l$  is representative of the four spherical Bessel functions  $j_l$ ,  $y_l$ ,  $h_l^{(1)}$ ,  $h_l^{(2)}$ . Equations 3.38 and 3.39 represent two possible solutions of 3.35 [180]:

$$u = e^{-i\omega t} \cos(\varphi) \sum_{l=1}^{\infty} (-i)^l \frac{2l+1}{l(l+1)} P_l^1(\cos \theta) j_l(kr) \quad 3.38$$

$$v = e^{-i\omega t} \sin(\varphi) \sum_{l=1}^{\infty} (-i)^l \frac{2l+1}{l(l+1)} P_l^1(\cos \theta) j_l(kr) \quad 3.39$$

The EM fields satisfying the Maxwell's equations (from 2.1 to 2.4) can be expressed as functions of the particular vector spherical harmonics arisen from the generating functions 3.38 and 3.39 [177,178,180]:

$$\mathbf{E} = \mathbf{M}_v + i\mathbf{N}_u \quad 3.40 \quad \mathbf{H} = n(-\mathbf{M}_u + i\mathbf{N}_v) \quad 3.41$$

The Mie solution inside and outside the sphere can be found by imposing the boundary conditions onto the surface of the sphere and at infinite. Particularly, the field inside the sphere is generated by

$$u = e^{-i\omega t} \cos(\varphi) \sum_{l=1}^{\infty} n c_l (-i)^l \frac{2l+1}{l(l+1)} P_l^1(\cos \theta) j_l(nkr) \quad 3.42$$

$$v = e^{-i\omega t} \sin(\varphi) \sum_{l=1}^{\infty} n d_l (-i)^l \frac{2l+1}{l(l+1)} P_l^1(\cos \theta) j_l(nkr) \quad 3.43$$

while the field outside the sphere results from the superposition of the incident plane wave and the scattered wave

$$u = e^{-i\omega t} \cos(\varphi) \sum_{l=1}^{\infty} a_l (i)^l \frac{2l+1}{l(l+1)} P_l^1(\cos \theta) h_l^{(2)}(kr) \quad 3.44$$

$$v = e^{-i\omega t} \sin(\varphi) \sum_{l=1}^{\infty} b_l (i)^l \frac{2l+1}{l(l+1)} P_l^1(\cos \theta) h_l^{(2)}(kr) \quad 3.45$$

Note that the different spherical Bessel functions  $j_l$  and  $h_l^{(2)}$  appearing in Equations 3.42 and 3.43 than 3.44 and 3.45 is due to the asymptotic behaviour of the finite field at the origin and the scattered wave at infinite, respectively. In an effort to lighten the notation, the Mie coefficients  $a_l$ ,  $b_l$ ,  $c_l$ , and  $d_l$  can be expressed by introducing the Riccati-Bessel functions 3.46 and 3.47:

$$\psi_l(\rho) = \rho j_l(\rho) \quad 3.46 \quad \xi_l(\rho) = \rho h_l^{(1)}(\rho) \quad 3.47$$

Thus, the Mie coefficients in case of nonmagnetic conductive sphere ( $\mu = 1$ ) embedded in a linear, isotropic, and homogeneous medium result [177,178,180]

$$a_l = \frac{m\psi_l(mx)\psi_l'(x) - \psi_l(x)\psi_l'(mx)}{m\psi_l(mx)\xi_l'(x) - \xi_l(x)\psi_l'(mx)} \quad 3.48$$

$$b_l = \frac{\psi_l(mx)\psi_l'(x) - m\psi_l(x)\psi_l'(mx)}{\psi_l(mx)\xi_l'(x) - m\xi_l(x)\psi_l'(mx)} \quad 3.49$$

$$c_l = \frac{m\psi_l(x)\xi_l'(x) - m\xi_l(x)\psi_l'(x)}{\psi_l(mx)\xi_l'(x) - m\xi_l(x)\psi_l'(mx)} \quad 3.50$$

$$d_l = \frac{m\psi_l(x)\xi_l'(x) - m\xi_l(x)\psi_l'(x)}{m\psi_l(mx)\xi_l'(x) - \xi_l(x)\psi_l'(mx)} \quad 3.51$$

where the parameters  $m$  and  $x$  are defined as  $m \equiv \underline{n}_1/n_2$ , in which  $\underline{n}_1$  is the complex refractive index of the metal 3.52 and  $n_2$  is the real refractive index of the surrounding medium, and  $x = k_2 a$ , in which  $k_2 = 2\pi/\lambda_2$  is the wavenumber in the surrounding medium and  $a$  the radius of the particle.

$$\underline{n}(\omega) = \sqrt{\varepsilon(\omega)} \quad 3.52$$

In the case of nanostructures whose dimensions are much smaller than the wavelength of the external EM field, the Mie problem can be addressed by adopting the quasi-static approximation. Since the phase of the oscillating external field is approximately constant over the particle volume, the system acts as a conductive particle in an electrostatic field. Although the quasi-static approximation is strictly valid only for vanishingly small particles, in practice it provides reliable results for nanoparticles whose dimensions are lower than 100 nm [173,176]. For larger particles, the phase of the electric field varies over the particle volume, hence an electrodynamic approach is required.

An analytical solution to the scattering problem is obtained by considering a metal nanosphere of radius  $a \ll \lambda$  – embedded in a linear, isotropic, and homogeneous medium – interacting with an external time-harmonic EM field.

Given the azimuthal symmetry of the system, the general solution of the electrical potential provided by the Laplace equation  $\Delta\Phi = 0$  is [173,176]

$$\Phi(r, \theta) = \sum_{l=0}^{\infty} [A_l r^l + B_l r^{-(l+1)}] P_l(\cos \theta), \quad 3.53$$

where  $P_l(\cos\theta)$  are the Legendre polynomials of order  $l$  and  $\theta$  the angle between  $\mathbf{r}$  and the  $z$ -axis. The expression 3.53 can be written by separating the contribution of the potential inside and outside the sphere.

$$\Phi_{\text{in}}(r, \theta) = \sum_{l=0}^{\infty} A_l r^l P_l(\cos \theta) \quad 3.54$$

$$\Phi_{\text{out}}(r, \theta) = \sum_{l=0}^{\infty} [B_l r^l + C_l r^{-(l+1)}] P_l(\cos \theta) \quad 3.55$$

Note that the coefficient relative to  $r^{-(l+1)}$  in the 3.54 has to be zero to keep finite the potential solution in the center of the sphere. The determination of the coefficients  $A_l$ ,  $B_l$  and  $C_l$  is provided by imposing the boundary conditions at infinite and onto the surface of the sphere. Particularly, at  $r \rightarrow \infty$  the potential results  $\Phi_{\text{out}} \rightarrow -E_0 z = -E_0 r \cos \theta$  following  $B_1 = -E_0$  and  $B_l = 0$  for  $l \neq 1$ , whereas at  $r = a$  the continuity of the tangential component of the electric field and of the normal components of the displacement field demands

$$-\frac{1}{a} \frac{\partial \Phi_{\text{in}}}{\partial \theta} \Big|_{r=a} = -\frac{1}{a} \frac{\partial \Phi_{\text{out}}}{\partial \theta} \Big|_{r=a} \quad 3.56$$

$$-\varepsilon_0 \varepsilon_1 \left. \frac{\partial \Phi_{\text{in}}}{\partial r} \right|_{r=a} = -\varepsilon_0 \varepsilon_2 \left. \frac{\partial \Phi_{\text{out}}}{\partial r} \right|_{r=a} \quad 3.57$$

By inserting the expressions of the potential 3.54 and 3.55 into the relationship 3.56 and 3.57, the remaining nonzero coefficients are

$$A_1 = -\frac{3\varepsilon_2}{\varepsilon_1 + 2\varepsilon_2} E_0 \quad 3.58 \quad C_1 = \frac{\varepsilon_1 - \varepsilon_2}{\varepsilon_1 + 2\varepsilon_2} a^3 E_0 \quad 3.59$$

Therefore, the solutions for potential inside and outside the sphere are

$$\Phi_{\text{in}}(r, \theta) = -\frac{3\varepsilon_2}{\varepsilon_1 + 2\varepsilon_2} E_0 r \cos \theta \quad 3.60$$

$$\Phi_{\text{out}}(r, \theta) = -E_0 r \cos \theta + \frac{\varepsilon_1 - \varepsilon_2}{\varepsilon_1 + 2\varepsilon_2} E_0 a^3 \frac{\cos \theta}{r^2} \quad 3.61$$

The solution 3.61 describes the superposition of the electrostatic field and that produced by an electric dipole located in the center of the sphere. Thus, the potential outside the sphere can be written in terms of the dipole moment  $\mathbf{p}$ .

$$\Phi_{\text{out}} = -E_0 r \cos \theta + \frac{\mathbf{p} \cdot \mathbf{r}}{4\pi\varepsilon_0\varepsilon_2 r^3} \quad 3.62$$

$$\mathbf{p} = 4\pi\varepsilon_0\varepsilon_2 a^3 \frac{\varepsilon_1 - \varepsilon_2}{\varepsilon_1 + 2\varepsilon_2} \mathbf{E}_0 \quad 3.63$$

Such a dipole moment corresponds to that induced inside the metal sphere by the external field  $\mathbf{E}_0$  yielding  $\mathbf{p} = \varepsilon_0\varepsilon_2\alpha\mathbf{E}_0$  of magnitude proportional to polarizability  $\alpha$ .

$$\alpha = 4\pi a^3 \frac{\varepsilon_1 - \varepsilon_2}{\varepsilon_1 + 2\varepsilon_2} \quad 3.64$$

The polarizability 3.64 experiences a resonant enhancement at the minimum of  $|\varepsilon_1 + 2\varepsilon_2|$ . In the case of slow-varying  $\Im\{\varepsilon_1(\omega)\} \equiv \varepsilon_1''$  around the resonance, the minimum is provided by the Fröhlich condition 3.65 and the associated mode is called dipole surface plasmon [173,176]

$$\Re\{\varepsilon_1(\omega)\} \equiv \varepsilon_1' = -2\varepsilon_2. \quad 3.65$$

It is worth to notice that in real cases the magnitude of the polarizability  $\alpha$  in Equation 3.64 is limited by  $\varepsilon_1'' \neq 0$  in the denominator [173,176].

The spatial distribution of the electric field inside and outside the sphere can be retrieved by calculating the gradient of the potentials 3.60 and 3.61 yielding

$$\mathbf{E}_{\text{in}} = \frac{3\varepsilon_2}{\varepsilon_1 + 2\varepsilon_2} \mathbf{E}_0 \quad 3.66$$

$$\mathbf{E}_{\text{out}} = \mathbf{E}_0 + \frac{3\mathbf{n}(\mathbf{n} \cdot \mathbf{p}) - \mathbf{p}}{4\pi\varepsilon_0\varepsilon_2} \frac{1}{r^3} \quad 3.67$$

Note that a resonance in polarizability entails an enhancement of both the internal and dipolar fields. The harmonic time dependence of the electric field  $\mathbf{E}(\mathbf{r}, t) = \mathbf{E}_0 e^{-i\omega t}$  can be recovered in the framework of the quasi-static approximation since the spatial retardation effects are negligible over the whole particle volume for subwavelength nanospheres. Thus, the oscillating electric field induces a coherent dipole moment  $\mathbf{p} = \varepsilon_0\varepsilon_2\alpha\mathbf{E}_0 e^{-i\omega t}$  as shown in Figure 3.2.

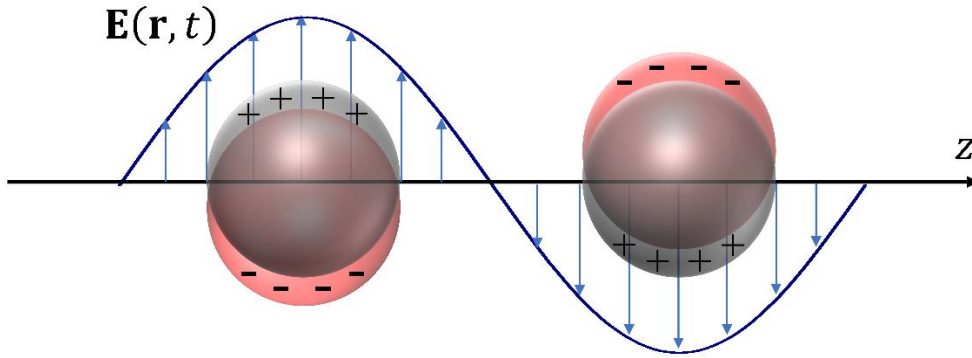


**Figure 3.2.** Excitation of LSPs realized by illuminating the metal nanoparticles with an oscillating electric field. The displacement of the conduction electrons with respect to the positive ion core gives rise to a coherent oscillating dipole moment in the nanoparticles. Reproduced from [25].

In turn, the oscillating dipoles produce an EM field that leads to the scattering of the external radiation. The electric and magnetic fields emitted by an oscillating dipole are [172,173]

$$\mathbf{H} = \frac{ck^2}{4\pi} (\mathbf{n} \times \mathbf{p}) \frac{e^{ikr}}{r} \left(1 - \frac{1}{ikr}\right) \quad 3.68$$

$$\mathbf{E} = \frac{1}{4\pi\varepsilon_0\varepsilon_2} \left\{ k^2 (\mathbf{n} \times \mathbf{p}) \times \mathbf{n} \frac{e^{ikr}}{r} + [3\mathbf{n}(\mathbf{n} \cdot \mathbf{p}) - \mathbf{p}] \left( \frac{1}{r^3} - \frac{ik}{r^2} \right) e^{ikr} \right\} \quad 3.69$$

where  $\mathbf{n}$  is the unit vector in the direction of the point of interest. In the near region ( $kr \ll 1$ ), Equations 3.68 and 3.69 become

$$\mathbf{H} = \frac{i\omega}{4\pi} (\mathbf{n} \times \mathbf{p}) \frac{1}{r^2} \quad 3.70$$

$$\mathbf{E} = \frac{3\mathbf{n}(\mathbf{n} \cdot \mathbf{p}) - \mathbf{p}}{4\pi\varepsilon_0\varepsilon_2} \frac{1}{r^3} \quad 3.71$$

In this zone, the electric field dominates over the magnetic field. Particularly, for static field ( $ka \rightarrow 0$ ), the magnetic field are vanishingly small [172,173]. In the radiative zone ( $kr \gg 1$ ), the fields propagate through spherical-waves of form reading [172,173]

$$\mathbf{H} = \frac{ck^2}{4\pi} (\mathbf{n} \times \mathbf{p}) \frac{e^{ikr}}{r} \quad 3.72$$

$$\mathbf{E} = \sqrt{\frac{\mu_0}{\epsilon_0 \epsilon_2}} \mathbf{H} \times \mathbf{n} \quad 3.73$$

At the resonance frequency both absorption and scattering of the impinging EM radiation occur. In the quasi-static approximation, the scattering and absorption cross sections results [173,176]

$$\sigma_{\text{sca}} = \frac{k^4}{6\pi} |\alpha|^2 = \frac{8\pi}{3} k^4 a^6 \left| \frac{\epsilon_1 - \epsilon_2}{\epsilon_1 + 2\epsilon_2} \right|^2 \quad 3.74$$

$$\sigma_{\text{abs}} = k \Im[\alpha] = 4\pi k a^3 \Im \left[ \frac{\epsilon_1 - \epsilon_2}{\epsilon_1 + 2\epsilon_2} \right] \quad 3.75$$

The assumption of spherical shape can be relaxed to retrieve Equations 3.74 and 3.75 in the case of elongated particles. Gans' theory provides an analytical solution within a quasi-static framework in the case of ellipsoids – with semiaxes  $a_1$ ,  $a_2$  and  $a_3$  much smaller than the excitation wavelength – by decomposing the plasmon excitation along the three symmetry axes [176,179]. In this case, the absorption and scattering cross sections are [176,179]

$$\sigma_{\text{sca},i} = \frac{k^4}{6\pi} |\alpha_i|^4 \quad 3.76 \quad \sigma_{\text{abs},i} = k \Im\{\alpha_i\} \quad 3.77$$

where the subscript  $i = \{1, 2, 3\}$  refers to the direction of the principal axes of the ellipsoid. The polarizabilities  $\alpha_i$  appearing in Equations 3.76 and 3.77 is provided by solving the Laplace equation in ellipsoidal coordinates [176,179]

$$\alpha_i = 4\pi a_1 a_2 a_3 \frac{\epsilon_1 - \epsilon_2}{3\epsilon_2 + 3L_i(\epsilon_1 - \epsilon_2)} \quad 3.78$$

$$L_i = \frac{a_1 a_2 a_3}{2} \int_0^\infty \frac{dq}{(a_i^2 + q)f(q)} \quad 3.79$$

$$f(q) = \sqrt{(q + a_1^2)(q + a_2^2)(q + a_3^2)} \quad 3.80$$

Since the scattering cross section 3.76 scales with the fourth power of the nanoparticle volume while the absorption cross section 3.77 exhibits a linear dependence, the spheroid size introduces a nonlinearity in the extinction cross section  $\sigma_{\text{ext},i} = \sigma_{\text{sca},i} + \sigma_{\text{abs},i}$ .

### 3.2.4 Nanoparticles-based sensor

In colorimetric detection, metal nanoparticles are used to take advantage of the colour change that occurs in colloidal suspension as a result of both changes in refractive index of the surrounding environment and plasmon coupling between the nanoparticles [21–24].

At optical frequencies, LSPR wavelengths are linearly related to changes in refractive index of the surrounding medium over small ranges of  $n$  [22], so refractive index sensitivity of a particular nanoparticle type can be measured in nanometres of peak shift per unit refractive index (nm/RIU):

$$S = \frac{d\lambda_{\text{LSPR}}}{dn}. \quad 3.81$$

By introducing the resonance condition, the refractive index sensitivity can be expressed in terms of resonance wavelength. The latter determines the real part of the dielectric function at resonance  $\varepsilon'(\lambda_{\text{LSPR}})$  for a given particle structure and refractive index  $n$ , and the wavelength dependence on the dielectric function, which determines  $\lambda_{\text{LSPR}}$  given  $\varepsilon'(\lambda_{\text{LSPR}})$  [23]

$$S = \frac{d\varepsilon'(\lambda_{\text{LSPR}})}{dn} \left( \frac{d\varepsilon'(\lambda)}{d\lambda} \right)^{-1}_{\lambda_{\text{LSPR}}}. \quad 3.82$$

Using a Drude-like model, the real part of the dielectric function 3.28 varies nearly linearly with wavelength and can be approximated as follows [23]

$$\varepsilon' = m\lambda + \varepsilon_0, \quad 3.83$$

where  $m \equiv d\varepsilon'(\lambda) \cdot d\lambda^{-1}$  is the slope. By combining Equations 3.83 and 3.84, it results

$$\frac{d\lambda_{\text{LSPR}}}{dn} = \frac{1}{m} \frac{d\varepsilon'(\lambda_{\text{LSPR}})}{dn}. \quad 3.84$$

The polarizability of spheroidal particles with diameter much smaller than the wavelength of light can be approximated by the quasistatic polarizability 3.78. At wavelengths whereby the imaginary part of the dielectric function 3.29 is slowly varying, the resonance occurs at poles of 3.78 yielding

$$\varepsilon'(\lambda_{\text{LSPR}}) = -2\chi n^2 \quad 3.85$$

$$\chi = \frac{1}{2} \left( \frac{1-L}{L} \right) \quad 3.86$$

where  $\chi$  is a shape-dependent parameter related to the depolarization factor  $L$  ( $\chi > 1$  for non-spherical shapes  $\chi = 1$  for a sphere). Thus, the resonance condition determines the sensitivity of the peak wavelength to the refractive index of the medium through its derivative with respect to  $n$ . By inserting Equation 3.85 into 3.84 and considering the linear parametrization 3.83, the refractive index sensitivity of the plasmon peak wavelength results [23]

$$\frac{d\lambda_{\text{LSPR}}}{dn} = \frac{2}{n} \left( \lambda_{\text{LSPR}} + \frac{\varepsilon_0}{m} \right). \quad 3.87$$

Despite larger nanoparticles tend to have higher sensitivities, their peaks are broadened by multipolar excitations and radiative damping [22]. The figure of merit (FOM) can be introduced in order to characterize the nanoparticle sensing capabilities

$$\text{FOM} = \frac{S}{\Delta\lambda}, \quad 3.88$$

where  $\Delta\lambda$  is the resonance line width. For more complex plasmonic nanostructures, it can be difficult to define a consistent LSPR line width, so a more general figure of merit FOM\* can be described in terms of the relative intensity change ( $dI \cdot I^{-1}$ ) that occurs at a fixed wavelength  $\lambda_0$  upon a small change  $dn$  to the local refractive index and does not include the line width [22].

Thus, sensors based on changes in intensity and those based on peak shifts can be directly compared through

$$\frac{d\lambda_{\text{LSPR}}}{dn} = \frac{1}{m} \frac{d\varepsilon'(\lambda_{\text{LSPR}})}{dn}. \quad 3.89$$

Due to the LSPR shift, caused by the environmental change, nanoparticles may also be used in bulk refractive index sensors as well as molecular sensors. In the latter case, the change to the particle dielectric environment is confined to a nanoscale volume around the nanoparticle due to the rapidly decay of LSPR with the distance from the surface [181–183]. In case of molecular sensing, the figure of merit  $\text{FOM}_{\text{mol}}$  is defined as the maximum number of bound molecules on the nanoparticles (or dynamic range, DR) divided by the minimum number of detectable molecules (or molecular detection limit, MDL). The MDL is calculated as [22]

$$\text{MDL} = \frac{V_S \sqrt{U_{\text{system}}^2 + U_{\text{fit}}^2}}{V_A \Delta \text{RI} e^{-2r/l_d} 3S_0} \quad 3.90$$

where  $V_S$  is the sensing volume,  $V_A$  is the analyte volume,  $\Delta RI$  is the refractive index difference between the analyte and the surrounding medium,  $U_{\text{system}}$  is the uncertainty in the physical detection of the LSPR peak,  $U_{\text{fit}}$  is the uncertainty in the fitting of the LSPR peak,  $S_0$  is the bulk refractive index sensitivity,  $r$  is the distance of the analyte from the nanoparticle surface, and  $l_d$  is the decay length of the electric field from the particle surface.

The analyte detection in label-based colorimetric approaches can be achieved by cross-linking, non-cross-linking, or destabilization-induced aggregation [25,72]. In this work we exploited a cross-linking method in which the nanoparticles aggregation is induced by the controlled assembly of ligand-functionalized AuNPs through intermolecular bonds between ligands and analytes, which overpower the interparticle electrostatic repulsion (Figure 3.3). In such a case (Figure 3.3b), the analytes can act as both linkers among ligand-functionalized AuNPs inducing their aggregation and anchoring sites wherein the LSPR shift arises from the close-packing of ligand-functionalized AuNPs around the analyte Figure 3.3c.

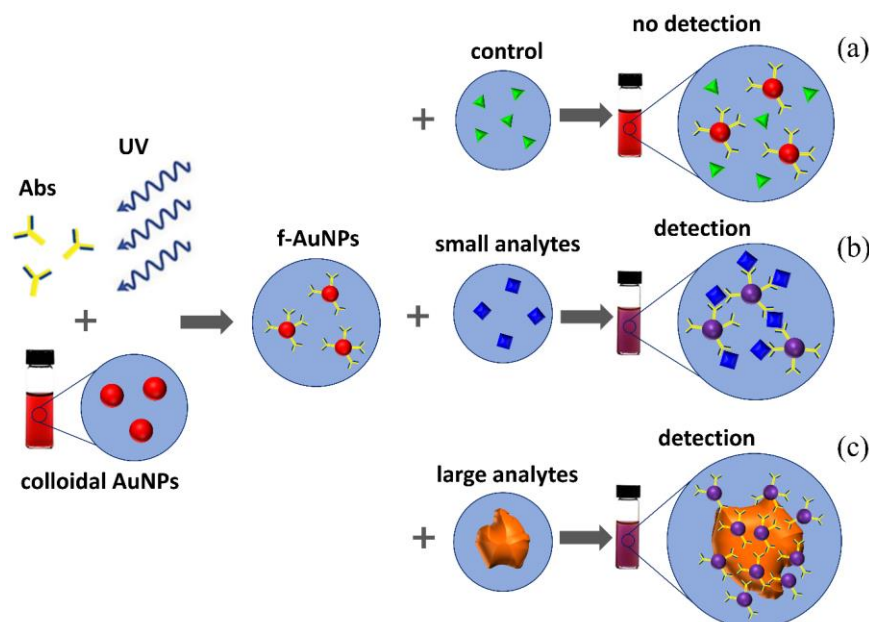


**Figure 3.3.** Detection scheme of a colorimetric immunosensor based on a colloidal solution of PIT-functionalized AuNPs with Abs (f-AuNPs). (a) No optical change is measured if the analytes are not recognised by f-AuNPs. (b) Small analytes act as linkers due to multiple binding sites allowing the f-AuNPs to aggregate. (c) Large analytes are surrounded by f-AuNPs promoting their plasmon coupling. Reproduced from [25].

Although cross-linking aggregation method offers a convenient colorimetric assay, its sensitivity is usually limited to the nanomolar levels due to the lack of feasible amplification steps while its dynamic range spans only few decades of the analyte concentration due to the occurrence of the hook effect – i.e. the saturation of ligand binding sites that prevents the AuNP aggregation at higher analyte concentrations [22,184].

In such a case, the analytes can act as both linkers among ligand-functionalized AuNPs inducing their aggregation (Figure 3.3b) and anchoring sites wherein the LSPR shift arises from the close-packing of ligand-functionalized AuNPs around the analyte (Figure 3.3c).

## 3.3 Materials and methods

### 3.3.1 Materials

Iron oxide (II, III) MNPs (average diameter 30 nm) were purchased by MERCK (catalog number 747327), gold (III) chloride hydrate and sodium citrate were purchased from Sigma-Aldrich. The IgG-EPSPS antibody used for Fe<sub>3</sub>O<sub>4</sub>@Au MNPs functionalization and the glyphosate were purchased from Thermo-Fischer. Bovine serum albumin (BSA) for blocking the surface of Fe<sub>3</sub>O<sub>4</sub>@Au and the aminomethylphosphonic acid (AMPA) [0.25 µg·mL<sup>-1</sup>], a common metabolite of glyphosate, used to test the specificity of the biosensor, were both purchased from Sigma Aldrich.

The biofunctionalization of Fe<sub>3</sub>O<sub>4</sub>@Au MNPs was carried out by means of the photochemical immobilization technique (PIT) [65] already shown to be very effective for similar colorimetric biosensors [27,72]. In this experiment, the UV radiation at  $\lambda=254$  nm was produced by two U-shaped low-pressure mercury lamps (Trylight®, Promete s.r.l.) in which a standard quartz cuvette could be easily housed (Figure 1.4). Since each of the lamp could deliver 6 W, given the proximity of the cuvette to the lamps and the wrapping geometry, we estimated that the solution was exposed to an UV-irradiation of approximately 0.3 W·cm<sup>2</sup>.

Spectrophotometric measurements were performed with a 6715 UV-Vis spectrophotometer (Jenway), while transmission electron microscopy (TEM) images for morphological analysis of the produced NPs were obtained with the FEI Tecnai G2 20 Transmission Electron Microscope.

The permanent neodymium iron boron magnets used to realize a rotating magnetic field were purchased from Alga Magneti s.r.l. (Italy).

### 3.3.2 Synthesis of Fe<sub>3</sub>O<sub>4</sub>@Au MNPs

The solution containing Fe<sub>3</sub>O<sub>4</sub> NPs exhibits the brownish color observable in Figure 3.4a.

The coating of the MNPs is a crucial step to prevent core oxidation, ensure functionalization and observe the phenomenon of LSPR. To this end, we adopted the direct gold coating [20,185] by adding 3 mL sodium citrate [10 mg·mL<sup>-1</sup>] and 225 µL Fe<sub>3</sub>O<sub>4</sub> NPs [5 mg·mL<sup>-1</sup>] into 45 mL of ultra-pure water. The whole solution was heated up to 95 °C under gentle stirring. When the solution was close to the

boiling point, 50  $\mu\text{L}$  of  $\text{HAuCl}_4$  [ $10 \text{ mg}\cdot\text{mL}^{-1}$ ] were added for three times every 2 minutes. After one hour, the color changed from brownish to red-violet as a consequence of the Au shell formation (Figure 3.4b). To separate the gold-coated MNPs ( $\text{Fe}_3\text{O}_4@ \text{Au}$  MNPs) from the gold NPs, both present at the end of the synthesis, the solution was centrifuged by a Heraeus Pico 17 centrifuge at 6000 rpm for 30 minutes. To maximize the efficiency of the  $\text{Fe}_3\text{O}_4@ \text{Au}$  MNPs separation from the gold NPs, an external magnetic field was applied using a neodymium iron boron magnet.

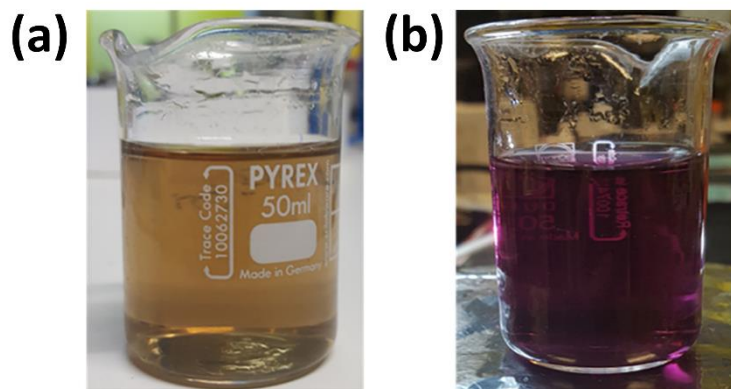


**Figure 3.4.** a) Solution of pristine magnetic nanoparticles ( $5 \text{ mg}\cdot\text{mL}^{-1}$ ) before coating. b) The same solution after gold coating ( $\text{Fe}_3\text{O}_4@ \text{Au}$  MNPs).

### 3.3.3 Functionalization of $\text{Fe}_3\text{O}_4@ \text{Au}$ MNPs

A volume of 100  $\mu\text{L}$  of UV-activated EPS-PS-IgG ( $25 \text{ }\mu\text{g}\cdot\text{mL}^{-1}$ ) was mixed to 1 mL of  $\text{Fe}_3\text{O}_4@ \text{Au}$  MNPs ( $5 \text{ mg}\cdot\text{mL}^{-1}$ ) to functionalize the nanoparticles [65]. The mixing was realized by adding small volumes (5  $\mu\text{L}$ ) of antibody solution every 5 seconds so that the whole process was accomplished in 100 seconds. The process took place keeping the  $\text{Fe}_3\text{O}_4@ \text{Au}$  MNPs solution under gentle stirring to avoid non controlled aggregation. The number of spikes – and, hence, the amount of IgGs to be mixed to the solution of  $\text{Fe}_3\text{O}_4@ \text{Au}$  MNPs – was chosen so to saturate the surface coverage. To this end, we measured the wavelength shift after each spike with freshly UV-irradiated solution. As Figure 3.5a shows, 20 spikes were enough to reach the saturation of the process. The effective surface coverage was further demonstrated by the blocking realized by adding 200  $\mu\text{L}$  of Bovine Serum Albumin (BSA) [ $50 \text{ }\mu\text{g}\cdot\text{mL}^{-1}$ ]. In this case, no additional wavelength shift was detected (see Figure 3.5b) after the blocking step, a result that is expected when the surface is fully covered and no room is available for BSA. After the blocking phase the  $\text{Fe}_3\text{O}_4@ \text{Au}$  MNPs solution was centrifuged again at 6000 rpm for 30 minutes to remove the Abs and the BSA in excess and 50  $\mu\text{L}$  of ultrapure water were gently added to the microtube containing the pellet of MNPs.

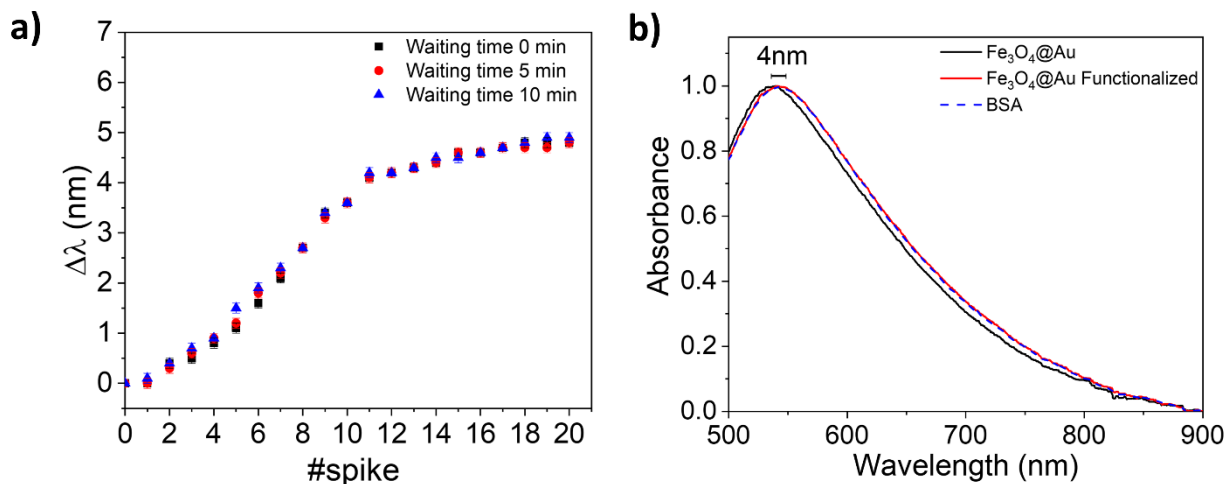


**Figure 3.5.** a) Wavelength shifts ( $\Delta\lambda$ ) in response to the number of spikes of Ab. Each spike was 5  $\mu\text{L}$  and did not significantly change the volume of the colloidal solution (1 mL). The concentration of the Ab solution was 25  $\mu\text{g}\cdot\text{mL}^{-1}$ . The shift is measured after a waiting time. The waiting times of 0 min corresponds to measurements carried out immediately after the spike. The saturation value is reached after approximately 10 spikes and it was the value adopted throughout the experiment. The lack of dependence on the waiting time suggests that the antibodies quickly bind the nanoparticles. b) Absorption spectra of Fe<sub>3</sub>O<sub>4</sub>@Au MNPs before (black line) and after (red) functionalization. After the functionalization, there is a red shift of approximately 4 nm as a consequence of the increase of the refractive index caused by the antibody surrounding the surface. The dashed blue curve is the absorption spectrum after the blocking carried out by BSA. The lack of any shift demonstrate that the surface was well covered by Abs.

### 3.3.4 Rotating magnetic field

The rotating magnetic field was realized using a rotating wheel on which two magnets were stuck according to the geometry reported in Figure 3.1b. Such a configuration was the result of empirical attempts aimed at realizing in the central region an intense magnetic field so to favor the formation of chain-like Fe<sub>3</sub>O<sub>4</sub>@Au agglomerates whose rotational dynamics produce a mixing efficiency enhancing their diffusion. In fact, by rotating the wheel by means of a DC motor, we could find that a frequency of approximately 5 Hz was effective in whirling the colloidal solution, while for frequencies higher than 10 Hz the mixing was less effective. The magnetic field in the region between the magnets was measured using hall probes. In the central region, which is a center of symmetry for the configuration, the magnetic field was about 100 mT.

## 3.4 Results

### 3.4.1 Characterization of Fe<sub>3</sub>O<sub>4</sub>@Au MNPs

A representative TEM image of the iron oxide MNPs is shown in Figure 3.6a, which confirms the spherical shape of the nanoparticles with an average diameter of 30 nm. Figure 3.6b shows the TEM image of the nanoparticles after the coating procedure. The results of the protocol were Fe<sub>3</sub>O<sub>4</sub>@Au

MNPs with an average diameter of 50 nm. As a consequence of the coating process, were produced irregular-shaped spurious gold nanoparticles too, that were eliminated in the magnetic separation process after the centrifugation step Paragraph 3.3.2.

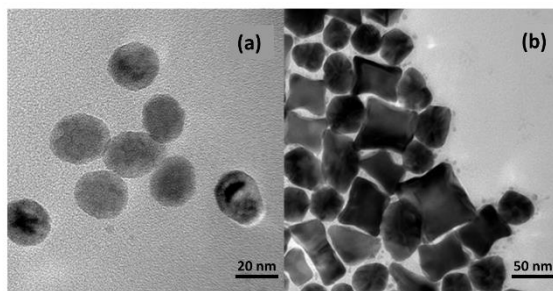


**Figure 3.6.** TEM images showing size and morphology of nanoparticles. a)  $\text{Fe}_3\text{O}_4$  MNPs and b)  $\text{Fe}_3\text{O}_4@Au$  MNPs.

The absorbance spectrum of  $\text{Fe}_3\text{O}_4@Au$  MNPs is shown in Figure 3.7 (black solid line). The resonance peak at 530 nm confirms the presence of gold on the surface of the MNPs. In order to assess the thickness of the gold layer, we simulated the optical response of an aqueous solution containing core@shell nanoparticles by finite-difference time-domain (FDTD) method which we used to solve Maxwell's equations [186–188]. A detailed description of the simulation workspace is reported in Figure 3.8, whereas Figure 3.7 shows the normalized absorbance of  $\text{Fe}_3\text{O}_4@Au$  MNPs as a function of the shell thickness. As expected, the LSPR wavelength red-shifts as the shell thickness increases. A shell thickness of 10 nm (red solid line) satisfactorily reproduces the experimental data (black solid line) thereby corroborating the nanoparticle enlargement observed by TEM images (Figure 3.6).

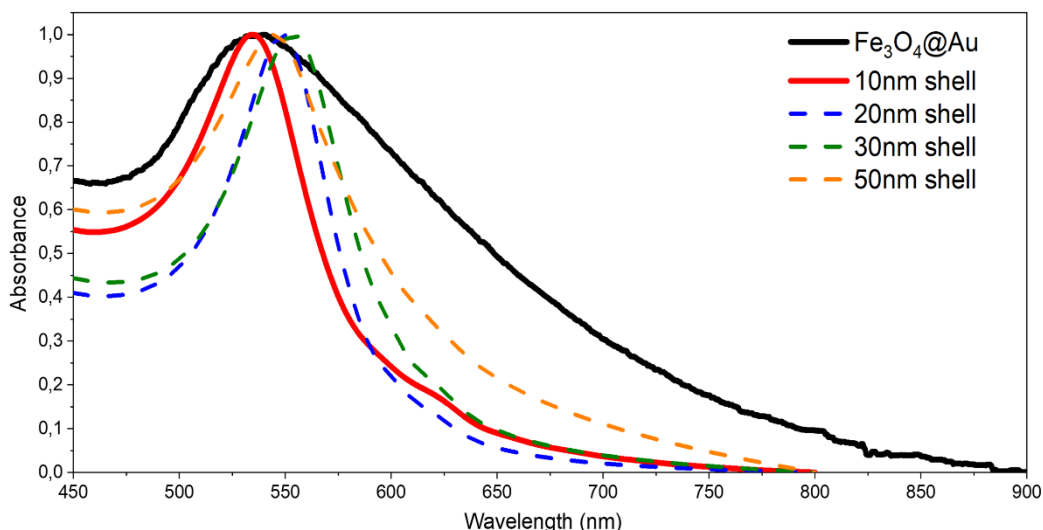


**Figure 3.7.** Comparison between experimental absorption spectrum (black solid line) and simulated normalized spectra obtained for different thicknesses of the gold shell. The simulated data resulting from a shell thickness of 10 nm are the ones who best reproduce the experimental spectrum.

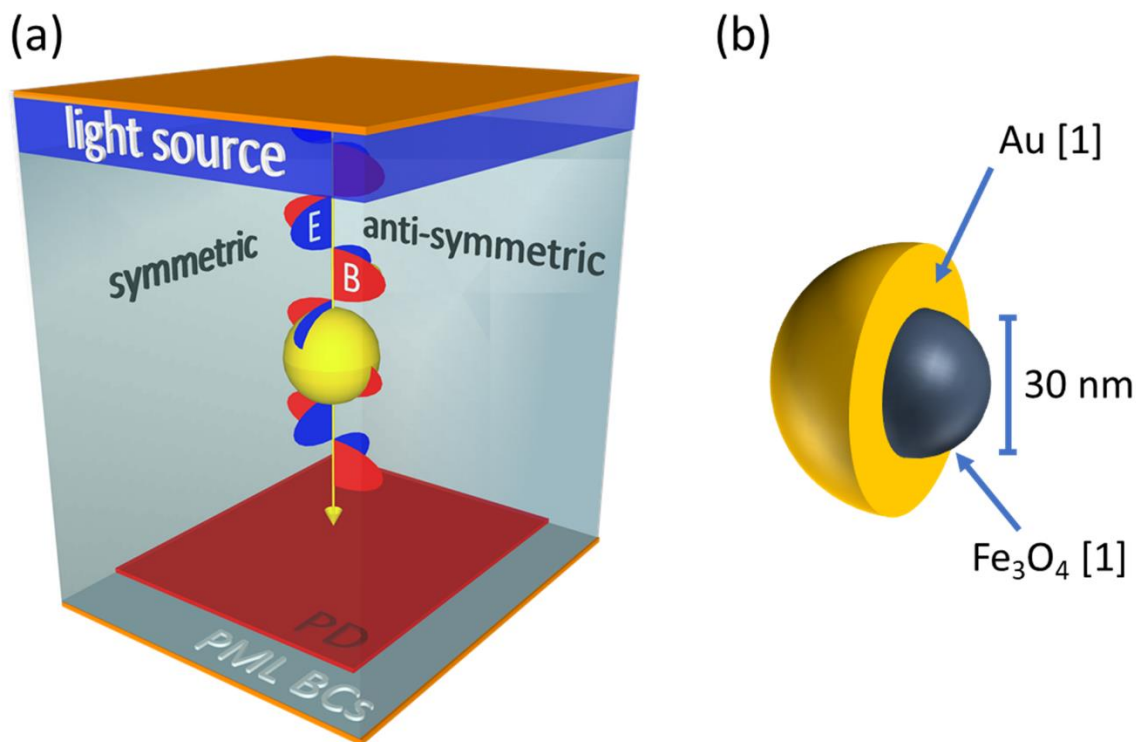


**Figure 3.8.** (a) Schematic representation of the simulation workspace in Lumerical's environment consisting of light source, boundary conditions (BCs), photodetector (PD), nanostructure and embedding medium. A  $x$ -polarized electromagnetic wave propagating along  $z$  direction was used to investigate the optical response of the core@shell nanoparticle. The refractive index of the embedding medium was set 1.33. A photodetector was placed on the opposite side of the workspace to collect the transmittance photons. Anti-symmetric/symmetric BCs were set in both  $x$ - and  $y$ -directions to reduce the simulation time by a factor of 8 without worsening the accuracy of the results. Perfect matched layer (PML) BCs were set in  $z$  direction to warrant perfect absorption of the radiation both propagating beyond the photodetector and backscattered through the light source. The simulation volume was discretized over a mesh of 0.3 nm spatial resolution in order to obtain a high accuracy level while keeping the simulation time within few hours. (b) Sketch of the core@shell nanoparticle made of 30 nm diameter  $\text{Fe}_3\text{O}_4$  [2] core and gold [1] shell with variable thickness in the range 10-30 nm.

### 3.4.2 Detection of glyphosate

An aqueous solution (tap water) of 50  $\mu\text{L}$  containing glyphosate at different concentrations was added to the microtube containing 50  $\mu\text{L}$  of ultrapure water and the pellet of functionalized  $\text{Fe}_3\text{O}_4$ @Au MNPs (Paragraph 3.3.3) for the detection (1:1 volume). One of the limiting factors in a colorimetric biosensor based on the aggregation induced by the presence of the target analyte is the relatively low diffusion velocity of the nanoparticles. In fact, the large mass of the nanoparticles hampers the aggregation thereby limiting the sensitivity. To overcome such an issue, we exposed the microtube to the rotating magnetic field yielded by the wheel sketched in Figure 3.1b. The whirlpools induced by the stirring at approximately 5 Hz were visible by eye in the volume of 100  $\mu\text{L}$ . Subsequently, absorbance measurements were performed after transferring the solution into a cuvette. The optical density of the colloidal solution was 1, corresponding to approximately  $10^{10}$  nanoparticles $\cdot\text{mL}^{-1}$ .

To highlight the contribution of the magnetic field to the aggregation, we carried out the experiment with the same solution of nanoparticles ( $\text{Fe}_3\text{O}_4@Au$  MNPs) without the magnetic stirring. The dose-response curves are reported in Figure 3.9, in which the left [(a) and (c)] and right [(b) and (d)] panels refer to the experiment with the rotating magnetic field turned off and on, respectively. More specifically, Figure 3.9a and b shows the resonance shift of the localized surface plasmon resonance ( $\Delta\lambda_{\text{LSPR}}$ ) due to specific target recognition without and with the magnetic stirring, respectively. The shifts were measured from the absorption spectra reported in Figure 3.10. The lower panels (Figure 3.9c and d) show the pictures of the cuvettes resulting from the detection of glyphosate at different concentrations. The color change is visible by naked eyes.

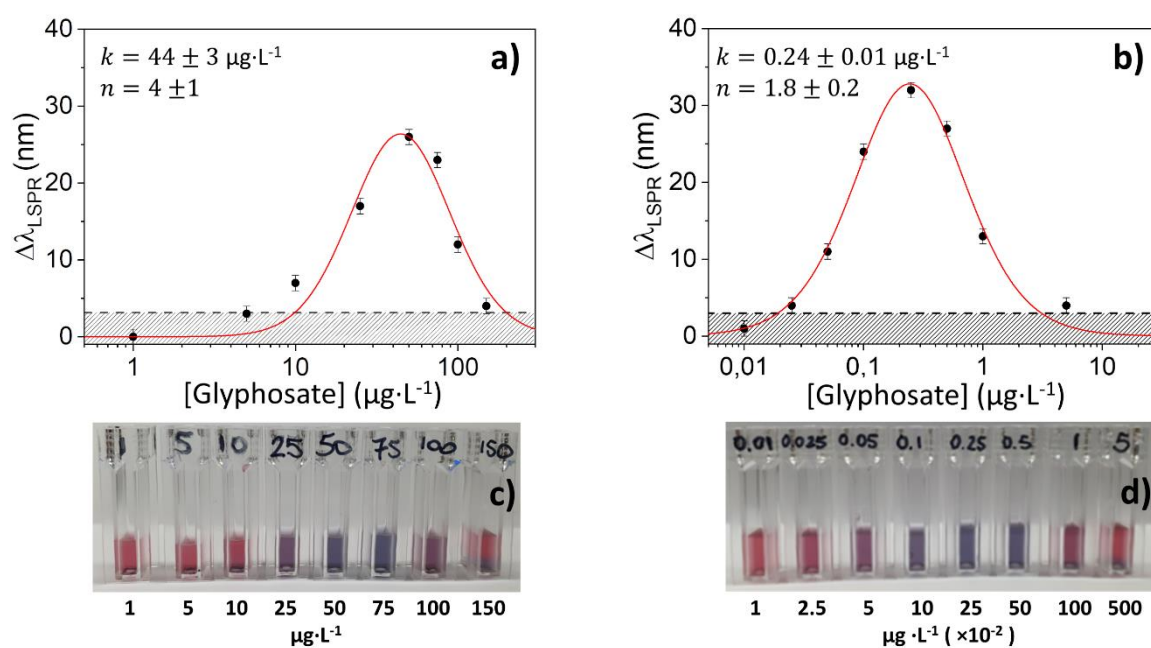


**Figure 3.9.** Resonance shift observed by mixing 50  $\mu\text{L}$  of an aqueous solution (tap water) containing glyphosate at different concentrations to 50  $\mu\text{L}$  of  $\text{Fe}_3\text{O}_4@Au$  MNPs. The rotating magnetic field was either turned (a) off or (b) on. The dose response curve is the best fit of the experimental data obtained with Equation (1). The gray regions represent the 3 standard deviations (SD) noise level and set the limit of detection to (a) 10  $\mu\text{g}\cdot\text{L}^{-1}$  and (b) 20  $\text{ng}\cdot\text{mL}^{-1}$  for magnetic field off and on, respectively. The 100  $\mu\text{L}$  volume resulting from the mixing was diluted in pure water (1:10) so to have 1 mL volume suitable for the spectrophotometers (see spectra reported in Figure 3.10). Panels (c) and (d) the pictures of the cuvettes resulting from the detection of glyphosate at different concentrations.

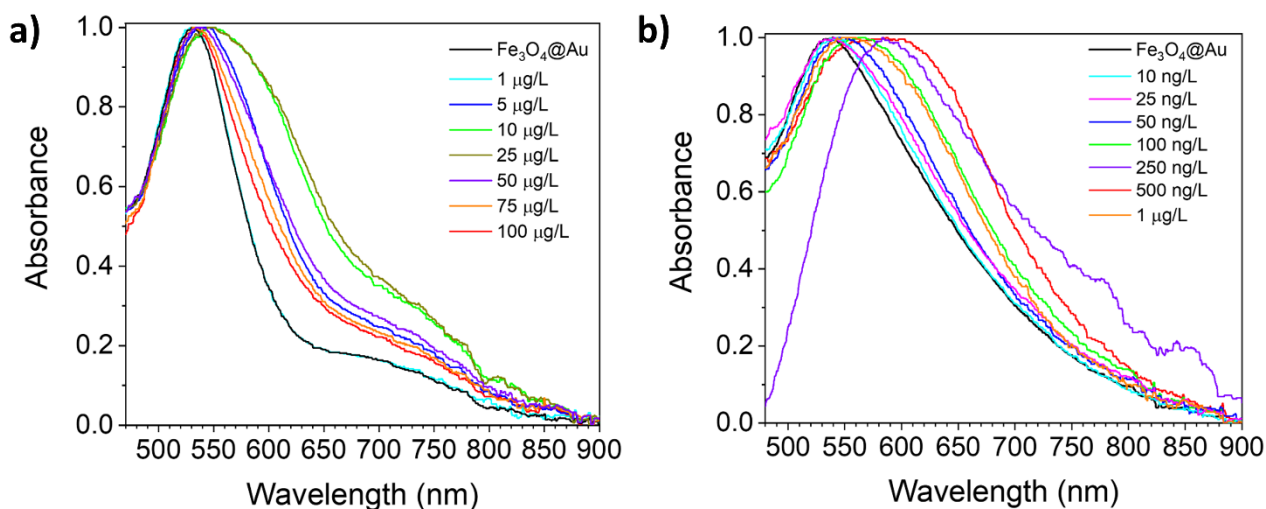


**Figure 3.10.** Absorption spectra  $\text{Fe}_3\text{O}_4\text{@Au}$  MNPs at several glyphosate concentrations. The magnetic field was either (a) off or (b) on.

### 3.4.3 Specificity assay against AMPA

As expected for an immunosensor like the one described in this work, the specificity was very high as witnessed by the lack of any change in the absorption spectrum observed when aminomethylphosphonic acid (AMPA) was tested (Figure 3.11). The main glyphosate metabolite [158], was mixed at the several concentrations in the range  $0.01\text{-}100\ \mu\text{g}\cdot\text{L}^{-1}$ , the choice to investigate the specificity in a wide window of concentrations values was dictated by the need to avoid any influence of the Hook effect in the lack of the color change.

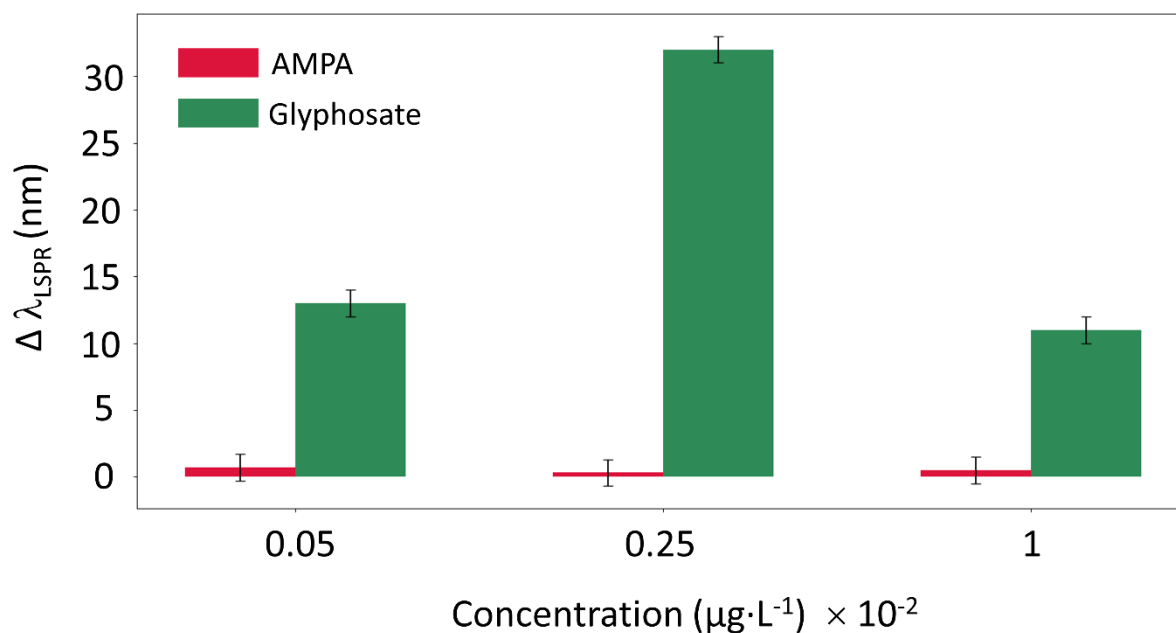


**Figure 3.11.** Sensor specificity. The sensor responds to aminomethylphosphonic acid (AMPA), the main glyphosate metabolite. As can be noticed the signal obtained with AMPA is compatible with zero and departs to what is obtained for glyphosate. The specificity assays was carried out at several concentrations in the range  $0.01\text{-}100\ \mu\text{g}\cdot\text{L}^{-1}$  ( $0.05, 0.25, 1\ \mu\text{g}\cdot\text{L}^{-1}$

<sup>1</sup> reported), in order to avoid any influence of the Hook effect in the lack of the signal change. The experimental procedure was the same employed for the detection of glyphosate as well as the statistical data analysis to determine the errors.

## 3.5 Discussion

### 3.5.1 Dose-response curve

By considering a simplified description of the aggregation dynamics [27,28], it is possible to relate  $\Delta\lambda_{LSPR}([G])$  to the glyphosate concentration  $[G]$  through the following equation

$$\Delta\lambda_{LSPR}([G]) = \left( \frac{R \cdot [G]}{(k + [G])^2} \right)^n \quad 3.91$$

In Equation 3.91 the factor  $R$  includes both the  $\text{Fe}_3\text{O}_4@Au$  MNPs concentration and instrument response,  $k$  is the concentration at which the signal is maximum and  $n$  arises from the multiple order complexation between the two interacting species (glyphosate and functionalized  $\text{Fe}_3\text{O}_4@Au$  MNPs) and can be related to the Hill coefficient [189]. The red lines in Figure 3.9a and b are the best fits of the experimental data to Equation 3.91 with the resulting values for  $k$  and  $n$  shown in the panels, whereas we got  $R = (39 \pm 6) \times 10 \text{ (nm)}^{\frac{1}{n}} \cdot \mu\text{g} \cdot \text{L}^{-1}$  and  $R = 6.6 \pm 0.6 \text{ (nm)}^{\frac{1}{n}} \cdot \mu\text{g} \cdot \text{L}^{-1}$ , for the data in 5a and 5b, respectively. From Figure 3.9a and b, we see that when the magnetic field is turned on, the value for  $k$  reduces by a factor of 100 compared to the one achieved in case of field turned off, whereas the complexity order  $n$  is essentially the same in both cases. The reduction of  $k$  is the direct consequence of the increase in the interaction rate between glyphosate and nanoparticles entailed by the micromixing. In this respect,  $k$  takes into account the mixing of microscopic entities that can take place with different kinetics and, hence, can give rise to different equilibrium constants. On the contrary, the similarity of the values obtained for the complexity order  $n$  possibly confirms that such a parameter is mainly related to the microscopic features such as the number of antibodies per nanoparticles, the antibody affinity or even the nanoparticle size.

By adopting the 3 standard deviations (SD) criteria (see Figures 5a and 5b), we obtained a LOD in the detection of glyphosate of  $10 \mu\text{g} \cdot \text{L}^{-1}$  using  $\text{Fe}_3\text{O}_4@Au$  MNPs with the rotating magnetic field turned off, whereas the LOD lowered down to  $20 \text{ ng} \cdot \text{L}^{-1}$  when the rotating magnetic field was turned on. Thus, the micromixing step improved the recognition of the antigens that in turn lowered the LOD by more than two order of magnitude. The features of our immunosensor are compared to those of other techniques in Table 3.1.

**Table 3.1.** Features of several biosensors and laboratory techniques for detecting glyphosate.

| Separation technique | Detection method | Sample                | Derivatization | Pre-concentration | Detection limit         | Ref.      |
|----------------------|------------------|-----------------------|----------------|-------------------|-------------------------|-----------|
| CE                   | C                | water                 | -              | yes               | 85 µg·L <sup>-1</sup>   | [158]     |
|                      | Indirect LIF     | commercial herbicides | -              | -                 | 200 µg·L <sup>-1</sup>  | [151]     |
|                      | MS               | wheat                 | -              | -                 | 420 µg·L <sup>-1</sup>  | [159]     |
| HPLC                 | UV-Vis           | fruit juices          | yes            | yes               | 10 µg·L <sup>-1</sup>   | [190]     |
|                      | F                | rainwater             | yes            | -                 | 0.16 µg·L <sup>-1</sup> | [191]     |
|                      |                  | water                 | yes            | yes               | 0.02 µg·L <sup>-1</sup> | [147]     |
|                      | C                | water                 | -              | yes               | 42 µg·L <sup>-1</sup>   | [192]     |
|                      | ICP-MS           | water                 | -              | -                 | 0.7 µg·L <sup>-1</sup>  | [152]     |
|                      | EC               | water                 | yes            | -                 | 1.7 µg·L <sup>-1</sup>  | [193]     |
|                      | EC               | water                 | -              | -                 | 8.6 ng·L <sup>-1</sup>  | [194]     |
|                      | CD               | fruit juices          | -              | -                 | 100 µg·L <sup>-1</sup>  | [156]     |
|                      | CV biosensor     | water                 | -              | -                 | 5 ng·L <sup>-1</sup>    | [195]     |
| -                    | Colorimetric     | water                 | -              | -                 | 20 ng·L <sup>-1</sup>   | this work |

CE= Capillary Electrophoresis; C= Conductivity; LIF= Laser Induced Fluorescence; CD= Coulometric Detection; MS= Mass Spectrometry; ICP-MS = Inductively Coupled Plasma-Mass Spectrometry, CV = Cyclic Voltammetry.

### 3.5.2 Micromixing modelling

When a solution of magnetic nanoparticles (MNPs) is exposed to a magnetic field, the dipole-dipole interaction between the induced magnetic moments of the particles may induce the formation of chains along the direction of the magnetic field (Figure 3.13b). The chains formation process is realized as a balance between the field-induced attractive particle-particle magnetic interaction and the thermal energy. In this scenario the energy decrease associated to the magnetic coupling drives the formation of chains while the loss of entropy characterized by a solution with ordered structure of different sizes plays the opposite role. The critical value for this phenomenon that determines the balance between energetic and entropic factors is the so-called aggregation parameter  $N^*$ , which can be considered an estimation of the mean number of MNPs in a chain [196].

The magnetic chains can rotate at a constant frequency if the magnetic torque is balanced by the viscous torque. The magnetic torque ( $\Gamma_m$ ) acting on a chain of  $N^*$  spherical magnetic particles is given by equation [165,197]:

$$\Gamma_m = \frac{3\mu^2 N^{*2}}{64\pi\mu_0 r_0^3} \sin(2\alpha). \quad 3.92$$

In equation 3.92  $\mu$  is the dipole moment induced by the external magnetic field ( $\mu = \frac{4}{3}\pi r_0^3 \mu_0 \chi H_0$ , Figure 2.14), where,  $r_0$  ( $15 \cdot 10^{-9}$  m) is the radius of the magnetic core,  $\mu_0$  ( $4\pi \cdot 10^{-7}$  H·m<sup>-1</sup>) is the vacuum permeability,  $\chi$  is the magnetic susceptibility,  $H_0$  (100 mT) is the magnitude of the magnetic field applied and  $\alpha$  is the angle between the applied magnetic field and the longitudinal direction of the chain.

The viscous torque ( $\Gamma_v$ ) for a chain of  $N^*$  spherical particles rotating in a medium of viscosity  $\eta$  with angular velocity  $\omega$  is given by [198]:

$$\Gamma_v = kV\eta\omega, \quad 3.93$$

where  $k = \frac{2N^{*2}}{\ln(\frac{N^*}{2})}$  is a shape factor,  $V = N^* \frac{4\pi(r_0+r_c)^3}{3}$  is the volume of the chain,  $r_c$  ( $10 \cdot 10^{-9}$  m) is the thickness of the gold shell and in our case  $\eta$  is the viscosity of water ( $8.9 \cdot 10^{-4}$  Pa·s).

The balance between the two opposing torques leads to the existence of a maximum rotation frequency ( $f_{\max}$ ) for synchronous rotation, that is obtained equating the maximum magnetic torque (obtained for  $\alpha = \frac{\pi}{4}$ ) to the viscous torque:

$$f_{\max} = \frac{\mu_0 \chi^2 H_0^2 \ln\left(\frac{N^*}{2}\right)}{64\pi\eta N^*} \left(\frac{r_0}{r_0 + r_c}\right)^3. \quad 3.94$$

For frequencies lower than  $f_{\max}$ , the structure of the chain remains intact and rotates synchronously with the field (Figure 3.12b), whereas for frequencies above  $f_{\max}$  the chain rotate asynchronously and its structure can be compromised with the result that the mixing is not optimal (Figure 3.12d) [171]. In our case, the value for  $f_{\max}$  was determined experimentally by applying the rotating magnetic field to the solution containing the MNPs pellet and the glyphosate (Figure 3.13a). The  $f_{\max}$  value obtained was equal to 10 Hz, and it was used in Equation 3.94 to estimate  $N^*$ , obtaining  $N^* \approx 1.5 \cdot 10^4$  MNPs in a chain. The formation of rotating chains significantly accelerates the diffusion dynamics of the nanostructures in solution and is responsible for the improvement in terms of LOD between the experiment with magnetic field turned off and on whose dose response curves are shown in Figure 3.9a and b, respectively.

In the experiment with magnetic field off the dynamics of the nanoparticles is dominated by the Brownian motion with the diffusion coefficient given by  $D_{\text{MNP}} = \mu_{\text{MNP}} k_b T \approx 10^{-11} \text{ m}^2 \cdot \text{s}^{-1}$ , where  $\mu_{\text{MNP}} = (6\pi\eta r_c)^{-1}$  is the mobility of a single MNP,  $k_b$  is the Boltzmann constant and T (293 K) the temperature [133]. On the contrary, the diffusion coefficient for a rotating nanorod is given by  $D_{\text{chain}} = \mu_{\text{chain}} k_b T$ , where  $\mu_{\text{chain}} = \frac{3\lambda}{4\pi\eta(r_0+r_c)^4 N^{*3}}$  [199] is the mobility for the rotating chain of particles approximated as a nanorod with negligible transverse dimensions compared to the longitudinal one and  $\lambda$  ( $2.5 \cdot 10^{-10}$  m) is the mean free path of water molecules.

Since the temperature measures the average kinetic energy per particle, the increase of the average of kinetic energy – due to the synchronous rotation of the chains – can be described in terms of temperature increase. Thus, an effective temperature can be introduced:

$$T_{eff} = \frac{E_k}{k_b} + T \quad 3.95$$

where  $E_k = \frac{1}{2}I\omega^2$  is the mean kinetic rotational energy per chain due to the rotating magnetic field,  $I = \frac{1}{12}m_{MNP}[2(r_0 + r_c)]^2N^3$  ( $7 \cdot 10^{-22}$  kg·m<sup>2</sup>) is the moment of inertia of the chain,  $m_{MNP}$  ( $\approx 1 \cdot 10^{-18}$  kg) is an estimate of the mass of a single MNP, and  $\omega$  ( $5 \cdot 2\pi$  rad·s<sup>-1</sup>) is the angular rotational frequency. Since  $\frac{E_k}{k_b T} \simeq 90$ , in presence of the magnetic field, the diffusion is driven by the kinetic energy instead of the thermal agitation, giving rise to an effective diffusion coefficient  $D_{eff} = \mu_{chain}k_b T_{eff}$ . The latter compared to the diffusion coefficient of a single nanoparticle ( $\frac{D_{eff}}{D_{MNP}} \approx 2 \cdot 10^3$ ), indicates that the rotating magnetic field enhance liquid phase transport operations beyond what can be accomplished in the classical diffusion paradigm. Furthermore, the increase in the diffusion coefficient also increases the probability that the nanoparticles will collide and form a specific bond recognizing the same target (Figure 3.13c and d). When the magnetic micromixing phase ends, the magnetic field is turned off causing the destruction of all non-specific magnetic bonds and selecting only the biological ones (Figure 3.13e).

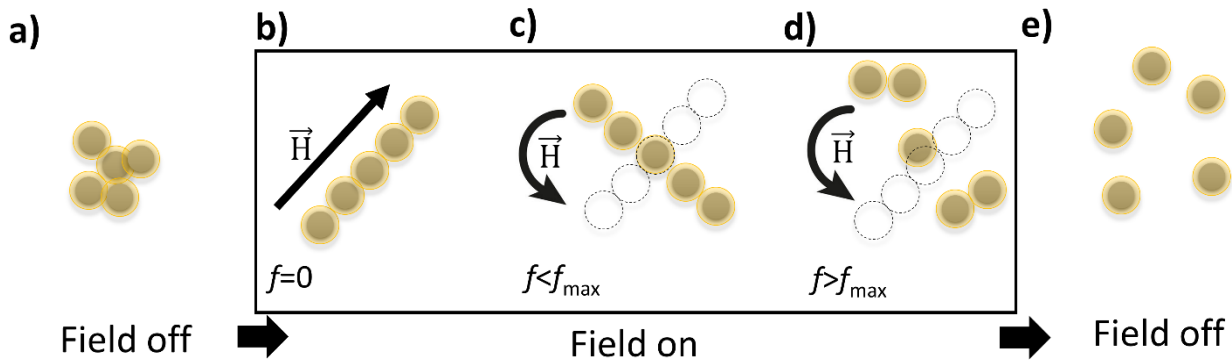


**Figure 3.12.** Schematic modeling of the formation and dynamics of chain-like structures. a) When the magnetic field is turned off the MNPs are found in the form of pellet. b) When the magnetic field is turned, the MNPs form chain-like structures along the direction of the external field. c) If the magnetic field rotate at a frequency  $f < f_{max}$  the structure of the chain remains intact and rotates synchronously with the field. d) If the magnetic field rotate at a frequency  $f > f_{max}$  the structure of the chain can be crack. e) When the magnetic field is turned off the chains are destroyed and the MNPs isolate again. The breakdown frequency  $f_{max}$  was determined experimentally to be 10 Hz.

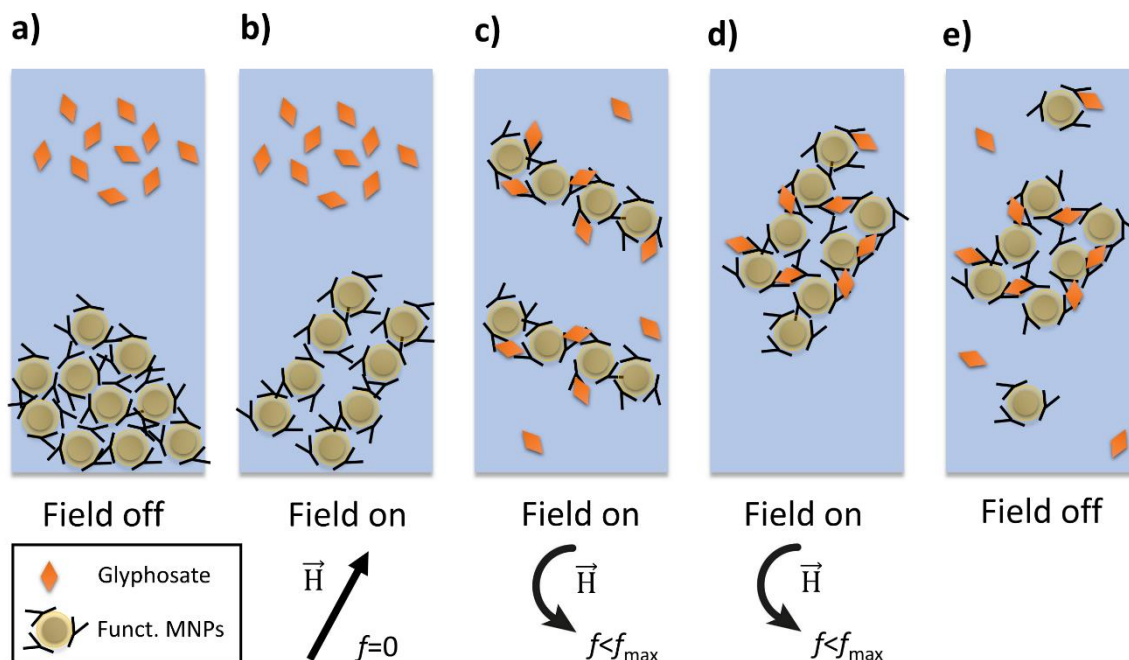


**Figure 3.13.** Schematic modeling of the micromixing phase. a) At the initial stage the functionalized MNPs are in the form of pellet and the magnetic field is turned off. b) When the magnetic field is turned on the MNPs form chain-like structures along the direction of magnetization. c) and d) When the magnetic field rotate at a frequency  $f < f_{\max}$  the structure of the chain remains intact and rotates synchronously with the field. During the micromixing phase the rotating chains have an increased probability to recognize the analyte and to encounter other chains in solution owing to enhanced diffusion ( $\frac{D_{chain}}{D_{MNPs}} \simeq 2 \cdot 10^3$ ). e) When the magnetic field is turned off at the end of the micromixing phase, the magnetic bonds disappear while the biological ones due to the recognition of the analytes persist and are detected during the absorbance measurements.

### 3.6 Conclusions

One of the limiting factors in the sensitivity of any assay involving the liquid phase is the collision rate among the particles, which is particularly low when the motion relies only on the thermal diffusion and the size of the particles is relatively large as it is the case with nanoparticles. We demonstrated that the core@shell nanoparticles with magnetic core can be effectively stirred by a rotating magnetic field. Under the action of such a field, nanoparticles form provisional chain-like agglomerates in a volume as small as 100  $\mu\text{L}$  that acquire a kinetic energy that largely overcomes the otherwise low thermal agitation. Such a response can be considered an example of enhanced diffusion by magnetic field whose applications include not only biosensing, but even contexts in which transport properties are of paramount importance like drug delivery [200].

The micromixing of antibody functionalized core@shell nanoparticles is beneficial for the target recognition and results in an improvement of the sensitivity of two orders of magnitude in comparison to the response measured by relying only on the thermal diffusion (magnetic field turned off). We applied the micromixing to a colorimetric immunosensor based on gold-coated magnetic

nanoparticles functionalized with IgG-EPSPS antibody for the detection of glyphosate in water for which we reached the LOD of  $20 \text{ ng}\cdot\text{L}^{-1}$ . Beside a very low LOD, high specificity and ease-of-use are the additional main strengths of the proposed assay. Specificity is ensured by the presence of IgGs and by the functionalization method used, whereas the transducer and strategy adopted to realize the magnetic field do not require any unwieldy equipment since the analysis consists of mixing a colloidal solution (sensing reagent) with a (liquid) sample in front of the rotating wheel shown in Figure 3.1b with a subsequent reading of the optical absorbance.

The limit of detection reached by the assay proposed here is lower than the regulatory limits established by the European Union for glyphosate in drinking water making it suitable for monitoring a water distribution network. Moreover, the portability of the whole system makes it attracting even for on-site analysis for any kind of water (e.g. surface and ground water). It is worth to remark that – as for any immunoassay – the biosensor described here can be designed for other targets by simply changing the antibodies.

## Chapter 4. Magneto resistive biosensor

The synthesis of noble metal modified magnetic particles as high-performance substrate that are easily functionalizable and possesses good dispersibility and stability, as well as strong magnetic response for high sensitivity magnetoresistive biosensors is still a challenge. Here, we reported a fast, simple, and effective protocol for coating commercial magnetic nanoparticle (MNP) clusters with gold nanoparticles (AuNPs). The resulting core@satellite magnetic particles (CSMPs), consisting of isolated AuNPs (satellites) stuck onto an aggregate of individual iron oxide crystals (core), are deeply characterized. In particular, the morphological, optical, hydrodynamic, magnetic, and surface charge properties are compared with those exhibited by the commercial MNP clusters. The proposed coating procedure endows the magnetic core with stability and ductility without resulting detrimental for their magnetic properties. Considering these features, the magnetic CSMPs are expected to be a versatile substrate for high-performance magneto resistive (MR) biochips. This was verified by the detection of Human IgG with a detection limit at picomolar level using a MR biochip that comprises 6 sensing regions, each one containing 5 U-shaped spin valve (SV) sensors (30 SV sensor in total), equipped with a unique highly-portable detection platform properly designed to achieve a point-of-care device. Antibodies were immobilized in upright orientation and close-packed configuration by photochemical immobilization technique (PIT) on the MR sensor and CSMPs allowing to considerably simplify the functionalization procedures and improving the biosensing effectiveness. Therefore, the novel CSMPs have an enormous potential for excellent sensing applications, especially in the target protein quantitative detection field, with a LOD at picomolar level, quick response (within 1 hour), potential multiplexing analysis (up to 6 different analytes at the same time) and signal redundancy (up to 30 measurements).

**Paragraph 4.1** contains an overview of the content outlined in the Chapter highlighting the novelty points and scope of the work. **Paragraph 4.2** briefly summarized the theoretical basis for understanding the phenomenon of the magneto resistive (MR) effect. In **Paragraph 4.3** are described the materials and methods exploited to carry out the experiments. In **Paragraph 4.4** core@satellite MNPs are fully characterized and compared with commercial magnetic nanoparticles. The main biosensing results are presented in **Paragraph 4.5**. The conclusions of the work are drawn in the **Paragraph 4.6**.

## 4.1 Overview

The ability to manipulate and control objects at nanoscale level is currently a topic of great interest in several field of applications ranging from diagnostic imaging to biophysics [83,84]. Magnetic nanostructures represent a smart tool to achieve the nanometric control by means of external magnetic fields.

Recently, several protocols to coat MNPs with a layer of a noble metal have been developed to improve the nanoparticle stability and durability [201], creating the so-called core@shell structures [202,203]. In particular, gold is usually preferred for its surface chemistry and biocompatibility [14,15], allowing the adoption of well-known functionalization techniques to link bioreceptors [16]. However, core@shell MNPs are not yet routinely adopted due to their complex fabrication procedures, the need for well-equipped laboratories, and limited availability on the market [17]. Additionally, there is a measurable decrease in the saturation magnetization with gold coating due to diamagnetic shielding resulting in a weakening of the magnetic properties of the nanoparticles [204,205]. Due to these obstacles, core@shell MNPs with good dispersity, stability and strong magnetic responsiveness have been scarcely reported. Several strategies have been studied to overcome these issues, among them one of the most promising has led to the development of the so-called core@satellite nanoparticles [206,207]. The latter exhibits isolated nanoparticles on the surface instead of a uniform coating layer. This arrangement allows to exploit all the advantages offered by gold surface chemistry – such as the possibility to anchor antibodies – without resulting detrimental for the magnetic properties. On the other hand, recent advances in the surfactant-assisted approaches for the direct aggregation of iron oxide nanoparticles into cluster-like entities show enhanced saturation magnetization, reduced coercive field at low temperature, higher blocking temperature, and a flatness of the field-cooled curves compared to those of individual nanoparticles [208,209].

In this work, we reported a fast, simple, and effective protocol for gold coating of commercial magnetic nanoparticle ( $\text{Fe}_3\text{O}_4$  MNP) clusters. This protocol triggers the formation of a rough shell covering the MNP cluster (diameter  $\approx 250$  nm) with gold nanoparticles (AuNPs) of smaller size (radius  $\approx 10$ -15 nm) (Figure 4.1a). The resulting core@satellite magnetic particles (CSMPs) were deeply characterized. In particular, the morphological, optical, hydrodynamic, magnetic and surface charge properties were compared with those exhibited by the commercial MNP cluster. We have shown that the coating procedure confers greater stability and ductility to the MNP cluster without the magnetic properties being adversely affected.

Furthermore, the CSMPs were applied in a biosensing experiment relying on a high-performance magneto resistive (MR) biochip [210]. MR sensing is based on the detection of the fringe magnetic field produced by MNPs when polarized by an external magnetic field (Figure 4.1b). The lab-on-a-

chip device was comprised of 6 sensing regions each one containing 5 U-shaped spin valve (SV) sensors (30 SV sensor in total), as previously described [211]. The device was manufactured by INESC-MN (Lisbon, Portugal). This is not a device on the market but a prototype made for research purposes which has been adapted to the experiment carried out in this work by the PhD candidate. It is possible to functionalize each sensing region with a different antibody so that the present biosensing setup is particularly suitable for both signal redundancy and simultaneous monitoring of different antigens at low concentrations (6 targets at the same time), paving the way for potential high-throughput and multiplexed analysis. The biochip features a unique and highly-portable detection platform [212] specifically designed to be used as a point-of-care (POC) device. The possibility of carrying out multiplex measurements on field with high-performance make this device particularly interesting for the identification of biomarker panels with high signal redundancy.

As it concerns the functionalization procedure, we used the well-established Photochemical Immobilization Technique (PIT) [44]. This technique, based on a selective UV-activation of antibodies (Abs), has proven to be an effective and competitive methodology since it is rapid and user-friendly and leads to strong (covalent) and conveniently oriented bonds of Abs on the sensor surfaces, without affecting the intrinsic selectivity of the bioreceptors [31,107,186,213]. The use of the PIT, in combination with a MR sensor and CSMPs, is a novelty element and allows to considerably simplify the functionalization procedures and to improve the sensing performance.

As a preliminary case study, CSMPs were successfully applied to MR biochip, for human immunoglobulin (IgG) detection in simulated samples achieving excellent sensing performance (LOD at picomolar level), quick response (within 1 hour), potential multiplexing analysis (up to 6 different analytes at the same time) and signal redundancy (up to 30 measurements). Considering this result, the CSMPs consisting of isolated AuNPs (satellites) stuck onto an aggregate of magnetic particles (core), with good dispersity and stability, strong magnetic responsiveness and good signal reproducibility, can be potentially used as an effective and versatile substrate in practical applications, including environment monitoring, food safety, pathogens detection, etc. Especially, with the help of MR biochip, the core@satellite magnetic particles have the potential to perform quantitative detection in complex system.

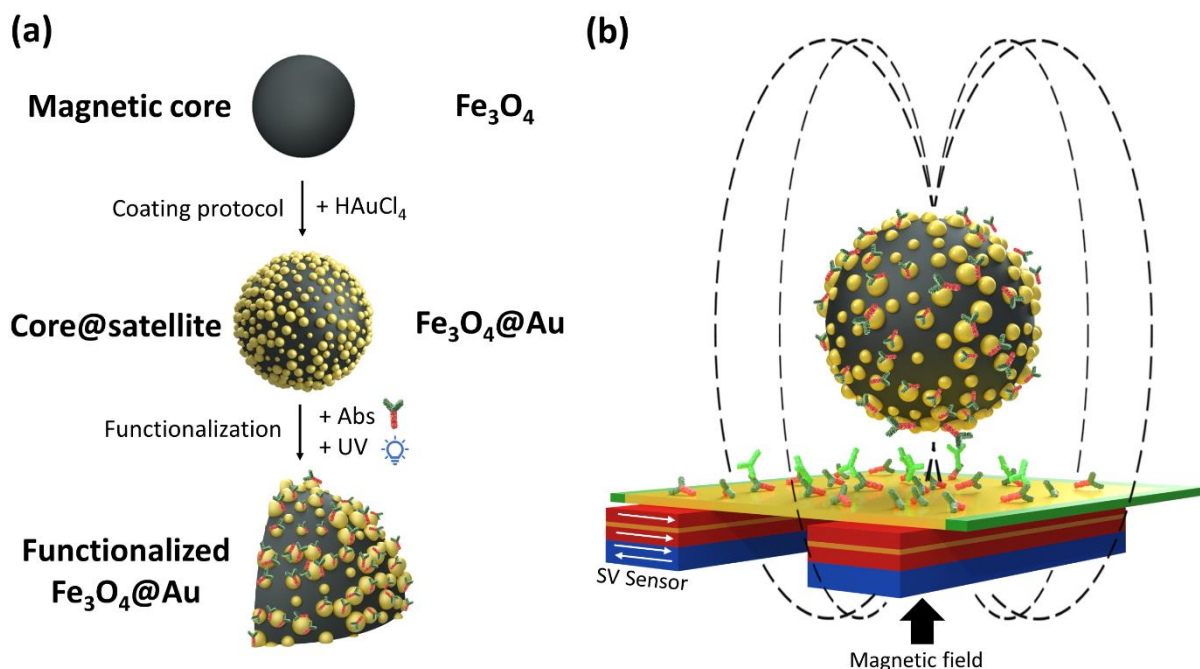


**Figure 4.1.** a) Commercial magnetic particles ( $\text{Fe}_3\text{O}_4$  MNPs) clusters (diameter  $\approx 250$  nm) are gold coated with smaller AuNPs (radius  $\approx 10$ -15 nm) by means of a coating protocol involving sodium citrate and tetrachloroauric acid. The resulting core@satellite magnetic particles (CSMPs) are functionalized by means of the Photochemical Immobilization Technique (PIT). b) Schematic representation (not in scale) of the magneto resistive (MR) chip detection system. The gold pad over the spin valve (SV) sensor was functionalized by PIT as well. The MR working principle is the detection of the fringe magnetic field created by the CSMPs on the sensor surface when an external magnetic field is applied. The antibodies on the chip surface recognize the target in solution that is recognized by the functionalized CSMPs in a sandwich scheme.

## 4.2 The magneto resistive effect

### 4.2.1 Spin Valve sensors

The physical working mechanism underlying spin valve sensor relies on the magnetoresistive (MR) effect [90]. In the presence of a stratified structured material such as that shown in Figure 4.2, it is observed that the movement of conduction electrons between the ferromagnetic (FM) layers through the magnetic (M) layer is influenced by the spin of the electrons. In particular, for a spin valve sensor composed by  $\text{FM}_1/\text{M}/\text{FM}_2$ , two currents can be distinguished, each one associated with a value of the spin of the electrons. The two currents behave differently due to the different relative orientation of the FM layers and the spin of the electrons. In particular, at the interface between different materials that build the SV sensor, the probability of scattering for electrons with spin up and down will be different.

The FM layers of spin valve structures can have parallel or anti-parallel moments (Figure 4.2a and b). In the first case, a spin-down electron will have a greater scattering probability than a spin-up electron, meaning that there exists a resistivity channel for spin-up electrons which lowers the overall

resistance of the device. In the second case, spin-down and spin-up electrons will both have a higher scattering probability in one of the FM layers and a lower scattering probability in the other creating two channels with the same resistivity. The difference in terms of resistance between the parallel and the antiparallel configuration is known as the MR ratio:

$$MR = \frac{R_{\uparrow\downarrow} - R_{\uparrow\uparrow}}{R_{\uparrow\uparrow}}, \quad 4.1$$

where  $R_{\uparrow\downarrow}$  and  $R_{\uparrow\uparrow}$  are the resistance of the sensor in the anti-parallel and parallel configuration.

Right after their introduction in the market, these sensors were employed for several commercial applications, such as memory devices, automotive sensor equipment, and earth field correction tools. Only later on their effectiveness in the detection of biological events has been proven [101,214–217].

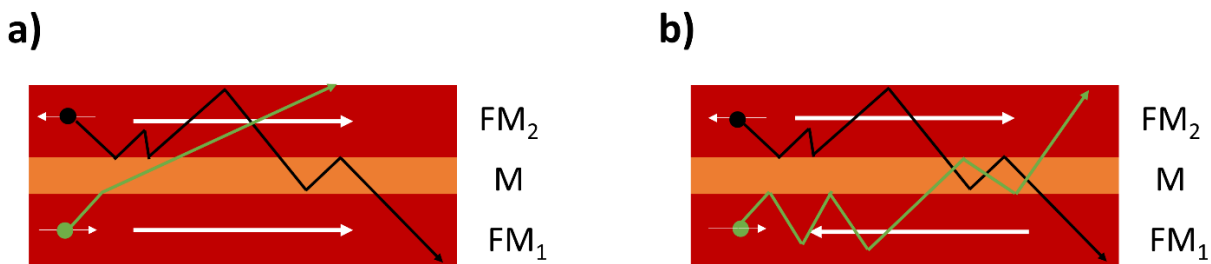


**Figure 4.2.** Schematic representation of a SV sensor. The two channels conduction for spin-up and spin-down electrons is illustrated. a) In the parallel configuration of the SV sensor, a spin-down electron will have a greater scattering probability than a spin-up electron, in the case of the anti-parallel configuration there are no differences in the scattering process.

#### 4.2.2 MNPs detection in DC mode

Magnetic nanoparticles are detected by the magneto resistive sensor by their field fringe field. The latter induces a change in the resistance of the chip that is used as sensing parameter. Since the nanoparticles employed in this study are superparamagnetic – and thus not showing any remanent field – they must be polarized in order to produce a fringe field. To date, several methods have been studied to polarize nanoparticles which can be divided into two categories the ones using constant magnetic field (DC) and the others using time-varying magnetic fields (AC). The previous nomenclature simply derives from the fact that in these applications it is generally preferred to use currents, continuous (DC) or alternating (AC), to generate the magnetic fields instead of permanent magnets. For the sensor described in this Chapter, DC field polarization was the one that proved to be most suitable, so the particles were polarized by a constant magnetic field. The more widespread way to magnetize the magnetic particles is to apply the polarizing field in the  $x$ -direction ( $H_x$ ) as depicted in Figure 4.3.

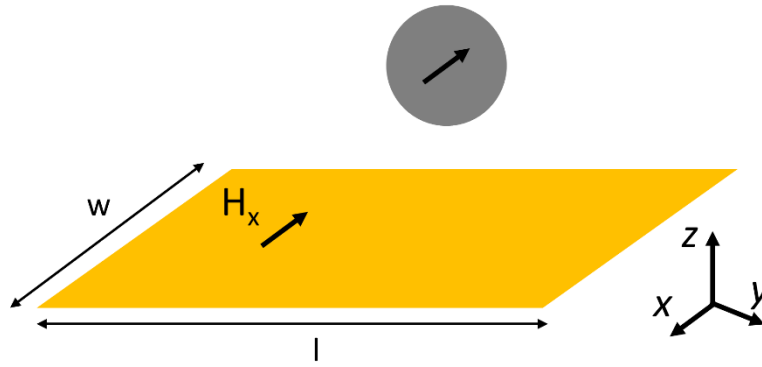


**Figure 4.3.** Schematic representation of the detection system using a DC polarization along  $x$ -axis. Adapted from .

In this case, a magnetic particle generates a fringe field in  $x$ -direction with a sign opposite to the polarizing field. The intensity of the polarizing field must be chosen carefully. In fact, while high polarization fields increase the magnetic moment, and thus also the fringe field of magnetic nanoparticles, there is, however, a risk that the sensor will fall out of the linear response zone. As can be noticed in Figure 4.4, the sensor resistance changes linearly with the applied field approximately in the range  $(-35; 35)$  Oe, while outside this range the resistance variation is non-linear (low field zone) or negligible (saturation zone). Therefore, the polarizing field has to be chosen in such a way to realize a trade-off between the polarization of MNPs and the MR sensor. To this end it is important to assure that the sensor is not saturated otherwise no resistance variation due to the presence of magnetic particles can be observed. This problem can be overcome by using two different polarization fields for the particles and MR sensors. However, putting a solution of this kind into practice significantly makes the implementation of the experimental apparatus harder. In fact, by choosing the same polarization field for the MR sensor and MNPs was possible to use a single coil in the detection platform (Paragraph 4.3.5).

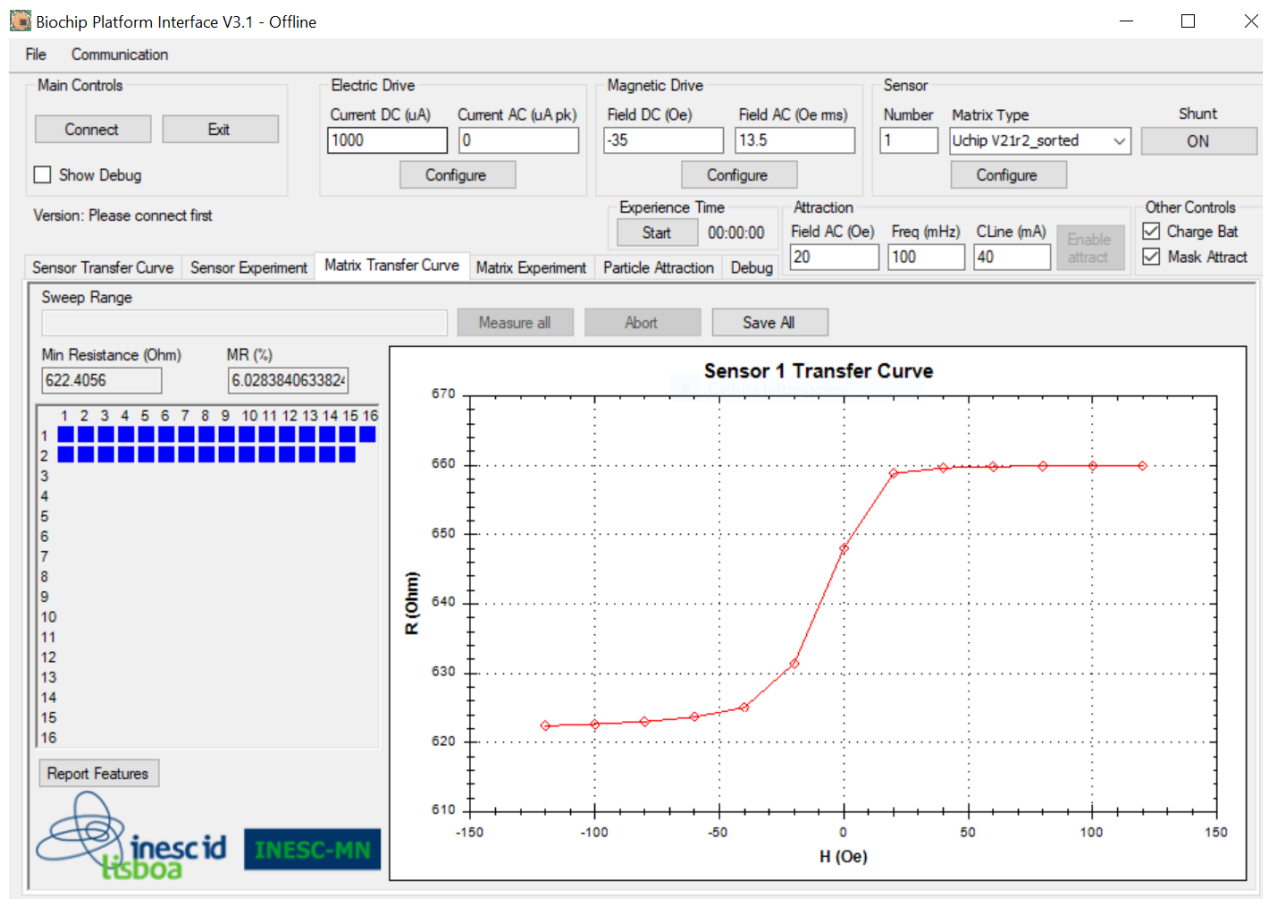


**Figure 4.4.** Transfer curve of a single U-shaped spin valve (SV) sensor ( $80 \times 2.6 \mu\text{m}^2$ ).

For biosensing applications, the MNPs are usually coated with streptavidin, a protein that has high affinity to biotin. In this way, a biotin molecule can be attached to the target biomolecule by a biotinylation process so that the labelling is made by streptavidin-biotin interaction. This indirect functionalization mechanistic approach is costly, time-consuming and inefficient as well as often not feasible due to the limited applicability of biotinylation methods. To overcome this issue, the idea of using MNPs decorated with gold satellite nanoparticles allows to exploit the well-known functionalization techniques and the Photochemical Immobilization Technique (Paragraph 1.2.3) that was employed in this work.

The experimental procedure by which nanoparticles are actually detected is explained in Paragraph 4.3.6, briefly antibodies functionalized core@satellite MNPs are put into contact to the chip surface. The latter was functionalized and exposed to the target of interest in advance. If the target and the antibody on core@satellite particles are complementary, after a washing step the magnetic particles remain attached to the surface. Upon magnetization by an external magnetic field, the markers generate fringe fields, which are detected by magneto resistive sensors

As an alternative strategy, the preconcentration technique could be used. Instead of exposing the sensor surface to the target, it is possible to introduce the MNPs into the solution to be examined so that they can be manipulated by external magnetic fields to rake the target in solution and later conveyed on the sensing surface. Moreover, in any sensing setup, magnetic forces for stringency

control and for focusing the biological target to the sensor area could be exploited. This is usually accomplished by building a circuit of permanent magnets around the sensitive regions that induce the MNPs to stay close to the functionalized areas.

### 4.2.3 Considerations on sensitivity

The sensitivity of a MR biosensor depends on the length,  $l$ , and the width,  $w$ , of the device

$$MR = R_0 \frac{l}{w}, \quad 4.2$$

where  $R_0$  is a constant that depends on the spin valve structure. In addition, there is a direct relationship between the number of active probe biomolecules on the surface and the probability of capturing a specific target biomolecule in a test solution. Therefore, a larger biologically active area increases biological sensitivity [218].

The dynamic range of the sensor is directly proportional to the sensor area since more magnetic particles fit in the sensor area and can therefore be detected. However, as can be observed in Figure 4.5a, as the sensor area increases, the average magnetic fringe field detected of a MNPs of a fixed tupe decreases.

In order to achieve a balance between limit of detection, dynamic range, and biological sensitivity, a trade-off must be made. Consequently, the sensor characteristics can be modified to fit the problem to be addressed. Large sensors can be employed for applications requiring larger dynamic ranges and higher target concentration detection (i.e. disease monitoring, gene expression analysis). Small sensors will be used for applications demanding low target concentration detection and small dynamic range (i.e. yes/no detection such as in disease diagnostics).

The distance between the sensor free layer and the magnetic particle itself is another important aspect in the optimization of the sensor sensitivity to magnetic particles. Usually, the free layer is covered with a passivation and a gold layer. These two layers aim to protect the sensor from possible corrosion caused by biochemical solutions used in the bioassays. In addition, the gold layer allows to considerably simplify the functionalization procedures and to improve the sensing performance. In any case, the thickness of the passivation layer and the gold layer should be as small as possible since as shown in Figure 4.5b, the magnetic field of fringe detected decreases rapidly as the distance of the MNP from the free layer increases.

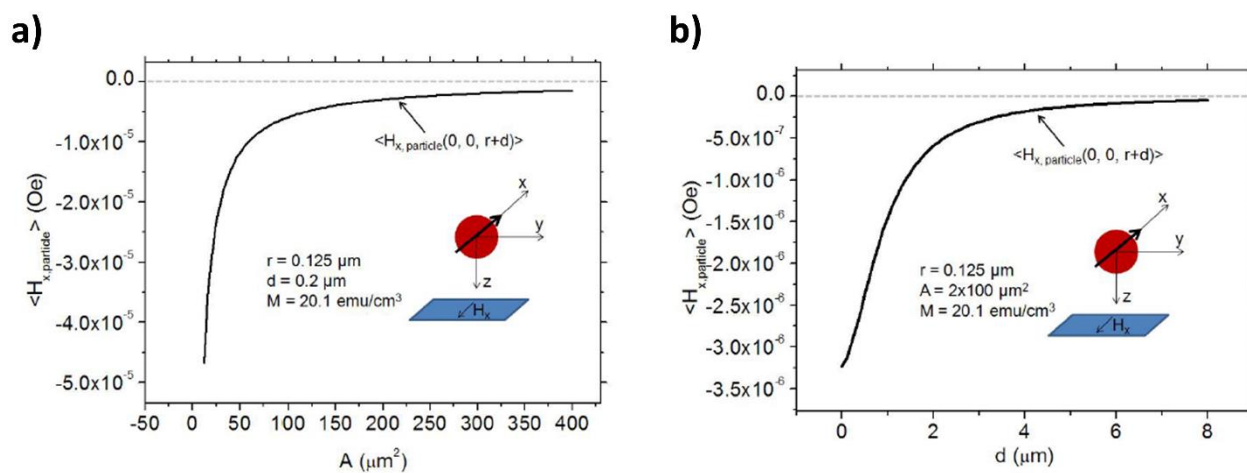


**Figure 4.5.** Average magnetic field of one particle in the center of the sensing area in function of the sensor area a) and separation between the sensor and the particle b). Reproduced from [218].

## 4.3 Materials and Methods

### 4.3.1 Reagents and materials

The water used in the preparation of any solution was MilliQ, while tetrachloroauric acid ( $\text{HAuCl}_4 \cdot 3\text{H}_2\text{O}$ ), sodium citrate ( $\text{Na}_3\text{C}_6\text{H}_5\text{O}_7$ ), and Polysorbate 20 (Tween<sup>TM</sup> 20,  $\text{C}_{26}\text{H}_{50}\text{O}_{10}$ ) were purchased by Sigma Aldrich. All the antibodies used for this study were purchased from ImmunoReagents. Bovine serum albumine (BSA) was purchased from Pierce. The magnetic dextran iron oxide composite nanoparticles were purchased from Micromod (product name nanomag<sup>®</sup>-D, product code 09-54-252). They have a core@shell like structure with a core of magnetite and a dextran shell [219]. The magnetite core consists of aggregates of individual iron oxide (magnetite) crystals with diameters of 5-15 nm. Their surface has been modified with PEG 300 in order to prevent the unspecific protein binding on the particle surface.

### 4.3.2 Synthesis of CSMPs

CSMPs were made by incubating AuNPs with dextran iron oxide composite particles. In a typical experiment 100  $\mu\text{L}$  of magnetic particles, as from the stock, were added to a solution containing 15 mL of MilliQ water. The solution was heated until 95  $^\circ\text{C}$  with vigorous stirring by using a mechanical motor stirrer (Heidolph RZR 50, Germany). Once the temperature was reached, 1 mL of sodium citrate (100 mM) and 50  $\mu\text{L}$  of a  $\text{HAuCl}_4 \cdot 3\text{H}_2\text{O}$  (10  $\text{mg} \cdot \text{mL}^{-1}$ ) were added to the solution one after the other. After 2 minutes, when the solution changed color from an initial brown (Figure 4.6a) of the magnetic particles to a weak purple, 50  $\mu\text{L}$  of a  $\text{HAuCl}_4 \cdot 3\text{H}_2\text{O}$  of the same concentration were added. At this point the solution was let cool down keeping the same stirring speed until it reached the room

temperature (RT). Once at RT, the CSMPs underwent 5 washing steps where magnetic attraction was employed to remove the supernatant in excess. After magnetic separation, the particles were resuspended in 10 mL in a solution of MilliQ water and Tween™ 20 (0.005 %) (Figure 4.6b). As a result of such a procedure a colloidal solution of 10 mL of CSMPs ( $5 \cdot 10^9$  nps·mL<sup>-1</sup>) was obtained. It was noted that resuspending the CSMPs in a solution of MilliQ water and Tween™ 20 (0.005 %) was the best way to stabilize the nanoparticles and store them for several weeks.

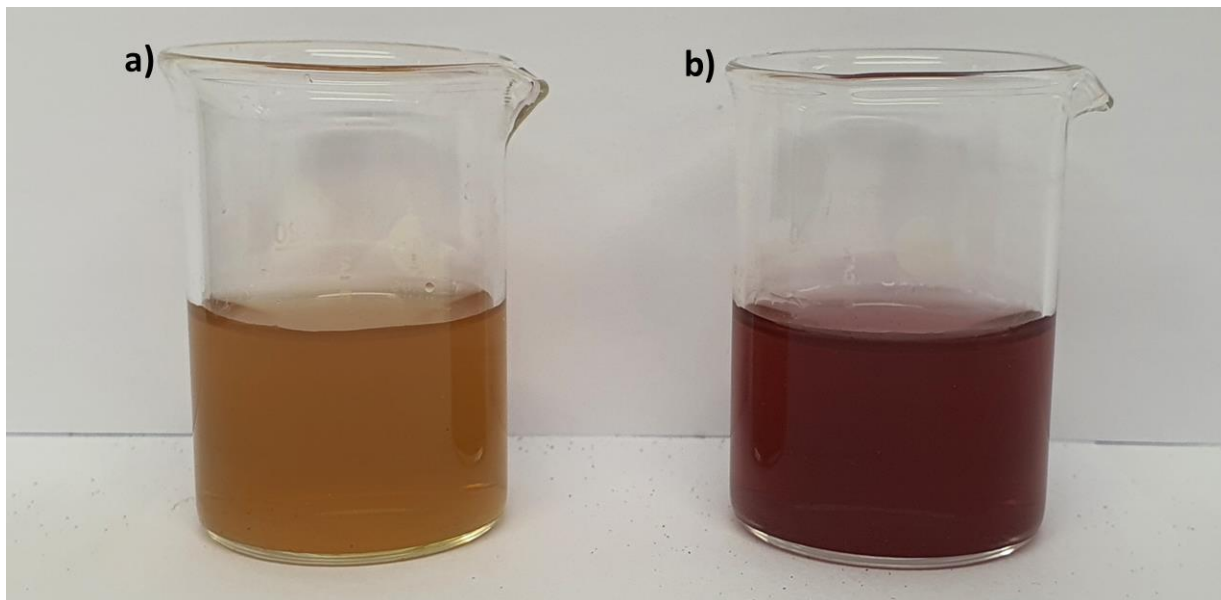


**Figure 4.6.** a) suspension of MNPs as from the stock, b) CSMPs suspension after the coating process. The particle concentration was  $3 \cdot 10^9$  MNPs·mL<sup>-1</sup> in both cases.

### 4.3.3 MR sensors fabrication and cleaning

The MR biochip contains 6 sensing regions enclosed in a gold squared frame ( $300 \times 300 \mu\text{m}^2$ ) each one containing 5 U-shaped spin valve sensors ( $80 \times 2.6 \mu\text{m}^2$ ) coated with a gold pad ( $35 \times 13 \mu\text{m}^2$ ) for a total of 30 SV sensors (Figure 4.7). The 6 sensitive regions are arranged in two parallel rows, 3 on the left side and 3 on the right side. The several microfabrication steps involved in the manufacturing of the SV biochips have been previously described [216]. Briefly, the SV materials were deposited by Ion beam in a Nordiko 3000 tool [220] on a 150 mm diameter Silicon wafer, passivated with 100 nm of alumina ( $\text{Al}_2\text{O}_3$  deposited by sputtering from a ceramic target, with a power of 200 W, 4.5 mTorr). The SV multi-layer structure was the following: Ta 20 nm/NiFe 25 nm/CoFe 28 nm/Cu 26 nm/CoFe 24 nm/MnIr 70 nm/Ta 50 nm. The sensors were patterned using direct write laser lithography (Heidelberg DWL 2.0, diode laser wavelength 405nm) and transferred to the substrate by ion milling etching (Nordiko 3000, using an Ar<sup>+</sup> beam with 29 mA ( $92 \mu\text{A}/\text{cm}^2$ ), acceleration  $V_+ = 500$  V, extraction  $V_- = 200$  V, at a pressure  $p = 2.4 \cdot 10^{-4}$  Torr and beam-to-surface angle =  $70^\circ$  for 400 s) and protected with a 350nm thick  $\text{Si}_3\text{N}_4$  passivation layer deposited by PECVD in an Oxford tool ( $\text{SiH}_4 = 20$  sccm,  $\text{N}_2 = 20$  sccm,  $\text{N}_2\text{O} = 980$  sccm, at a pressure of 1 Torr and  $300^\circ\text{C}$ ),

where the gold pads deposited were then defined over the sensors. Before every biosensing experiment, the chips underwent a cleaning process. The sensing region was rinsed multiple times with MilliQ water and Isopropyl alcohol (IPA). Once dried with compressed air they were exposed to an ultraviolet light/ozone plasma for 15 min at  $28 \text{ mW}\cdot\text{cm}^{-2}$  at 5 mm separation from the UV lamp inside an UVO cleaner machine from Jelight, (Irvine, CA, USA). The biochips can be recycled several times using the abovementioned procedure.

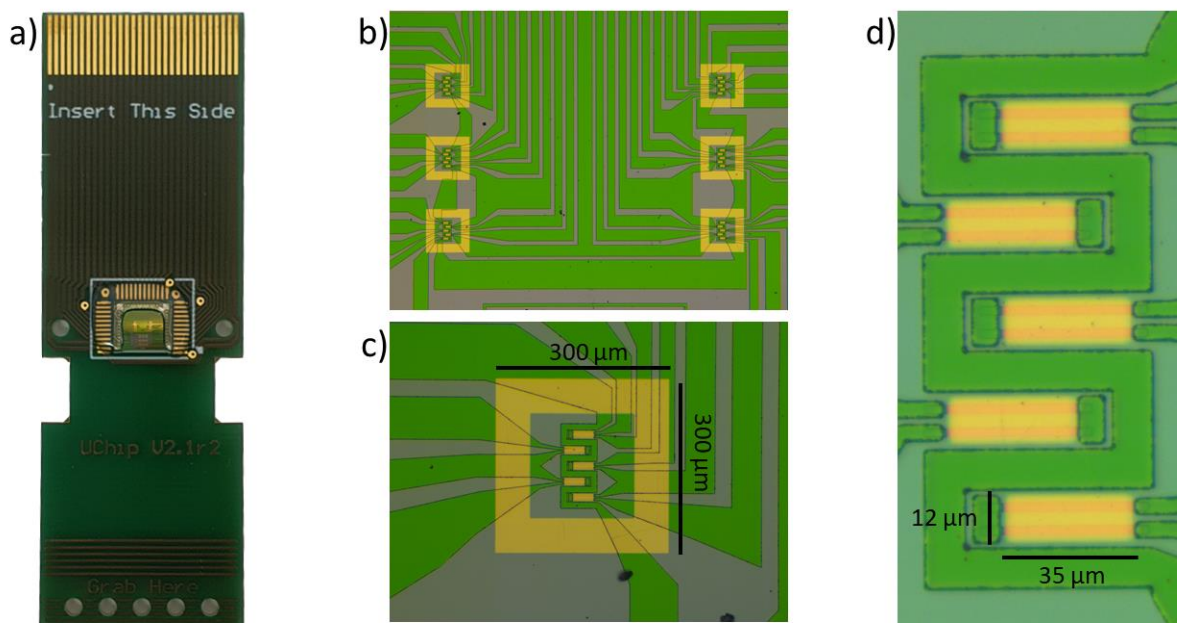


**Figure 4.7.** a) Image of the PCB carrier containing the chip. The gold stripes in upper part are connected to the chip in center, the contacts are covered with silicon to prevent water damage to the circuits. b) Microscope image (5x magnification) showing the 6 sensing regions. c) Microscope image (20x magnification) of one sensing region. d) Microscope image (50 x magnification) highlighting the sensors details, the gold squared frame ( $300 \times 300 \mu\text{m}^2$ ) contains the 5 U-shaped SV sensors ( $80 \times 2.6 \mu\text{m}^2$ ) covered by a gold pad ( $35 \times 13 \mu\text{m}^2$ ).

#### 4.3.4 Functionalization protocol

The MR sensor gold surfaces were modified with Abs, where each sensing region can be discretely functionalized with a different probe antibody. In this experiment half of the sensors were functionalized with Goat anti-Human IgG (in order to detect Human IgG) and the remaining half was functionalized with Donkey anti-Sheep IgG (negative control). To the best of our knowledge, this is the first time that the Photochemical Immobilization Technique (PIT) (Figure 1.4) [44] was employed in combination with MR sensors. PIT is a powerful and fast methodology whose effectiveness has already been confirmed in several biosensing applications [20,28,31,107]. It is based on selective UV-activation of Abs that leads to a strong covalent binding to noble metal surfaces that improve the detection efficiency of the immunosensor orienting the Abs with the fragment antigen-binding site (Fab) exposed to the solvent. The functionalization procedure via PIT involved the following steps: a quartz cuvette containing 1 mL of Abs dissolved in ultrapure water ( $25 \mu\text{g}\cdot\text{mL}^{-1}$ ) was irradiated by

UV light (lamp Trylight®) for 30 s, which is the optimal irradiation time for PIT; immediately after the irradiation the solution was manually spotted on the chip surface, one droplet covering the 3 sensing regions (Goat Anti-Human IgG for sensors from 1 to 15, Donkey Anti-Sheep IgG for sensors from 16 to 30); the substrates were left at room temperature inside a humid chamber for 10 minutes after which the unbound Abs were washed with MilliQ water. Once the unbound antibodies were removed, 30  $\mu\text{L}$  of a solution of 5% bovine serum albumine (BSA) were deposited on the surface of the chip in order to fill any unoccupied area left after functionalization in order to minimize non-specific contributions. The chip was incubated for 1 h after which it was washed with MilliQ water. Using a different protocol, also the CSMPs were functionalized by PIT. Firstly, a volume of 2 mL of the solution resulting from the abovementioned coating protocol was concentrated in a volume of 100  $\mu\text{L}$  by means of magnetic separation. Separately a 100  $\mu\text{L}$  of Abs solution ( $10 \mu\text{g}\cdot\text{mL}^{-1}$ ) was irradiated by UV light for 30 s and later was added in ten spikes (5  $\mu\text{L}$  each) to the CSMPs solution. The functionalized CSMPs were gently stirred for 10 minutes. As final step the CSMPs were magnetically separated from the solution in order to remove the antibodies in excess and resuspended in 10  $\mu\text{L}$  of water to be conveyed into the microfluidic circuit that crosses the sensors.

#### **4.3.5 Biochip experimental setup**

The biochip detection platform was fabricated as previously described [221]. Briefly, the system is divided into five main sections: the chip insertion site, the copper coil for magnetic drive, the battery, the USB connector, and the box containing the detection electronic circuit (Figure 4.8). The removable microfluidics circuit, made of Polydimethylsiloxane (PDMS), is placed above the chip with the possibility to be connected to any pumping system. The metal box has the purpose of shielding the circuits from external signals that could cause interference with the measurement process. The detection electronic circuit is composed by three main modules: a sensing and processing module (SPM), an autonomous communication module (ACoM) and analyzer module (AnM). Thanks to SPM and ACoM modules the platform can be directly connected to a PC and fully controlled using the specially designed graphic user interface (GUI) (Figure 4.9). Taking advantage of the AnM module, the acquired signals are processed in real time and transmitted to a digital analyzer that enables the user to control and follow the experiment. All the electronic circuitry for addressing, driving and reading out signals from spin-valve is implemented using off-the-shelf components. The developed platform is portable (15 cm x 13 cm x 4 cm) and capable of operating autonomously for nearly 8 hours. The battery can be recharged by the PC using the same connection used to operate the platform.



**Figure 4.8.** Detail of the biochip platform internals: 1) chip insertion site, 2) coil for magnetic drive, 3) battery, 4) box enclosing detection electronic, 5) USB port.

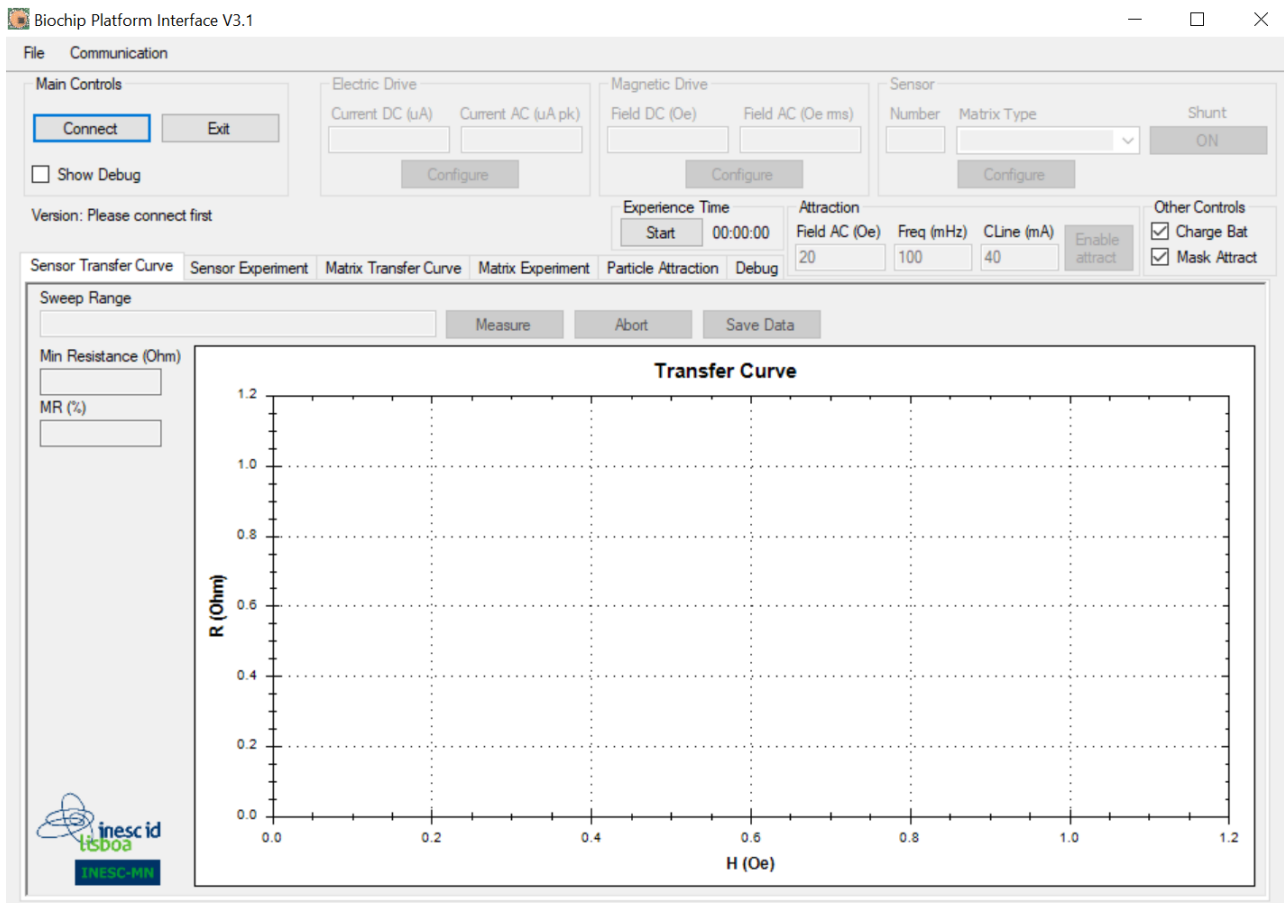


**Figure 4.9.** Screenshot of the graphic user interface (GUI) through which is possible to operate the platform.

### 4.3.6 Experimental procedure

30  $\mu$ L of a solution containing the antigen to be detected at fixed concentrations was spotted on the sensor, whose surface was functionalized with Abs and blocked with BSA as described in Paragraph 4.3.4. After being incubated for 1 h, the chip was washed with MilliQ water and inserted in the

specifically designed magneto resistive biochip platform (Paragraph 4.3.5). A U-shaped Polydimethylsiloxane (PDMS) microfluidic channel  $800 \times 300 \mu\text{m}^2$  (width  $\times$  height) was placed over the chip to transport the functionalized CSMPs over the sensing area. The measurements start with a voltage baseline acquisition of around 5-10 minutes. When the signal was stable, the CSMPs solution, functionalized and concentrated as described in Paragraph 4.3.4, was conveyed in the microfluidic circuit by means of a syringe pump (New Era Pump systems) at a flow rate of  $50 \mu\text{L}\cdot\text{min}^{-1}$  (Figure 4.10). The flux was stopped when the solution completely filled the channel meaning the CSMPs were over the sensing area. After 10 minutes, once the voltage signal of the sensors was saturated, the unbound CSMPs were washed out with water at a flow rate of  $150 \mu\text{L}\cdot\text{min}^{-1}$  for 5 minutes. If there were differences between the initial baseline voltage ( $V_{\text{baseline}}$ ) and the final voltage after the washing ( $V_{\text{washing}}$ ), a binding signal  $\Delta V$  was obtained. The binding voltage difference ( $V_{\text{baseline}} - V_{\text{washing}}$ ) was calculated either for the detection ( $\Delta V^{\text{p}}$ ) and the negative ( $\Delta V^{\text{n}}$ ) control sensors (Figure 4.10). Then, the mean value of the voltage variation for the negative control sensors  $\overline{\Delta V}^{\text{n}}$  was subtracted to the  $\Delta V^{\text{p}}$  for each positive sensor and finally each  $\Delta V$  was divided by the baseline voltage value of each sensor. Having control sensors entails innumerable advantages, including that of being able to subtract any drift (due to temperature or external interference) from binding signal and keep only the contribution due to the specific biological interaction. The sensors were biased with a 1 mA DC current, and the magnetic drive was set to 35 Oe DC. An additional time-varying magnetic field was employed with 13.5 Oe rms AC at 211 Hz. For each sensor, a transfer curve as the one in Figure 4.4, was acquired and the data was sequentially recorded at a bandwidth of 4 Hz and 2 samples per sensor.

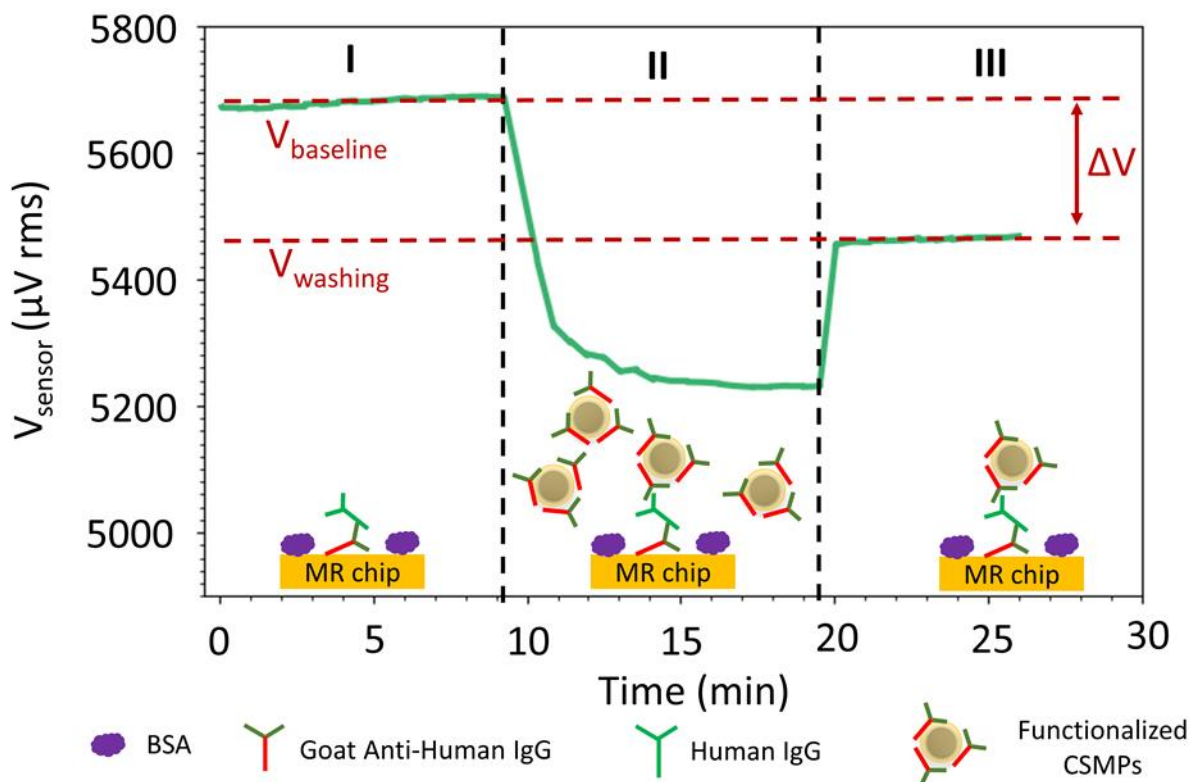


**Figure 4.10.** Typical dynamic response of the MR biosensor. On the y-axis the potential difference across the chip and on the x axis the time interval. The green line represents the response of the sensor in each of the following steps: (I) voltage baseline acquisition (flow rate  $50 \mu\text{L}\cdot\text{min}^{-1}$ ), (II) CSMPs interacting with the sensor (static), (III) washing step (flow rate  $150 \mu\text{L}\cdot\text{min}^{-1}$ ).

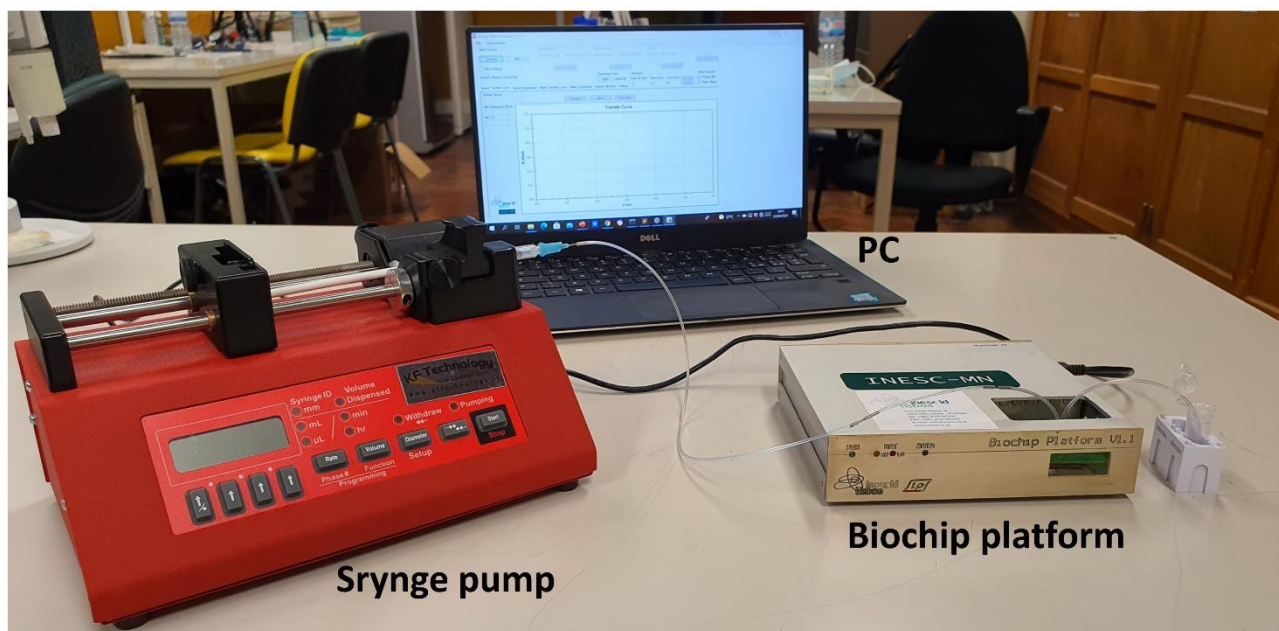


**Figure 4.11.** The experimental setup is shown in Fig S5, on the left a syringe pump; on the right the biochip detection platform connected to a PC through a USB connector for data acquisition.

### 4.3.7 Simulation workspace

The optical response of CSMPs was investigated by the finite-difference time-domain (FDTD) method implemented in Lumerical “FDTD solutions” tool. Maxwell’s equations are solved inside each unit cell in which the simulation workspace is discretized. Figure 4.12 depicts the scheme of the simulation workspace.

A single CSMPs was placed in a total-field scattered-field (TFSF) volume ( $500 \times 500 \times 300 \text{ nm}^3$ ) with a plane wave source on the bottom side. A photodetector (spectral resolution: 1 nm) was positioned on the opposite side to collect the transmitted light thereby retrieving the CSMPs extinction spectrum. The optical response was explored by a linearly polarized wave ( $0^\circ$ - $180^\circ$  polarization angle with an angular step of  $15^\circ$ ) in the range 400-800 nm travelling along the  $z$ -axis. The TFSF volume was embedded into a FDTD volume ( $2000 \times 2000 \times 2000 \text{ nm}^3$ ) filled with water (1.33 refractive index). Perfect matched layer boundary conditions were set on each FDTD side to warrant the perfect absorption of the incident radiation, avoiding back reflection effects. A discretizing mesh of 1 nm spatial resolution was adopted to ensure accurate results within a reasonable simulation time.

The CSMPs was modelled as a  $\text{Fe}_3\text{O}_4$  [222] ellipsoidal core (principal axes:  $a = 150 \text{ nm}$  and  $b = c = 100 \text{ nm}$ ) coated with 100 Au [222] spheres of a uniformly distributed radius in the range 10-15 nm. The Au spheres were randomly placed onto the  $\text{Fe}_3\text{O}_4$  core in such a way that their centre-to-centre distance was not shorter than 30 nm. The above-mentioned geometrical parameters were set in accordance to the actual morphologies observed in TEM images.

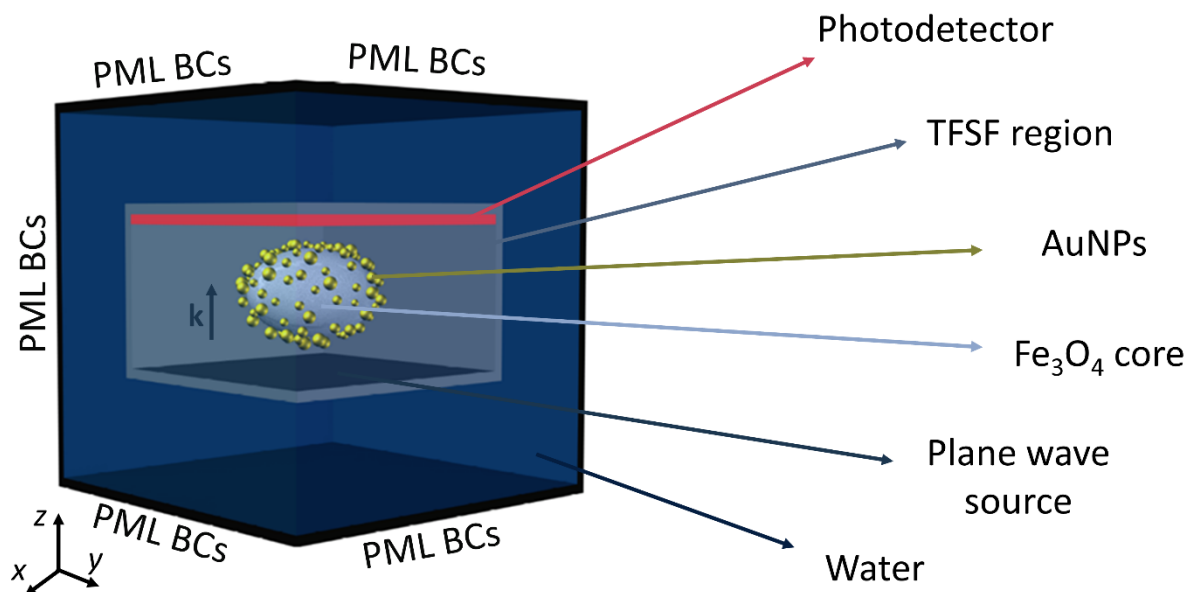


**Figure 4.12.** (a) Schematic representation of the simulation workspace in Lumerical’s environment consisting of light source, boundary conditions (BCs), photodetector, nanostructure (CSMPs) and embedding medium (water). A linearly polarized electromagnetic wave propagating along  $z$  direction was used to investigate the optical response of the CSMPs.

## 4.4 CSMPs Characterization

The AuNPs around the PEGylated MNP clusters are formed since the sodium citrate act as reductant of the tetrachloroauric acid. This process is favored by the high temperatures ( $> 90\text{ }^{\circ}\text{C}$ ) to which the solution is brought before adding the reagents and leads to the formation of small gold particles (seeds) that settle on the MNP clusters surface. The occurrence of this process is confirmed by the color change of the solution (from an initial brown to a light purple), effect due to the well-known surface plasmon oscillation whose frequency falls in the visible region [223]. When the color of the solution stops changing, more tetrachloroauric acid is added to the solution in order to grow the gold seeds on the MNP clusters surface until they reach dozens of nanometers of size (the solution turns red). The colloidal solution of CSMPs is realized thorough electrostatic interactions by citrate molecules that act as capping agents [224].

### 4.4.1 Morphology

Transmission electron microscopy (TEM) measurements were carried out to determine the morphology and shape of the particles. TEM micrographs were obtained using a FEI Tecnai G2 S-twin apparatus operating at 200 kV (LaB6 source). The particle powder samples were dispersed in water, then a small quantity of the solution was added on the carbon-coated copper grid (200 mesh) and let evaporate. Figure 4.13 (from a to f) shows the micrographs of the bare MNP clusters (a, b, c) as taken from the stock, in the upper panel and those of the CSMPs, coated with the abovementioned protocol, in the lower panel (d, e, f). As can be noted in panel a, where a single MNP cluster is depicted, this kind of clusters are non-spherical but irregularly shaped, this conformation is quite common for clustered-type dextran iron oxide composite particles [225,226]. As regarding the micrographs of CSMPs, small AuNPs (radius  $\approx 10\text{-}15\text{ nm}$ ) are visibly attached on the surfaces of the bigger MNP clusters (diameter  $\approx 250\text{ nm}$ ) as a result of the coating protocol (panel f).

### 4.4.2 Optical response

Both the MNP cluster and the CSMPs were characterized by UV–vis spectroscopy (Jenwayn6715 UV/vis spectrophotometer, United Kingdom). After the coating process, the color of the solutions changes from a strong brown (MNP clusters, Figure 4.6a) to a dark red (CSMPs, Figure 4.6b), that is a characteristic color of AuNPs solutions. The presence of AuNPs on the surface of the MNP clusters is confirmed by extinction analysis in UV-vis range. As can be noticed from Figure 4.13g, the

extinction spectra of the MNPs (dashed black line) does not show any extinction peak while the spectra of the CSMPs (solid red line) show a prominent peak at  $567 \pm 6$  nm. The CSMPs solution was washed with magnetic separation multiple times before the measurement (Paragraph 4.3.2) to ensure that the only contribution to the signal was originated by the AuNPs attached to the surface of the MNP cluster. In order to corroborate the experimental characterization, we simulated the optical response of an aqueous solution containing core@satellite particles by finite-difference time-domain (FDTD) method which we used to solve Maxwell's equations [188]. A detailed description of the simulation workspace is reported in Figure 4.12, whereas Figure 4.13 shows the normalized extinction of CSMPs (gold solid line). The experimental extinction spectrum (red solid line) is consistently reproduced by a simulation involving a distribution of 100 AuNPs with radius between 10 and 15 nm randomly distributed on the magnetic core. The plasmonic resonance peaked at 560 nm represents the response of the optically uncoupled AuNPs and it strongly depends on the nanoparticles shape, size and surrounding environment (magnetite and Tween™ 20 shell). On the other hand, the secondary peak at 660 nm arises from the dipolar coupling among nearest neighbors which give rise to a coupled mode at higher wavelengths [223] thus it mainly depends on the nanoparticle density and centre-to-centre distance distribution. Although the experimental spectrum does not exhibit two distinct plasmonic resonances, we can safely assess that more realistic but extremely time-consuming simulations including different magnetite morphologies and AuNP arrangement would lead to a broadening of the secondary plasmonic mode that would entail an increase of the extinction in the red band (600-800 nm) as experimentally observed.

#### 4.4.3 Surface charge properties

Zeta potential measurements were carried out with the Zetasizer Nano ZS instrument (Malvern Instruments Company, United Kingdom). The assessment of the zeta potential is crucial to provide an insight on the stability and the charge surface modifications of the colloidal solution of MNP clusters due to the gold coating [227]. As shown in Figure 4.13h (dashed black line) the bare MNP clusters in an aqueous solution exhibit a zeta potential distribution peaked around -3 mV. Such a low absolute values of the zeta potential is generally related to the instability of the colloidal solution [227]. On the contrary, the zeta potential distribution peak observed for CSMPs in water is about -30 mV (Figure 4.13h, solid red line), thus revealing a high stability of the colloidal solution. It is worth noticing that the negative shifting of the distribution is coherent with the adjoint of the AuNPs around the magnetic core. Indeed, the typical values of the zeta potential for AuNPs in aqueous solutions are highly negative [228].

#### 4.4.4 Hydrodynamic properties

In order to analyze the hydrodynamic behavior of the suspension of CSMPs, dynamic light scattering (DLS) measurements were performed with the Zetasizer Nano ZS instrument (Malvern Instruments Company, United Kingdom). Figure 4.13i shows the size distributions of a suspension of bare MNP clusters (dashed black line) and a suspension of CSMPs (solid red line) in MilliQ water. The size distribution for bare MNP clusters is unimodal and the average hydrodynamic diameter is about 260 nm with a standard deviation of 100 nm. On the other hand, the size distribution of the CSMPs is bimodal with a major and a minor mode distinguishable from each other. The average hydrodynamic diameter of the distribution is about 350 nm with a standard deviation of 80 nm for the major mode. The growth of the average hydrodynamic diameter with respect to that of the MNP clusters can be understood qualitatively as an effect of the AuNPs on the surface. However, since the nanoparticles are not spherically shaped and both size distributions are quite broad, a quantitative estimation of the thickness of the gold coating shells is unattainable. The minor mode of CSMPs size distribution is due to aggregates with diameter bigger than 1  $\mu\text{m}$  derived from the gold coating process. These by-products are just about 10 % of the whole nanoparticles population and can be easily removed from the suspension through precipitation before using the nanoparticles for biosensing applications.

#### 4.4.5 Magnetic properties

The magnetic properties of both MNP clusters and CSMPs were assessed with a vibrating-sample magnetometer (VSM) (DSM 880, Microsense, USA). The hysteresis loops (Figure 4.13l) were performed at 300 K and showed a decrease of around 9% in the saturation magnetization values  $M_s = 55$  and  $51 \text{ emu}\cdot\text{g}^{-1}$  respectively for MNP clusters and CSMPs. The weakening of the magnetic properties of MNPs when coated with gold is a well known phenomena [229,230] and it is connected with the diamagnetic nature of gold and it is an unavoidable trade-off if MNPs are intended to be used in a biological environment. In our case, the gold diamagnetic contribution was not subtracted and the additional mass of the gold is expected to reduce  $M_s$  accordingly. However, the small reduction of the saturation magnetization did not impact of the experiment noticeably. During the measurements the intensity of the magnetic field applied to the particles is of 35 Oe, falling into the linear range of the hysteresis curve.

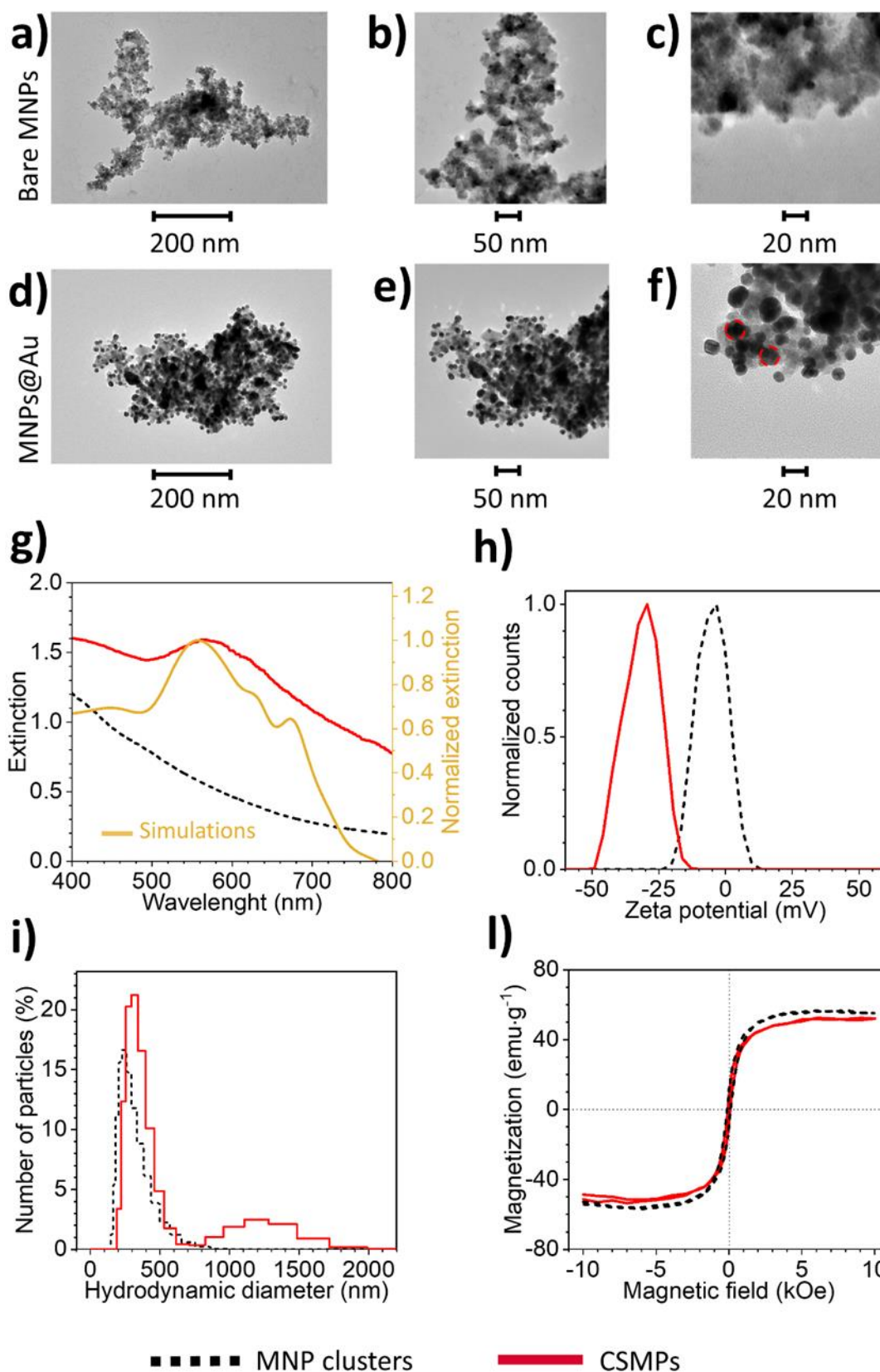


**Figure 4.13.** TEM micrographs at different magnification of MNP clusters as from stock (a), (b), (c) and CSMPs after the gold coating protocol (d), (e), (f). Due to the coating protocol, small AuNPs ( $\approx 20$  nm) stick to the surface of the bigger MNP clusters (diameter  $\approx 250$  nm). The images (a) and (d) depict single entire particles clusters while (b), (c), (e) and (f) highlight details at a greater magnification to show the AuNPs on the cluster surface. g) UV-Vis spectra of a solution containing MNP clusters as from stock (dashed black line) and a solution containing CSMPs (solid red line). The extinction peak ( $567 \pm 6$  nm) that appear after the coating protocol is due to the presence of gold on the surface of the MNP clusters. Simulations of the optical response by finite-difference time-domain (FDTD) method confirmed that the presence of AuNPs randomly distributed on the magnetic core with radius between 10 and 15 nm. h) Zeta potential distribution of bare MNP clusters (dashed black line) and CSMPs (solid red line) dispersed in aqueous solutions. The peaks of the distributions are -3 mV and -30 mV for MNP clusters and CSMPs, respectively. i) Size distributions from DLS measurements of a suspension of MNP clusters (dashed black line) and a suspension of CSMPs (solid red line). Due to the coating

protocol the unimodal distribution of the CSMPs turns into a bimodal distribution with a major and a minor mode. The major mode (average 350 nm and standard deviation 80 nm) constitutes about 90 % of the population and groups the signal of MNP clusters which have undergone an increase in the hydrodynamic diameter due to the presence of small AuNPs on the surface. The minor mode, on the other hand, represents aggregates of nanoparticles (about 1  $\mu\text{m}$  diameter) that are formed during the coating process as side effect. The aggregates were separated from the solution before carrying out biosensing experiments. l) Hysteresis loop of a solution containing MNP clusters as from the stock (black line) and CSMPs (red line) obtained with a vibrating-sample magnetometer (VSM). Data are normalized by total solid content, without removal of the gold contribution.

## 4.5 Biosensing application

### 4.5.1 Detection of Human IgG in simulated samples

The dose-response curve is reported in Figure 4.14a together with the best fit of the experimental data provided by a sigmoid curve:

$$\frac{\Delta V}{V} = a \frac{[x]}{[x] + b} + c \quad 4.3$$

where  $a = 4.1 \pm 0.4$ ,  $b = 145 \pm 70 \text{ ng}\cdot\text{mL}^{-1}$ ,  $c = 0.3 \pm 0.3$  are connected to the asymptotic value ( $a+c$ ), the concentration ( $[x]$ ) at which the frequency shift reaches the 50% of its maximal value ( $\approx b$ ) and the value obtained when the concentration is zero ( $c$ ). The dose-response curve exhibits signal saturation at concentrations higher than  $1 \mu\text{g}\cdot\text{mL}^{-1}$ , thus showing that the MR biochip in combination with CSMPs is able to provide a quantitative measurement over three decades. The error bars originate from a biological variability, each datapoint of the dose-response curve is the result of the average over 30 values from as many sensors in 2 different chips, 15 from the first experiment and 15 more from the duplicate.  $\Delta V \cdot V^{-1}$  were calculated for each positive sensor according to Paragraph 4.3.6. The standard deviation of the mean was considered as the statistical error on each of the two sets of 15 measurements whose propagation yielded the error of the datapoints in Figure 4.14a. The error related to the fluctuation of the experimental setup was negligible. Each experiment was performed with a different biochip obtaining coherent results. This is a strong confirmation of the robustness of the experimental setup with respect to fluctuations related to differences in the CSMPs solution and in the fabrication process of MR biochips. The limit of detection (LOD) was assessed by means of 3 standard deviation (SD) criteria calculating the concentration at which the dose-response curve assumes a value equal to the signal for the blank sample plus three standard deviation and turned up to be  $3.5 \text{ ng}\cdot\text{mL}^{-1}$  (23 pM).

### 4.5.2 Specificity assay

The specificity of the immunosensor was proved by assessing the detection of compounds similar to Human IgG by using the same experimental procedure. In this case it was measured the response of

the sensor to Mouse IgG, Goat anti-Human IgG and Rabbit anti-Chicken IGY and compared to the signals obtained for the blank and Human IgG samples. The experimental procedure was the same employed for the detection of Human IgG (Paragraph 4.3.6) as well as the statistical data analysis to determine the errors. Figure 4.14b shows the reliability of the immune response at low ( $10 \text{ ng}\cdot\text{mL}^{-1}$ ) and high concentrations ( $500 \text{ ng}\cdot\text{mL}^{-1}$ ) of the targets. As can be noticed the signal obtained with other Abs is compatible with blank and departs from what is obtained for the Human IgG. The good performance of the sensor in term of specificity are mainly a consequence of the biorecognition properties of the antibodies combined with the CSMPs low tendency to form non-specific bonds.

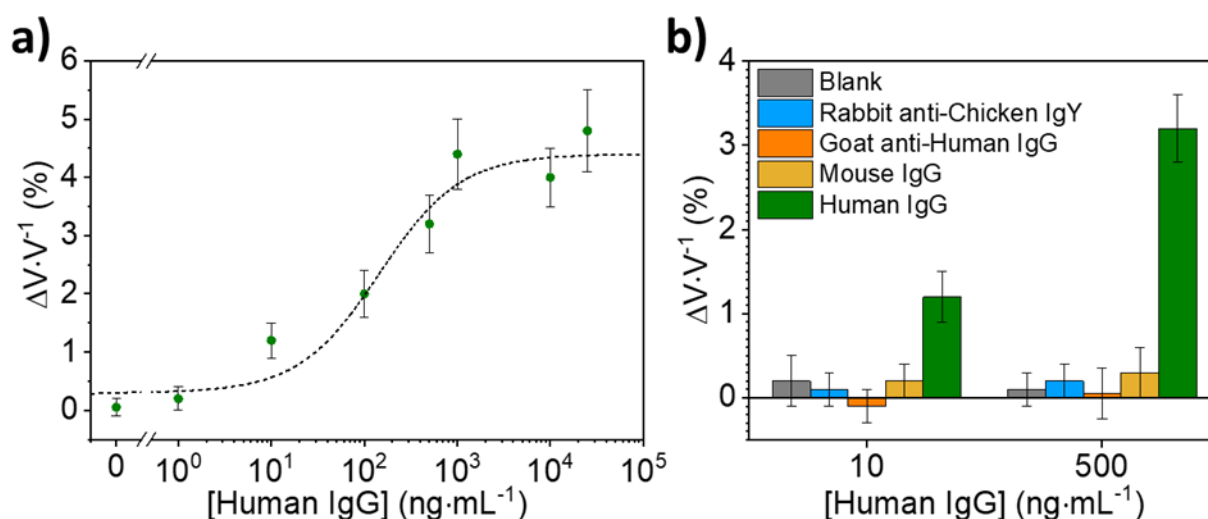


**Figure 4.14.** a) Dose–response curve, i.e., versus Human IgG concentrations ( $\text{ng}\cdot\text{mL}^{-1}$ ), the x axis scale is linear from 0 to  $1 \text{ ng}\cdot\text{mL}^{-1}$  and logarithmic from this value on. Experimental data are fitted by a sigmoid curve (Equation 1). Each data point was duplicated, the error bars were calculated as described in Section 2.6. The range of tested concentrations varies from the zero concentration to  $25 \mu\text{g}\cdot\text{mL}^{-1}$ . Each datapoint was duplicated, every experiment has been carried out using a different biochip. b) Sensor specificity. The sensor responds to compounds similar to Human IgG. As can be noticed the signal obtained with other Abs is compatible with blank and departs to what is obtained for the Human IgG. The experimental procedure was the same employed for the detection of Human IgG (Section 2.6) as well as the statistical data analysis to determine the errors.

## 4.6 Conclusions

Herein, we described an innovative platform composed of core@satellite magnetic particles as versatile substrate for an efficient biofunctionalization and the development of high sensitivity magneto resistive biosensors. The coating process was realized via chemical reduction of tetrachloroauric acid by means of sodium citrate so that the synthesized AuNPs (radius  $\approx 10\text{-}15 \text{ nm}$ ) self-assembled onto the outer surface of commercial MNP clusters (diameter  $\approx 250 \text{ nm}$ ). The CSMPs were deeply characterized, in particular the morphology, optical and magnetic response, hydrodynamic diameter and surface charge were compared with those exhibited by bare MNP clusters. We showed that CSMPs stability and ductility, along with magnetic responsiveness, were significantly improved thanks to the proposed approach. The results suggests that the satellite AuNPs

provided MNP clusters with convenient anchoring sites for biomolecules and higher chemical stability without resulting detrimental for core magnetic properties. Notably, while the surface charge demonstrated a significant improvement of the CSMPs stability, the magnetic saturation only suffered from a 9% reduction.

We implemented the CMSPs in an MR based biochip to realize a highly sensitive POC device. The MR biochip contained 6 sensing regions enclosed in a gold squared frame ( $300 \times 300 \mu\text{m}^2$ ) each one containing 5 U-shaped spin valve (SV) sensors ( $80 \times 2.6 \mu\text{m}^2$ ) coated with a gold layer ( $35 \times 13 \mu\text{m}^2$ ) for a total of 30 SV sensors. As a proof of concept, we demonstrated the feasibility of our platform to detect Human IgG in an interesting range for biomedical applications ( $1\text{-}1000 \text{ ng}\cdot\text{mL}^{-1}$ ). Additionally, multiplexed implementation (up to 6 different analytes at the same time) and signal redundancy (up to 30 measurements) are inherently ensured by the features of the MR detection platform.

The device showed quick response (within 1 hour) and excellent sensing performance with a LOD of  $3.5 \text{ ng}\cdot\text{mL}^{-1}$  (23 pM). As futuristic scope, the magnetic properties of CSMPs could be exploited for sample preconcentration in complex matrices before their interaction with the MR biochip. The versatility of our coating approach could be tested on different starting magnetic nanoparticles for tailored bioassays. Finally, the potential applications of the proposed biosensing platform are far-reaching for multi-analyte detection with high signal redundancy. Therefore, this kind of CSMPs would be very useful as a multifunctional substrate for detecting molecule analytes and target protein in the solution.

# Final remarks

The aim of the work in this thesis was to propose novel effective protocols for gold coating of commercial magnetic nanoparticles (MNPs) to improve the applicability of biosensors in environmental control, food safety and clinical analysis. A major objective of introducing gold decorated magnetic nanoparticles (MNPs@Au) was to improve the performance of widely spread-out biosensing setups, narrowing the gap in terms of performance with gold standard techniques.

The thesis has been divided into four chapters to gradually introduce the reader to the experiments. Each chapter opens with a description of the related theoretical framework and ends showing the obtained experimental results (except for Chapter 1 that is purely introductory). In particular, a specifically designed type of MNPs@Au was tested in combination with a sensor in each Chapter.

A magnetoelastic (ME) biosensor for wireless detection of analytes in liquid was proposed in Chapter 2. MNPs@Au, specifically designed for this type of application, were used for the first time in combination with a ME sensor in a new amplification protocol that significantly enhanced the sensitivity. The improvement in sensitivity was understood by modeling the interaction between the MNPs@Au and the ME sensor and comparing magnetic attraction to Brownian motion. Ultimately, the advantages of the magnetic core of the nanoparticles relies on their coupling with the local magnetic field, which in turn leads to an increase of the local density in proximity of the ribbon surface. Compared to standard configurations, both the magnetic sensitive platform and magnetic nanoparticles contributed to the measurement process for the first time. The superiority of MNPs@Au over the non-magnetic AuNPs, has been demonstrated by testing the ME biosensor against Human IgG in the range 0–20  $\mu\text{g}\cdot\text{mL}^{-1}$ . For futuristic purposes, in order to exploit their advantages fully, MNPs@Au could be used to purify the target from complex matrices before carrying out detection measurements with the ME sensor.

In Chapter 3 was described a colorimetric immunosensor for the detection of glyphosate in tap water. The most important novelty element was to use MNPs@Au instead of the more common AuNPs. The use of MNPs@Au made it possible to exploit at the same time the optical properties of the outer gold shell and the magnetic properties of the core. In particular, the outer shell was used for optical

sensing, by exploiting the local surface plasmon resonance (LSPR), as well as for efficient and fast functionalization by PIT. The magnetic core was exploited to trigger a micromixing mechanism, by means of external magnetic fields, that improved the MNPs@Au diffusion properties in the solution. Thanks to this innovation, the proposed colorimetric sensor was able to detect the glyphosate in concentration lower than the ones legally permitted in food according to several authorities. The performance of the proposed biosensor could be further improved deepening some aspects. For instance, a test campaign on different nanoparticle sizes and shapes can be conducted to optimize the presented micromixing mechanism and improve the sensitivity to a greater extent. Further studies could be conducted to investigate the sensing potentialities of such an approach in viscous, opalescent, and more complex matrices such as saliva to develop non-invasive point-of-care tests capable of dealing with the uncontrolled diffusion of endemic diseases.

The protocol for coating commercial MNP clusters with AuNPs introduced in Chapter 4 was meant to develop a multifunctional substrate for magneto resistive biosensors. The resulting core@satellite magnetic particles (CSMPs) consisted of isolated gold nanoparticles stuck onto an aggregate of individual iron oxide crystals (core). The complete characterization of the physical and chemical properties of CSMPs allowed to highlight all the advantages brought by the coating procedure. The CSMPs, flanked by a powerful magneto resistive (MR) biosensor, were used in the detected Human IgG in concentrations of clinical interest. Thanks to the gold decoration it was possible to apply the Photochemical Immobilization Technique by replacing obsolete, expensive, and time-consuming functionalization techniques. Despite the excellent result in terms of sensitivity and the simplifications in the experimental procedure, there are still several aspects that can be improved. In the first place, the biochip could be equipped with a magnetic circuit capable of focusing the nanoparticles near the sensitive regions, increasing both response times and sensitivity. Secondly, the conformation of CSMPs could be explored in more depth, testing different magnetic cores on the market, and changing the conformation of the AuNPs on the surface by modifying the parameters of the coating protocol.

In conclusion, all types of gold decorated magnetic nanoparticles introduced in this work brought improvements to the biosensor with which they were combined. The multiplicity of ways in which MNPs@Au can be used allows for more creative and efficient ways to revisit established biosensing schemes.

# References

- [1] L.C. Clark, C. Lyons, Electrode Systems for Continuous Monitoring in Cardiovascular Surgery, *Ann. N. Y. Acad. Sci.* 102 (1962) 29–45. <https://doi.org/10.1111/j.1749-6632.1962.tb13623.x>.
- [2] T. Lavecchia, A. Tibuzzi, M.T. Giardi, Biosensors for functional food safety and analysis, in: *Adv. Exp. Med. Biol.*, Springer US, Boston, MA, 2010: pp. 267–281. [https://doi.org/10.1007/978-1-4419-7347-4\\_20](https://doi.org/10.1007/978-1-4419-7347-4_20).
- [3] C.I.L. Justino, A.C. Duarte, T.A.P. Rocha-Santos, Recent progress in biosensors for environmental monitoring: A review, *Sensors*. 17 (2017) 2918. <https://doi.org/10.3390/s17122918>.
- [4] M. Oliverio, S. Perotto, G.C. Messina, L. Lovato, F. De Angelis, Chemical Functionalization of Plasmonic Surface Biosensors: A Tutorial Review on Issues, Strategies, and Costs, *ACS Appl. Mater. Interfaces*. 9 (2017) 29394–29411. <https://doi.org/10.1021/acsami.7b01583>.
- [5] N. Bhalla, Y. Pan, Z. Yang, A.F. Payam, Opportunities and Challenges for Biosensors and Nanoscale Analytical Tools for Pandemics: COVID-19, *ACS Nano*. 14 (2020) 7783–7807. <https://doi.org/10.1021/acsnano.0c04421>.
- [6] P. Guardia, A. Labarta, X. Batlle, Tuning the size, the shape, and the magnetic properties of iron oxide nanoparticles, *J. Phys. Chem. C*. 115 (2011) 390–396. <https://doi.org/10.1021/jp1084982>.
- [7] A.G. Kolhatkar, A.C. Jamison, D. Litvinov, R.C. Willson, T.R. Lee, Tuning the magnetic properties of nanoparticles, 2013. <https://doi.org/10.3390/ijms140815977>.
- [8] V. Nabaei, R. Chandrawati, H. Heidari, Magnetic biosensors: Modelling and simulation, *Biosens. Bioelectron.* 103 (2018) 69–86. <https://doi.org/10.1016/j.bios.2017.12.023>.
- [9] M. Hasanzadeh, N. Shadjou, M. de la Guardia, Iron and iron-oxide magnetic nanoparticles as signal-amplification elements in electrochemical biosensing, *TrAC - Trends Anal. Chem.* 72 (2015) 1–9. <https://doi.org/10.1016/j.trac.2015.03.016>.
- [10] A.H.C. Ng, R. Fobel, C. Fobel, J. Lamanna, D.G. Rackus, A. Summers, C. Dixon, M.D.M. Dryden, C. Lam, M. Ho, N.S. Mufti, V. Lee, M.A.M. Asri, E.A. Sykes, M.D. Chamberlain, R. Joseph, M. Ope, H.M. Scobie, A. Knipes, P.A. Rota, N. Marano, P.M. Chege, M. Njuguna, R. Nzunza, N. Kisangau, J. Kiogora, M. Karuingi, J.W. Burton, P. Borus, E. Lam, A.R. Wheeler, A digital microfluidic system for serological immunoassays in remote settings, *Sci. Transl. Med.* 10 (2018) eaar6076. <https://doi.org/10.1126/scitranslmed.aar6076>.
- [11] A.K. Gupta, M. Gupta, Synthesis and surface engineering of iron oxide nanoparticles for biomedical applications, *Biomaterials*. 26 (2005) 3995–4021.

<https://doi.org/10.1016/j.biomaterials.2004.10.012>.

- [12] J.J. Gooding, S. Ciampi, The molecular level modification of surfaces: From self-assembled monolayers to complex molecular assemblies, *Chem. Soc. Rev.* 40 (2011) 2704–2718. <https://doi.org/10.1039/c0cs00139b>.
- [13] K. Saha, S.S. Agasti, C. Kim, X. Li, V.M. Rotello, Gold nanoparticles in chemical and biological sensing, *Chem. Rev.* 112 (2012) 2739–2779. <https://doi.org/10.1021/cr2001178>.
- [14] A. Minopoli, N. Sakač, B. Lenyk, R. Campanile, D. Mayer, A. Offenhäusser, R. Velotta, B. Della Ventura, LSPR-based colorimetric immunosensor for rapid and sensitive 17 $\beta$ -estradiol detection in tap water, *Sensors Actuators, B Chem.* 308 (2020). <https://doi.org/10.1016/j.snb.2020.127699>.
- [15] K. Loza, J. Diendorf, C. Sengstock, L. Ruiz-Gonzalez, J.M. Gonzalez-Calbet, M. Vallet-Regi, M. Köller, M. Epple, The dissolution and biological effects of silver nanoparticles in biological media, *J. Mater. Chem. B.* 2 (2014) 1634–1643. <https://doi.org/10.1039/c3tb21569e>.
- [16] A. Chaudhary, S. Khan, A. Gupta, C.K. Nandi, Effect of surface chemistry and morphology of gold nanoparticle on the structure and activity of common blood proteins, *New J. Chem.* 40 (2016) 4879–4883. <https://doi.org/10.1039/c5nj03720d>.
- [17] M.A. Dheyab, A.A. Aziz, M.S. Jameel, P.M. Khaniabadi, Recent advances in synthesis, medical applications and challenges for gold-coated iron oxide: Comprehensive study, *Nanomaterials.* 11 (2021) 1–16. <https://doi.org/10.3390/nano11082147>.
- [18] B.D. Malhotra, R. Singhal, A. Chaubey, S.K. Sharma, A. Kumar, Recent trends in biosensors, *Curr. Appl. Phys.* 5 (2005) 92–97. <https://doi.org/10.1016/j.cap.2004.06.021>.
- [19] C.A. Grimes, S.C. Roy, S. Rani, Q. Cai, Theory, instrumentation and applications of magnetoelastic resonance sensors: A review, *Sensors.* 11 (2011) 2809–2844. <https://doi.org/10.3390/s110302809>.
- [20] R. Campanile, E. Scardapane, A. Forente, C. Granata, R. Germano, R. Di Girolamo, A. Minopoli, R. Velotta, B. Della Ventura, V. Iannotti, Core-shell magnetic nanoparticles for highly sensitive magnetoelastic immunosensor, *Nanomaterials.* 10 (2020) 1–18. <https://doi.org/10.3390/nano10081526>.
- [21] S.K. Ghosh, T. Pal, Interparticle coupling effect on the surface plasmon resonance of gold nanoparticles: From theory to applications, *Chem. Rev.* 107 (2007) 4797–4862. <https://doi.org/10.1021/cr0680282>.
- [22] K.M. Mayer, J.H. Hafner, Localized surface plasmon resonance sensors, *Chem. Rev.* 111 (2011) 3828–3857. <https://doi.org/10.1021/cr100313v>.
- [23] M.M. Miller, A.A. Lazarides, Sensitivity of metal nanoparticle surface plasmon resonance to

- the dielectric environment, *J. Phys. Chem. B.* 109 (2005) 21556–21565. <https://doi.org/10.1021/jp054227y>.
- [24] K.S. Lee, M.A. El-Sayed, Gold and silver nanoparticles in sensing and imaging: Sensitivity of plasmon response to size, shape, and metal composition, *J. Phys. Chem. B.* 110 (2006) 19220–19225. <https://doi.org/10.1021/jp062536y>.
- [25] A. Minopoli, Plasmonic nanostructures for optical biosensing, University of Naples Federico II, 2020.
- [26] P.N. Njoki, I.-I.S. Lim, D. Mott, H.-Y. Park, B. Khan, S. Mishra, R. Sujakumar, J. Luo, C.-J. Zhong, Size Correlation of Optical and Spectroscopic Properties for Gold Nanoparticles, *J. Phys. Chem. C.* 111 (2007) 14664–14669. <https://doi.org/10.1021/jp074902z>.
- [27] M. Iarossi, C. Schiattarella, I. Rea, L. De Stefano, R. Fittipaldi, A. Vecchione, R. Velotta, B. Della Ventura, Colorimetric Immunosensor by Aggregation of Photochemically Functionalized Gold Nanoparticles, *ACS Omega.* 3 (2018) 3805–3812. <https://doi.org/10.1021/acsomega.8b00265>.
- [28] A. Minopoli, N. Sakač, B. Lenyk, R. Campanile, D. Mayer, A. Offenhäusser, R. Velotta, B. Della Ventura, LSPR-based colorimetric immunosensor for rapid and sensitive 17 $\beta$ -estradiol detection in tap water, *Sensors Actuators, B Chem.* 308 (2020) 127699. <https://doi.org/10.1016/j.snb.2020.127699>.
- [29] S. Megarajan, A. Veerappan, A selective pink-to-purple colorimetric sensor for aluminium via the aggregation of gold nanoparticles, *Opt. Mater. (Amst).* 108 (2020) 110177. <https://doi.org/10.1016/j.optmat.2020.110177>.
- [30] H. Li, L. Rothberg, Colorimetric detection of DNA sequences based on electrostatic interactions with unmodified gold nanoparticles, *Proc. Natl. Acad. Sci. U. S. A.* 101 (2004) 14036–14039. <https://doi.org/10.1073/pnas.0406115101>.
- [31] B. Della Ventura, M. Cennamo, A. Minopoli, R. Campanile, S.B. Censi, D. Terracciano, G. Portella, R. Velotta, Colorimetric test for fast detection of SARS-COV-2 in nasal and throat swabs, *ACS Sensors.* 5 (2020) 3043–3048. <https://doi.org/10.1021/acssensors.0c01742>.
- [32] A. Makarov, T. Windbacher, V. Sverdlov, S. Selberherr, CMOS-compatible spintronic devices: A review, *Semicond. Sci. Technol.* 31 (2016) 113006. <https://doi.org/10.1088/0268-1242/31/11/113006>.
- [33] C.H. Tsang, R.E. Fontana, T. Lin, D.E. Heim, B.A. Gurney, M.L. Williams, Design, fabrication, and performance of spin-valve read heads for magnetic recording applications, *IBM J. Res. Dev.* 42 (1998) 103–115. <https://doi.org/10.1147/rd.421.0103>.
- [34] C.C. Huang, C.L. Lin, J.J. Kao, J.J. Chang, G.J. Sheu, Vehicle Parking Guidance for Wireless Charge Using GMR Sensors, *IEEE Trans. Veh. Technol.* 67 (2018) 6882–6894.

<https://doi.org/10.1109/TVT.2018.2827069>.

- [35] N.K. Bhaskarrao, A.C. Sreekantan, P.K. Dutta, Analysis of a Linearizing Direct Digitizer With Phase-Error Compensation for TMR Angular Position Sensor, *IEEE Trans. Instrum. Meas.* 67 (2018) 1795–1803. <https://doi.org/10.1109/TIM.2018.2810698>.
- [36] U.P. Borole, S. Subramaniam, I.R. Kulkarni, P. Saravanan, H.C. Barshilia, P. Chowdhury, Highly sensitive giant magnetoresistance (GMR) based ultra low differential pressure sensor, *Sensors Actuators, A Phys.* 280 (2018) 125–131. <https://doi.org/10.1016/j.sna.2018.07.022>.
- [37] J.J. Park, K.S.M. Reddy, B. Stadler, A. Flatau, Magnetostrictive Fe-Ga/Cu Nanowires Array With GMR Sensor for Sensing Applied Pressure, *IEEE Sens. J.* 17 (2017) 2015–2020. <https://doi.org/10.1109/JSEN.2017.2657789>.
- [38] D.R. Baselt, G.U. Lee, M. Natesan, S.W. Metzger, P.E. Sheehan, R.J. Colton, A biosensor based on magnetoresistance technology, *Biosens. Bioelectron.* 13 (1998) 731–739. [https://doi.org/10.1016/S0956-5663\(98\)00037-2](https://doi.org/10.1016/S0956-5663(98)00037-2).
- [39] I. Giouroudi, E. Hristoforou, Perspective: Magnetoresistive sensors for biomedicine, *J. Appl. Phys.* 124 (2018). <https://doi.org/10.1063/1.5027035>.
- [40] T. Klein, W. Wang, L. Yu, K. Wu, K.L.M. Boylan, R.I. Vogel, A.P.N. Skubitz, J.P. Wang, Development of a multiplexed giant magnetoresistive biosensor array prototype to quantify ovarian cancer biomarkers, *Biosens. Bioelectron.* 126 (2019) 301–307. <https://doi.org/10.1016/j.bios.2018.10.046>.
- [41] J. Choi, A.W. Gani, D.J.B. Bechstein, J.R. Lee, P.J. Utz, S.X. Wang, Portable, one-step, and rapid GMR biosensor platform with smartphone interface, *Biosens. Bioelectron.* 85 (2016) 1–7. <https://doi.org/10.1016/j.bios.2016.04.046>.
- [42] D. Su, K. Wu, V.D. Krishna, T. Klein, J. Liu, Y. Feng, A.M. Perez, M.C.J. Cheeran, J.P. Wang, Detection of influenza A virus in swine nasal swab samples with a wash-free magnetic bioassay and a handheld giant magnetoresistance sensing system, *Front. Microbiol.* 10 (2019) 1077. <https://doi.org/10.3389/fmicb.2019.01077>.
- [43] N.G. Welch, J.A. Scoble, B.W. Muir, P.J. Pigram, Orientation and characterization of immobilized antibodies for improved immunoassays (Review), *Biointerphases.* 12 (2017) 02D301. <https://doi.org/10.1116/1.4978435>.
- [44] B. Della Ventura, M. Banchelli, R. Funari, A. Illiano, M. De Angelis, P. Taroni, A. Amoresano, P. Matteini, R. Velotta, Biosensor surface functionalization by a simple photochemical immobilization of antibodies: Experimental characterization by mass spectrometry and surface enhanced Raman spectroscopy, *Analyst.* 144 (2019) 6871–6880. <https://doi.org/10.1039/c9an00443b>.
- [45] M. Cimafonte, QCM and EIS Immunosensors for applications to food safety and quality,

University of Naples Federico II, 2019.

- [46] M. van der Veen, M.C. Stuart, W. Norde, Spreading of proteins and its effect on adsorption and desorption kinetics, *Colloids Surfaces B Biointerfaces*. 54 (2007) 136–142. <https://doi.org/10.1016/j.colsurfb.2006.08.017>.
- [47] M. Rabe, D. Verdes, S. Seeger, Understanding protein adsorption phenomena at solid surfaces, *Adv. Colloid Interface Sci.* 162 (2011) 87–106. <https://doi.org/10.1016/j.cis.2010.12.007>.
- [48] S. Sharma, H. Byrne, R.J.O. Kennedy, Antibodies and antibody-derived analytical biosensors, *Essays Biochem.* (2016) 9–18. <https://doi.org/10.1042/EBC20150002>.
- [49] H. Um, M. Kim, S. Lee, J. Min, H. Kim, Y. Choi, Y. Kim, Electrochemically oriented immobilization of antibody on poly-(2-cyano-ethylpyrrole)-coated gold electrode using a cyclic voltammetry, *Talanta*. 84 (2011) 330–334. <https://doi.org/10.1016/j.talanta.2011.01.013>.
- [50] A.C. Barton, S.D. Collyer, F. Davis, G. Garifallou, G. Tsekenis, E. Tully, R. O’Kennedy, T. Gibson, P.A. Millner, S.P.J. Higson, Labelless AC impedimetric antibody-based sensors with pgml–1 sensitivities for point-of-care biomedical applications, *Biosens. Bioelectron.* 24 (2009) 1090–1095. <https://doi.org/10.1016/j.bios.2008.06.001>.
- [51] O. Ouerghi, A. Touhami, N. Jaffrezic-renault, C. Martelet, H. Ben Ouada, S. Cosnier, Impedimetric immunosensor using avidin – biotin for antibody immobilization, *Bioelectrochemistry*. 56 (2002) 131–133.
- [52] J.E. Lee, J.H. Seo, C.S. Kim, Y. Kwon, J.H. Ha, S.S. Choi, H.J. Cha, A comparative study on antibody immobilization strategies onto solid surface, *Korean J. Chem. Eng.* 30 (2013) 1934–1938. <https://doi.org/10.1007/s11814-013-0117-5>.
- [53] M.S. Inkpen, Z. Liu, H. Li, L.M. Campos, J.B. Neaton, L. Venkataraman, Non-chemisorbed gold–sulfur binding prevails in self-assembled monolayers, *Nat. Chem.* 11 (2019) 351–358. <https://doi.org/10.1038/s41557-019-0216-y>.
- [54] M. Sharafeldin, K. McCaffrey, J.F. Rusling, Influence of antibody immobilization strategy on carbon electrode immunoarrays, *Analyst*. 144 (2019) 5108–5116. <https://doi.org/10.1039/C9AN01093A>.
- [55] J.M. Fowler, M.C. Stuart, D.K.Y. Wong, Self-Assembled Layer of Thiolated Protein G as an Immunosensor Scaffold, *Anal. Chem.* 79 (2007) 350–354. <https://doi.org/10.1021/ac061175f>.
- [56] K. Icoz, M.C. Soylu, Z. Canikara, E. Unal, Quartz-crystal Microbalance Measurements of CD19 Antibody Immobilization on Gold Surface and Capturing B Lymphoblast Cells: Effect of Surface Functionalization, *Electroanalysis*. 30 (2018) 834–841. <https://doi.org/10.1002/elan.201700789>.

- [57] D. Mandler, S. Kraus-Ophir, Self-assembled monolayers (SAMs) for electrochemical sensing, *J. Solid State Electrochem.* 15 (2011) 1535–1558. <https://doi.org/10.1007/s10008-011-1493-6>.
- [58] N.K. Chaki, K. Vijayamohanan, Self-assembled monolayers as a tunable platform for biosensor applications, *Biosens. Bioelectron.* 17 (2002) 1–12. [https://doi.org/10.1016/S0956-5663\(01\)00277-9](https://doi.org/10.1016/S0956-5663(01)00277-9).
- [59] A.D. Chowdhury, A. De, C.R. Chaudhuri, K. Bandyopadhyay, P. Sen, Label free polyaniline based impedimetric biosensor for detection of *E. coli* O157:H7 Bacteria, *Sensors Actuators, B Chem.* 171–172 (2012) 916–923. <https://doi.org/10.1016/j.snb.2012.06.004>.
- [60] C. Vericat, M.E. Vela, G. Benitez, P. Carro, R.C. Salvarezza, Self-assembled monolayers of thiols and dithiols on gold: new challenges for a well-known system, *Chem. Soc. Rev.* 39 (2010) 1805–1834. <https://doi.org/10.1039/b907301a>.
- [61] C.Y. Lee, H.E. Canavan, L.J. Gamble, D.G. Castner, Evidence of impurities in thiolated single-stranded DNA oligomers and their effect on DNA self-assembly on gold, *Langmuir.* 21 (2005) 5134–5141. <https://doi.org/10.1021/la0472302>.
- [62] A. Butterworth, E. Blues, P. Williamson, M. Cardona, L. Gray, D.K. Corrigan, SAM composition and electrode roughness affect performance of a DNA biosensor for antibiotic resistance, *Biosensors.* 9 (2019). <https://doi.org/10.3390/bios9010022>.
- [63] B. Della Ventura, L. Schiavo, C. Altucci, R. Esposito, R. Velotta, Light assisted antibody immobilization for bio-sensing, *Biomed. Opt. Express.* 2 (2011) 3223. <https://doi.org/10.1364/boe.2.003223>.
- [64] R. Funari, B. Della Ventura, C. Altucci, A. Offenhäusser, D. Mayer, R. Velotta, Single Molecule Characterization of UV-Activated Antibodies on Gold by Atomic Force Microscopy, *Langmuir.* 32 (2016) 8084–8091. <https://doi.org/10.1021/acs.langmuir.6b02218>.
- [65] B. Della Ventura, M. Banchelli, R. Funari, A. Illiano, M. De Angelis, P. Taroni, A. Amoresano, P. Matteini, R. Velotta, Biosensor surface functionalization by a simple photochemical immobilization of antibodies: experimental characterization by mass spectrometry and surface enhanced Raman spectroscopy, *Analyst.* 144 (2019) 6871–6880. <https://doi.org/10.1039/C9AN00443B>.
- [66] M.T. Neves-Petersen, Z. Gryczynski, J. Lakowicz, P. Fojan, S. Pedersen, E. Petersen, S. Bjørn Petersen, High probability of disrupting a disulphide bridge mediated by an endogenous excited tryptophan residue, *Protein Sci.* 11 (2009) 588–600. <https://doi.org/10.1110/ps.06002>.
- [67] G.L. Ellman, Tissue Sulfyd Groups, *Arch. Biochem. Biophys.* (1959) 70–77.
- [68] R. Funari, B. Della Ventura, R. Carrieri, L. Morra, E. Lahoz, F. Gesuele, C. Altucci, R. Velotta, Detection of parathion and patulin by quartz-crystal microbalance functionalized by the

photonics immobilization technique, *Biosens. Bioelectron.* 67 (2015) 224–229. <https://doi.org/10.1016/j.bios.2014.08.020>.

- [69] R. Funari, B. Della Ventura, L. Schiavo, R. Esposito, C. Altucci, R. Velotta, Detection of parathion pesticide by quartz crystal microbalance functionalized with UV-activated antibodies, *Anal. Chem.* 85 (2013) 6392–6397. <https://doi.org/10.1021/ac400852c>.
- [70] B. Della Ventura, N. Sakač, R. Funari, R. Velotta, Flexible immunosensor for the detection of salivary  $\alpha$ -amylase in body fluids, *Talanta*. 174 (2017) 52–58. <https://doi.org/10.1016/j.talanta.2017.05.075>.
- [71] R. Funari, I. Terracciano, B. Della Ventura, S. Ricci, T. Cardi, N. D’Agostino, R. Velotta, Label-Free Detection of Gliadin in Food by Quartz Crystal Microbalance-Based Immunosensor, *J. Agric. Food Chem.* 65 (2017) 1281–1289. <https://doi.org/10.1021/acs.jafc.6b04830>.
- [72] B. Della Ventura, M. Cennamo, A. Minopoli, R. Campanile, S. Bolletti Censi, D. Terracciano, G. Portella, R. Velotta, Colorimetric Test for Fast Detection of SARS-CoV-2 in Nasal and Throat Swabs, *ACS Sensors*. 5 (2020) 3043–3048. <https://doi.org/10.1021/acssensors.0c01742>.
- [73] B. Della Ventura, M. Iannaccone, R. Funari, M.P. Ciamarra, C. Altucci, R. Capparelli, S. Roperto, R. Velotta, Effective antibodies immobilization and functionalized nanoparticles in a quartzcrystal microbalance-based immunosensor for the detection of parathion, *PLoS One*. 12 (2017). <https://doi.org/10.1371/journal.pone.0171754>.
- [74] P. Uebel, S.T. Bauerschmidt, M.A. Schmidt, P. St.j. Russell, A gold-nanotip optical fiber for plasmon-enhanced near-field detection, *Appl. Phys. Lett.* 103 (2013) 21101. <https://doi.org/10.1063/1.4813115>.
- [75] S.K. Patel, C. Argyropoulos, Plasmonic nanoantennas: Enhancing light-matter interactions at the nanoscale, *EPJ Appl. Metamaterials*. 2 (2015) 4. <https://doi.org/10.1051/epjam/2015006>.
- [76] A. V. Kabashin, P. Evans, S. Pastkovsky, W. Hendren, G.A. Wurtz, R. Atkinson, R. Pollard, V.A. Podolskiy, A. V. Zayats, Plasmonic nanorod metamaterials for biosensing, *Nat. Mater.* 8 (2009) 867–871. <https://doi.org/10.1038/nmat2546>.
- [77] S.H. Kim, S.M. Sharker, H. Lee, I. In, K.D. Lee, S.Y. Park, Photothermal conversion upon near-infrared irradiation of fluorescent carbon nanoparticles formed from carbonized polydopamine, *RSC Adv.* 6 (2016) 61482–61491. <https://doi.org/10.1039/c6ra08196g>.
- [78] J. Liu, W. Bai, S. Niu, C. Zhu, S. Yang, A. Chen, Highly sensitive colorimetric detection of 17 $\beta$ -estradiol using split DNA aptamers immobilized on unmodified gold nanoparticles, *Sci. Rep.* 4 (2014) 7571. <https://doi.org/10.1038/srep07571>.
- [79] O.A. Alsager, S. Kumar, B. Zhu, J. Travas-Sejdic, K.P. McNatty, J.M. Hodgkiss,

- Ultrasensitive colorimetric detection of 17-estradiol: The effect of shortening dna aptamer sequences, *Anal. Chem.* 87 (2015) 4201–4209. <https://doi.org/10.1021/acs.analchem.5b00335>.
- [80] R. Wang, H. Chon, S. Lee, Z. Cheng, S.H. Hong, Y.H. Yoon, J. Choo, Highly Sensitive Detection of Hormone Estradiol E2 Using Surface-Enhanced Raman Scattering Based Immunoassays for the Clinical Diagnosis of Precocious Puberty, *ACS Appl. Mater. Interfaces.* 8 (2016) 10665–10672. <https://doi.org/10.1021/acsami.5b10996>.
- [81] R. Shukla, V. Bansal, M. Chaudhary, A. Basu, R.R. Bhonde, M. Sastry, Biocompatibility of gold nanoparticles and their endocytotic fate inside the cellular compartment: A microscopic overview, *Langmuir.* 21 (2005) 10644–10654. <https://doi.org/10.1021/la0513712>.
- [82] X. Zhang, Gold Nanoparticles: Recent Advances in the Biomedical Applications, *Cell Biochem. Biophys.* 72 (2015) 771–775. <https://doi.org/10.1007/s12013-015-0529-4>.
- [83] E. Katz, Magnetic Nanoparticles, *Magnetochemistry.* 6 (2020) 6. <https://doi.org/10.3390/magnetochemistry6010006>.
- [84] D. Xiao, T. Lu, R. Zeng, Y. Bi, Preparation and highlighted applications of magnetic microparticles and nanoparticles: a review on recent advances, *Microchim. Acta.* 183 (2016) 2655–2675. <https://doi.org/10.1007/s00604-016-1928-y>.
- [85] A. Ahmadi, H. Shirazi, N. Pourbagher, A. Akbarzadeh, K. Omidfar, An electrochemical immunosensor for digoxin using core-shell gold coated magnetic nanoparticles as labels, *Mol. Biol. Rep.* 41 (2014) 1659–1668. <https://doi.org/10.1007/s11033-013-3014-4>.
- [86] R. Rawal, S. Chawla, C.S. Pundir, An electrochemical sulfite biosensor based on gold coated magnetic nanoparticles modified gold electrode, *Biosens. Bioelectron.* 31 (2012) 144–150. <https://doi.org/10.1016/j.bios.2011.10.007>.
- [87] T. Ahmad, H. Bae, I. Rhee, Y. Chang, S.U. Jin, S. Hong, Gold-coated iron oxide nanoparticles as a T2 agent in magnetic resonance imaging, *J. Nanosci. Nanotechnol.* 12 (2012) 5132–5137. <https://doi.org/10.1166/jnn.2012.6368>.
- [88] S. Kayal, R.V. Ramanujan, Anti-cancer drug loaded iron-gold core-shell nanoparticles (Fe@Au) for magnetic drug targeting, *J. Nanosci. Nanotechnol.* 10 (2010) 5527–5539. <https://doi.org/10.1166/jnn.2010.2461>.
- [89] K.C.F. Leung, S. Xuan, X. Zhu, D. Wang, C.P. Chak, S.F. Lee, W.K.W. Ho, B.C.T. Chung, Gold and iron oxide hybrid nanocomposite materials, *Chem. Soc. Rev.* 41 (2012) 1911–1928. <https://doi.org/10.1039/c1cs15213k>.
- [90] D.R. Baselt, G.U. Lee, M. Natesan, S.W. Metzger, P.E. Sheehan, R.J. Colton, A biosensor based on magnetoresistance technology, *Biosens. Bioelectron.* 13 (1998) 731–739. [https://doi.org/10.1016/S0956-5663\(98\)00037-2](https://doi.org/10.1016/S0956-5663(98)00037-2).

- [91] T. Uchiyama, S. Nakayama, K. Mohri, K. Bushida, Biomagnetic field detection using very high sensitivity magnetoimpedance sensors for medical applications, *Phys. Status Solidi*. 206 (2009) 639–643. <https://doi.org/10.1002/pssa.200881251>.
- [92] V.C. Romao, S.A.M. Martins, J. Germano, F.A. Cardoso, S. Cardoso, P.P. Freitas, Lab-on-Chip Devices: Gaining Ground Losing Size, *ACS Nano*. 11 (2017) 10659–10664. <https://doi.org/10.1021/acsnano.7b06703>.
- [93] K. Zhang, L. Fu, L. Zhang, Z. Cheng, T. Huang, Magnetostrictive particle based biosensors for in situ and real-time detection of pathogens in water, *Biotechnol. Bioeng.* 111 (2014) 2229–2238. <https://doi.org/10.1002/bit.25279>.
- [94] X. Guo, J. Wang, Y. Zhao, R. Liu, Q. Zhang, Z. Yuan, S. Sang, A wireless magnetoelastic DNA-biosensor amplified by AuNPs for the detection of a common mutated DNA causing  $\beta$ -thalassaemia, *Biochem. Eng. J.* 156 (2020) 107498. <https://doi.org/10.1016/j.bej.2020.107498>.
- [95] P. G. Saiz, D. Gandia, A. Lasheras, A. Sagasti, I. Quintana, M.L. Fdez-Gubieda, J. Gutiérrez, M.I. Arriortua, A.C. Lopes, Enhanced mass sensitivity in novel magnetoelastic resonators geometries for advanced detection systems, *Sensors Actuators, B Chem.* 296 (2019). <https://doi.org/10.1016/j.snb.2019.05.089>.
- [96] M.L. Johnson, O. LeVar, S.H. Yoon, J.H. Park, S. Huang, D.J. Kim, Z. Cheng, B.A. Chin, Dual-cathode method for sputtering magnetoelastic iron-boron films, *Vacuum*. 83 (2009) 958–964. <https://doi.org/10.1016/j.vacuum.2008.11.004>.
- [97] Katz, Synthesis, Properties and Applications of Magnetic Nanoparticles and Nanowires—A Brief Introduction, *Magnetochemistry*. 5 (2019) 61. <https://doi.org/10.3390/magnetochemistry5040061>.
- [98] P. Taylor, P. Majewski, B. Thierry, Critical Reviews in Solid State and Materials Sciences Functionalized Magnetite Nanoparticles — Synthesis , Properties , and Bio-Applications Functionalized Magnetite Nanoparticles — Synthesis , Properties , and Bio-Applications, *Small*. 8436 (2007) 37–41. <https://doi.org/10.1080/10408430701776680>.
- [99] M.M. Barsan, T.A. Enache, N. Preda, G. Stan, N.G. Apostol, E. Matei, A. Kuncser, V.C. Diculescu, Direct Immobilization of Biomolecules through Magnetic Forces on Ni Electrodes via Ni Nanoparticles: Applications in Electrochemical Biosensors, *ACS Appl. Mater. Interfaces*. 11 (2019) 19867–19877. <https://doi.org/10.1021/acsami.9b04990>.
- [100] K.S. Kim, J.K. Park, Magnetic force-based multiplexed immunoassay using superparamagnetic nanoparticles in microfluidic channel, *Lab Chip*. 5 (2005) 657–664. <https://doi.org/10.1039/b502225h>.
- [101] C. Duarte, T. Costa, C. Carneiro, R. Soares, A. Jitariu, S. Cardoso, M. Piedade, R. Bexiga, P. Freitas, Semi-quantitative method for streptococci magnetic detection in raw milk, *Biosensors*.

6 (2016) 1–14. <https://doi.org/10.3390/bios6020019>.

- [102] R. Soares, V.C. Martins, R. Macedo, F.A. Cardoso, S.A.M. Martins, D.M. Caetano, P.H. Fonseca, V. Silvério, S. Cardoso, P.P. Freitas, Go with the flow: advances and trends in magnetic flow cytometry, *Anal. Bioanal. Chem.* 411 (2019) 1839–1862. <https://doi.org/10.1007/s00216-019-01593-9>.
- [103] F.A. Blyakhman, S.Y. Sokolov, A.P. Safronov, O.A. Dinislamova, T.F. Shklyar, A.Y. Zubarev, G. V. Kurlyandskaya, Ferrogels Ultrasonography for Biomedical Applications, *Sensors*. 19 (2019) 3959. <https://doi.org/10.3390/s19183959>.
- [104] F. Blyakhman, N. Buznikov, T. Sklyar, A. Safronov, E. Golubeva, A. Svalov, S. Sokolov, G. Melnikov, I. Orue, G. Kurlyandskaya, Mechanical, Electrical and Magnetic Properties of Ferrogels with Embedded Iron Oxide Nanoparticles Obtained by Laser Target Evaporation: Focus on Multifunctional Biosensor Applications, *Sensors*. 18 (2018) 872. <https://doi.org/10.3390/s18030872>.
- [105] C. Grimes, C. Mungle, K. Zeng, M. Jain, W. Dreschel, M. Paulose, K. Ong, Wireless Magnetoelastic Resonance Sensors: A Critical Review, *Sensors*. 2 (2002) 294–313. <https://doi.org/10.3390/s20700294>.
- [106] A. García-Arribas, J. Gutiérrez, G. Kurlyandskaya, J. Barandiarán, A. Svalov, E. Fernández, A. Lasheras, D. de Cos, I. Bravo-Imaz, Sensor Applications of Soft Magnetic Materials Based on Magneto-Impedance, Magneto-Elastic Resonance and Magneto-Electricity, *Sensors*. 14 (2014) 7602–7624. <https://doi.org/10.3390/s140507602>.
- [107] M. Cimafonte, A. Fulgione, R. Gaglione, M. Papaianni, R. Capparelli, A. Arciello, S.B. Censi, G. Borriello, R. Velotta, B. Della Ventura, Screen printed based impedimetric immunosensor for rapid detection of *Escherichia coli* in drinking water, *Sensors (Switzerland)*. 20 (2020) 1–17. <https://doi.org/10.3390/s20010274>.
- [108] B. Della Ventura, M. Gelzo, E. Battista, A. Alabastri, A. Schirato, G. Castaldo, G. Corso, F. Gentile, R. Velotta, Biosensor for Point-of-Care Analysis of Immunoglobulins in Urine by Metal Enhanced Fluorescence from Gold Nanoparticles, *ACS Appl. Mater. Interfaces*. 11 (2019) 3753–3762. <https://doi.org/10.1021/acsami.8b20501>.
- [109] A. Fulgione, M. Cimafonte, B. Della Ventura, M. Iannaccone, C. Ambrosino, F. Capuano, Y.T.R. Proroga, R. Velotta, R. Capparelli, QCM-based immunosensor for rapid detection of *Salmonella Typhimurium* in food, *Sci. Rep.* 8 (2018). <https://doi.org/10.1038/s41598-018-34285-y>.
- [110] V. Abhilash, N. Rajender, K. Suresh, X-ray diffraction spectroscopy of polymer nanocomposites, in: S. Thomas, D. Rouxel, D. Ponnamma (Eds.), *Spectrosc. Polym. Nanocomposites*, William Andrew Publishing, 2016: pp. 410–451.

<https://doi.org/10.1016/B978-0-323-40183-8.00014-8>.

- [111] K.H. Pham, T.T. Thuy Giap, The liquid–amorphous phase transition, slow dynamics and dynamical heterogeneity for bulk iron: a molecular dynamics simulation, *RSC Adv.* 11 (2021) 32435–32445. <https://doi.org/10.1039/d1ra06394d>.
- [112] Z. Raza, B. Alling, I.A. Abrikosov, Computer simulations of glasses: The potential energy landscape, *J. Phys. Condens. Matter.* 27 (2015) 293201. <https://doi.org/10.1088/0953-8984/27/29/293201>.
- [113] D.M. Miskovic, K.J. Laws, M. Ferry, 9 - Metallic glasses, in: C. Wen (Ed.), *Struct. Biomater.*, Woodhead Publishing, 2021: pp. 275–300. <https://doi.org/https://doi.org/10.1016/B978-0-12-818831-6.00005-7>.
- [114] X. Guo, S. Gao, S. Sang, A. Jian, Q. Duan, J. Ji, W. Zhang, Detection system based on magnetoelastic sensor for classical swine fever virus, *Biosens. Bioelectron.* 82 (2016) 127–131. <https://doi.org/10.1016/j.bios.2016.03.067>.
- [115] E.M. Lifshitz, E. Kosevich, L.P. Pitaevskii, *Elastic Waves*, in: *Theory Elast.*, Third Edit, Butterworth-Heinemann, Oxford, 1986: pp. 87–107. <https://doi.org/10.1016/b978-0-08-057069-3.50010-3>.
- [116] F. Brailsford, *Applied Magnetism: A Study in Quantities*, in: *Electron. Power*, 1966: p. 368. <https://doi.org/10.1049/ep.1966.0297>.
- [117] G. Ausanio, V. Iannotti, L. Lanotte, Magnetoelastic stresses and strain sensors. In: *Encyclopedia of Sensors*, American Scientific Publishers, Valencia, 2006.
- [118] L. Lanotte, G. Ausanio, M. Carbuicchio, V. Iannotti, M. Muller, Coexistence of very soft magnetism and good magnetoelastic coupling in the amorphous alloy Fe<sub>62.5</sub>Co<sub>6</sub>Ni<sub>7.5</sub>Zr<sub>6</sub>Cu<sub>1</sub>Nb<sub>2</sub>B<sub>15</sub>, *J. Magn. Mater.* 215–216 (2000) 276–279. [https://doi.org/10.1016/S0304-8853\(00\)00133-5](https://doi.org/10.1016/S0304-8853(00)00133-5).
- [119] N.B. Ekreem, A.G. Olabi, T. Prescott, A. Rafferty, M.S.J. Hashmi, An overview of magnetostriction, its use and methods to measure these properties, *J. Mater. Process. Technol.* 191 (2007) 96–101. <https://doi.org/10.1016/j.jmatprotec.2007.03.064>.
- [120] C. Liang, S. Morshed, B.C. Prorok, Correction for longitudinal mode vibration in thin slender beams, *Appl. Phys. Lett.* 90 (2007) 221912. <https://doi.org/10.1063/1.2745262>.
- [121] A. Sagasti, J. Gutiérrez, A. Lasheras, J.M. Barandiarán, Size Dependence of the Magnetoelastic Properties of Metallic Glasses for Actuation Applications, *Sensors.* 19 (2019) 4296. <https://doi.org/10.3390/s19194296>.
- [122] C. Xue, C. Yang, T. Xu, J. Zhan, X. Li, A wireless bio-sensing microfluidic chip based on resonating “ $\mu$ -divers,” *Lab Chip.* 15 (2015) 2318–2326. <https://doi.org/10.1039/c5lc00361j>.

- [123] S. Huang, J. Hu, J. Wan, M.L. Johnson, H. Shu, B.A. Chin, The effect of annealing and gold deposition on the performance of magnetoelastic biosensors, *Mater. Sci. Eng. C.* 28 (2008) 380–386. <https://doi.org/10.1016/j.msec.2007.04.006>.
- [124] A.L. Possan, C. Menti, M. Beltrami, A.D. Santos, M. Roesch-Ely, F.P. Missell, Effect of surface roughness on performance of magnetoelastic biosensors for the detection of *Escherichia coli*, *Mater. Sci. Eng. C.* 58 (2016) 541–547. <https://doi.org/10.1016/j.msec.2015.08.029>.
- [125] M.J. Pollitt, G. Buckton, R. Piper, S. Brocchini, Measuring antibody coatings on gold nanoparticles by optical spectroscopy, *RSC Adv.* 5 (2015) 24521–24527. <https://doi.org/10.1039/C4RA15661G>.
- [126] W. Haiss, N.T.K. Thanh, J. Aveyard, D.G. Fernig, Determination of Size and Concentration of Gold Nanoparticles from UV–Vis Spectra, *Anal. Chem.* 79 (2007) 4215–4221. <https://doi.org/10.1021/ac0702084>.
- [127] J.A. Jargon, D.F. Williams, A. Sanders, The Relationship between Switch-Term-Corrected Scattering-Parameters and Wave-Parameters Measured with a Two-Port Vector Network Analyzer, *IEEE Microw. Wirel. Components Lett.* 28 (2018) 951–953. <https://doi.org/10.1109/LMWC.2018.2867076>.
- [128] H. Lin, Q. Lu, S. Ge, Q. Cai, C.A. Grimes, Detection of pathogen *Escherichia coli* O157:H7 with a wireless magnetoelastic-sensing device amplified by using chitosan-modified magnetic Fe<sub>3</sub>O<sub>4</sub> nanoparticles, *Sensors Actuators, B Chem.* 147 (2010) 343–349. <https://doi.org/10.1016/j.snb.2010.03.011>.
- [129] I. Langmuir, The adsorption of gases on plane surfaces of glass, mica and platinum, *J. Am. Chem. Soc.* 40 (1918) 1361–1403. <https://doi.org/10.1021/ja02242a004>.
- [130] P.E. Furlani, *Permanent Magnet and Electromechanical Devices*, Academic Press, New York, 1990.
- [131] G. Samourganidis, D. Kouzoudis, Characterization of magnetoelastic ribbons as vibration sensors based on the measured natural frequencies of a cantilever beam, *Sensors Actuators A Phys.* 301 (2020) 111711. <https://doi.org/10.1016/j.sna.2019.111711>.
- [132] W.Z. Shen, S. Cetinel, K. Sharma, E.R. Borujeny, C. Montemagno, Peptide-functionalized iron oxide magnetic nanoparticle for gold mining, *J. Nanoparticle Res.* 19 (2017). <https://doi.org/10.1007/s11051-017-3752-7>.
- [133] A. Einstein, On the Motion of Small Particles Suspended in a Stationary Liquid, *Ann. Phys.* 322 (1905) 549–560. <https://doi.org/10.1002/andp.19053220806>.
- [134] A.L. Valle, F.C.C. Mello, R.P. Alves-Balvedi, L.P. Rodrigues, L.R. Goulart, Glyphosate detection: methods, needs and challenges, *Environ. Chem. Lett.* 17 (2019) 291–317.

<https://doi.org/10.1007/s10311-018-0789-5>.

- [135] M. Kuster, M.L. de Alda, D. Barceló, Analysis of pesticides in water by liquid chromatography-tandem mass spectrometric techniques, *Mass Spectrom. Rev.* 25 (2006) 900–916. <https://doi.org/10.1002/mas.20093>.
- [136] M. Zourob, K.G. Ong, K. Zeng, F. Mouffouk, C.A. Grimes, A wireless magnetoelastic biosensor for the direct detection of organophosphorus pesticides, *Analyst.* 132 (2007) 338–343. <https://doi.org/10.1039/b616035b>.
- [137] S. Liu, Z. Zheng, X. Li, Advances in pesticide biosensors: current status, challenges, and future perspectives, *Anal. Bioanal. Chem.* 405 (2012) 63–90. <https://doi.org/10.1007/s00216-012-6299-6>.
- [138] T. Funke, H. Han, M.L. Healy-Fried, M. Fischer, E. Schönbrunn, Molecular basis for the herbicide resistance of Roundup Ready crops, *Proc. Natl. Acad. Sci. U. S. A.* 103 (2006) 13010–13015. <https://doi.org/10.1073/pnas.0603638103>.
- [139] H. Maeda, N. Dudareva, The Shikimate Pathway and Aromatic Amino Acid Biosynthesis in Plants, *Annu. Rev. Plant Biol.* 63 (2012) 73–105. <https://doi.org/10.1146/annurev-arplant-042811-105439>.
- [140] A.N. Steinrücken HC, The herbicide glyphosate is a potent inhibitor of 5-enolpyruvyl-shikimic acid-3-phosphate synthase, *Biochem. Biophys. Res. Commun.* (1980) 1207–1212.
- [141] European Commission, Status of glyphosate in the EU, (n.d.). [https://ec.europa.eu/food/plants/pesticides/approval-active-substances/renewal-approval/glyphosate\\_en](https://ec.europa.eu/food/plants/pesticides/approval-active-substances/renewal-approval/glyphosate_en).
- [142] L. Zhang, I. Rana, R.M. Shaffer, E. Taioli, L. Sheppard, Exposure to glyphosate-based herbicides and risk for non-Hodgkin lymphoma: A meta-analysis and supporting evidence, *Mutat. Res. - Rev. Mutat. Res.* 781 (2019) 186–206. <https://doi.org/10.1016/j.mrrev.2019.02.001>.
- [143] R. Mesnage, M. Teixeira, D. Mandrioli, L. Falcioni, Q.R. Ducarmon, R.D. Zwartink, F. Mazzacuva, A. Caldwell, J. Halket, C. Amiel, J.M. Panoff, F. Belpoggi, M.N. Antoniou, Use of shotgun metagenomics and metabolomics to evaluate the impact of glyphosate or roundup mon 52276 on the gut microbiota and serum metabolome of sprague-dawley rats, *Environ. Health Perspect.* 129 (2021) 1–15. <https://doi.org/10.1289/EHP6990>.
- [144] J. Hu, C. Lesseur, Y. Miao, F. Manservisi, S. Panzacchi, D. Mandrioli, F. Belpoggi, J. Chen, L. Petrick, Low-dose exposure of glyphosate-based herbicides disrupt the urine metabolome and its interaction with gut microbiota, *Sci. Rep.* 11 (2021) 1–10. <https://doi.org/10.1038/s41598-021-82552-2>.
- [145] G. Congur, Monitoring of glyphosate-DNA interaction and synergistic genotoxic effect of

- glyphosate and 2,4-dichlorophenoxyacetic acid using an electrochemical biosensor, *Environ. Pollut.* 271 (2021) 116360. <https://doi.org/10.1016/j.envpol.2020.116360>.
- [146] D.J. Hamilton, Á. Ambrus, R.M. Dieterle, A.S. Felsot, C.A. Harris, Regulatory Limits for Pesticide Residues in Water, *Chem. Int. -- Newsmag. IUPAC.* 25 (2003) 1123–1155. <https://doi.org/10.1515/ci.2003.25.6.21>.
- [147] J. Patsias, A. Papadopoulou, E. Papadopoulou-Mourkidou, Automated trace level determination of glyphosate and aminomethyl phosphonic acid in water by on-line anion-exchange solid-phase extraction followed by cation-exchange liquid chromatography and post-column derivatization, *J. Chromatogr. A.* 932 (2001) 83–90. [https://doi.org/10.1016/S0021-9673\(01\)01253-5](https://doi.org/10.1016/S0021-9673(01)01253-5).
- [148] A. Royer, S. Beguin, J.C. Tabet, S. Hulot, M.A. Reding, P.Y. Communal, Determination of glyphosate and aminomethylphosphonic acid residues in water by gas chromatography with tandem mass spectrometry after exchange ion resin purification and derivatization. Application on vegetable matrixes, *Anal. Chem.* 72 (2000) 3826–3832. <https://doi.org/10.1021/ac000041d>.
- [149] E. Mallat, D. Barceló, Analysis and degradation study of glyphosate and of aminomethylphosphonic acid in natural waters by means of polymeric and ion-exchange solid-phase extraction columns followed by ion chromatography-post-column derivatization with fluorescence detection, *J. Chromatogr. A.* 823 (1998) 129–136. [https://doi.org/10.1016/S0021-9673\(98\)00362-8](https://doi.org/10.1016/S0021-9673(98)00362-8).
- [150] M. Tsuji, Y. Akiyama, M. Yano, Simultaneous Determination of Glufosinate and Its Metabolite, and Glyphosate in Crops., *Anal. Sci.* 13 (1997) 283–285. <https://doi.org/10.2116/analsci.13.283>.
- [151] S.Y. Chang, C.H. Liao, Analysis of glyphosate, glufosinate and aminomethylphosphonic acid by capillary electrophoresis with indirect fluorescence detection, *J. Chromatogr. A.* 959 (2002) 309–315. [https://doi.org/10.1016/S0021-9673\(02\)00453-3](https://doi.org/10.1016/S0021-9673(02)00453-3).
- [152] Z.X. Guo, Q. Cai, Z. Yang, Determination of glyphosate and phosphate in water by ion chromatography - Inductively coupled plasma mass spectrometry detection, *J. Chromatogr. A.* 1100 (2005) 160–167. <https://doi.org/10.1016/j.chroma.2005.09.034>.
- [153] E.A. Hogendoorn, F.M. Ossendrijver, E. Dijkman, R.A. Baumann, Rapid determination of glyphosate in cereal samples by means of pre-column derivatisation with 9-fluorenylmethyl chloroformate and coupled-column liquid chromatography with fluorescence detection, *J. Chromatogr. A.* 833 (1999) 67–73. [https://doi.org/10.1016/S0021-9673\(98\)01055-3](https://doi.org/10.1016/S0021-9673(98)01055-3).
- [154] C.D. Stalikas, G.A. Pilidis, M.I. Karayannis, An integrated gas chromatographic method towards the simultaneous determination of phosphoric and amino acid group containing pesticides, *Chromatographia.* 51 (2000) 741–746. <https://doi.org/10.1007/BF02505414>.

- [155] K. Sato, J.Y. Jin, T. Takeuchi, T. Miwa, K. Suenami, Y. Takekoshi, S. Kanno, Integrated pulsed amperometric detection of glufosinate, bialaphos and glyphosate at gold electrodes in anion-exchange chromatography, *J. Chromatogr. A.* 919 (2001) 313–320. [https://doi.org/10.1016/S0021-9673\(01\)00843-3](https://doi.org/10.1016/S0021-9673(01)00843-3).
- [156] C.F.B. Coutinho, L.F.M. Coutinho, L.H. Mazo, S.L. Nixdorf, C.A.P. Camara, F.M. Lanças, Direct determination of glyphosate using hydrophilic interaction chromatography with coulometric detection at copper microelectrode, *Anal. Chim. Acta.* 592 (2007) 30–35. <https://doi.org/10.1016/j.aca.2007.04.003>.
- [157] L. Sun, D. Kong, W. Gu, X. Guo, W. Tao, Z. Shan, Y. Wang, N. Wang, Determination of glyphosate in soil/sludge by high performance liquid chromatography, *J. Chromatogr. A.* 1502 (2017) 8–13. <https://doi.org/10.1016/j.chroma.2017.04.018>.
- [158] M. Corbera, M. Hidalgo, V. Salvadó, P.P. Wiczorek, Determination of glyphosate and aminomethylphosphonic acid in natural water using the capillary electrophoresis combined with enrichment step, *Anal. Chim. Acta.* 540 (2005) 3–7. <https://doi.org/10.1016/j.aca.2004.12.028>.
- [159] L. Goodwin, J.R. Startin, B.J. Keely, D.M. Goodall, Analysis of glyphosate and glufosinate by capillary electrophoresis-mass spectrometry utilising a sheathless microelectrospray interface, *J. Chromatogr. A.* 1004 (2003) 107–119. [https://doi.org/10.1016/S0021-9673\(03\)00572-7](https://doi.org/10.1016/S0021-9673(03)00572-7).
- [160] S.L. Cahuantzi-Muñoz, M.A. González-Fuentes, L.A. Ortiz-Frade, E. Torres, Ş. Țălu, G. Trejo, A. Méndez-Albores, Electrochemical Biosensor for Sensitive Quantification of Glyphosate in Maize Kernels, *Electroanalysis.* 31 (2019) 927–935. <https://doi.org/10.1002/elan.201800759>.
- [161] V.N. Dhamu, S. Prasad, ElectrochemSENSE: A platform towards field deployable direct on-produce glyphosate detection, *Biosens. Bioelectron.* 170 (2020) 112609. <https://doi.org/10.1016/j.bios.2020.112609>.
- [162] V. Sok, A. Fragoso, Amperometric biosensor for glyphosate based on the inhibition of tyrosinase conjugated to carbon nano-onions in a chitosan matrix on a screen-printed electrode, *Microchim. Acta.* 186 (2019). <https://doi.org/10.1007/s00604-019-3672-6>.
- [163] H. Liu, P. Chen, Z. Liu, J. Liu, J. Yi, F. Xia, C. Zhou, Electrochemical luminescence sensor based on double suppression for highly sensitive detection of glyphosate, *Sensors Actuators, B Chem.* 304 (2020) 127364. <https://doi.org/10.1016/j.snb.2019.127364>.
- [164] E.C. Reynoso, E. Torres, F. Bettazzi, I. Palchetti, Trends and perspectives in immunosensors for determination of currently-used pesticides: The case of glyphosate, organophosphates, and neonicotinoids, *Biosensors.* 9 (2019) 20. <https://doi.org/10.3390/bios9010020>.
- [165] Q. Xiong, C.Y. Lim, J. Ren, J. Zhou, K. Pu, M.B. Chan-Park, H. Mao, Y.C. Lam, H. Duan,

- Magnetic nanochain integrated microfluidic biochips, *Nat. Commun.* 9 (2018) 1–11. <https://doi.org/10.1038/s41467-018-04172-1>.
- [166] W.H. Chong, Y. Huang, T.N. Wong, K.T. Ooi, G.P. Zhu, Magnetic Nanorobots, Generating Vortexes Inside Nanoliter Droplets for Effective Mixing, *Adv. Mater. Technol.* 3 (2018) 1–7. <https://doi.org/10.1002/admt.201700312>.
- [167] Q. Cao, Q. Fan, Q. Chen, C. Liu, X. Han, L. Li, Recent advances in manipulation of micro- and nano-objects with magnetic fields at small scales, *Mater. Horizons.* 7 (2020) 638–666. <https://doi.org/10.1039/c9mh00714h>.
- [168] M. Chang, J.L.F. Gabayno, R. Ye, K.W. Huang, Y.J. Chang, Mixing efficiency enhancing in micromixer by controlled magnetic stirring of Fe<sub>3</sub>O<sub>4</sub> nanomaterial, *Microsyst. Technol.* 23 (2017) 457–463. <https://doi.org/10.1007/s00542-016-3163-1>.
- [169] W.H. Chong, L.K. Chin, R.L.S. Tan, H. Wang, A.Q. Liu, H. Chen, Stirring in suspension: Nanometer-sized magnetic stir bars, *Angew. Chemie - Int. Ed.* 52 (2013) 8570–8573. <https://doi.org/10.1002/anie.201303249>.
- [170] X. Chen, L. Zhang, A review on micromixers actuated with magnetic nanomaterials, *Microchim. Acta.* 184 (2017) 3639–3649. <https://doi.org/10.1007/s00604-017-2462-2>.
- [171] R.M. Erb, J.J. Martin, R. Soheilian, C. Pan, J.R. Barber, Actuating Soft Matter with Magnetic Torque, *Adv. Funct. Mater.* 26 (2016) 3859–3880. <https://doi.org/10.1002/adfm.201504699>.
- [172] J.D. Jackson, *Classical Electrodynamics*, 3rd Edition, 1998.
- [173] S.A. Maier, *Plasmonics: Fundamentals and applications*, Springer US, New York, NY, 2007. <https://doi.org/10.1007/0-387-37825-1>.
- [174] C. Kittel, *Introduction to Solid State Physics Solution Manual*, 8th Edition, 2004.
- [175] P.A.D. Gonçalves, N.M.R. Peres, *An Introduction to Graphene Plasmonics*, WORLD SCIENTIFIC, 2016. <https://doi.org/10.1142/9948>.
- [176] V. Klimov, *Nanoplasmonics*, 2013. <https://doi.org/10.4032/9789814267427>.
- [177] H.C. van de Hulst, *Light Scattering by Small Particles*, Dover Publications, 1981.
- [178] Q. Fu, W. Sun, Mie theory for light scattering by a spherical particle in an absorbing medium, *Appl. Opt.* 40 (2001) 1354. <https://doi.org/10.1364/AO.40.001354>.
- [179] H. Chen, L. Shao, Q. Li, J. Wang, Gold nanorods and their plasmonic properties, *Chem. Soc. Rev.* 42 (2013) 2679–2724. <https://doi.org/10.1039/C2CS35367A>.
- [180] C.F. Bohren, D.R. Huffman, *Absorption and Scattering of Light by Small Particles*, Wiley, 1998. <https://doi.org/10.1002/9783527618156>.
- [181] A.J. Haes, S. Zou, G.C. Schatz, R.P. Van Duyne, Nanoscale optical biosensor: Short range distance dependence of the localized surface plasmon resonance of noble metal nanoparticles,

J. Phys. Chem. B. 108 (2004) 6961–6968. <https://doi.org/10.1021/jp036261n>.

- [182] A.J. Haes, S. Zou, G.C. Schatz, R.P. Van Duyne, A nanoscale optical biosensor: The long range distance dependence of the localized surface plasmon resonance of noble metal nanoparticles, J. Phys. Chem. B. 108 (2004) 109–116. <https://doi.org/10.1021/jp0361327>.
- [183] C.R. Yonzon, E. Jeoung, S. Zou, G.C. Schatz, M. Mrksich, R.P. Van Duyne, A comparative analysis of localized and propagating surface plasmon resonance sensors: The binding of Concanavalin A to a monosaccharide functionalized self-assembled monolayer, J. Am. Chem. Soc. 126 (2004) 12669–12676. <https://doi.org/10.1021/ja047118q>.
- [184] C.C. Chang, C.P. Chen, T.H. Wu, C.H. Yang, C.W. Lin, C.Y. Chen, Gold nanoparticle-based colorimetric strategies for chemical and biological sensing applications, Nanomaterials. 9 (2019) 1–24. <https://doi.org/10.3390/nano9060861>.
- [185] S. Moraes Silva, R. Tavallaie, L. Sandiford, R.D. Tilley, J.J. Gooding, Gold coated magnetic nanoparticles: from preparation to surface modification for analytical and biomedical applications, Chem. Commun. 52 (2016) 7528–7540. <https://doi.org/10.1039/C6CC03225G>.
- [186] A. Minopoli, B. Della Ventura, B. Lenyk, F. Gentile, J.A. Tanner, A. Offenhäusser, D. Mayer, R. Velotta, Ultrasensitive antibody-aptamer plasmonic biosensor for malaria biomarker detection in whole blood, Nat. Commun. 11 (2020) 6134. <https://doi.org/10.1038/s41467-020-19755-0>.
- [187] A. Minopoli, B. Della Ventura, R. Campanile, J.A. Tanner, A. Offenhäusser, D. Mayer, R. Velotta, Randomly positioned gold nanoparticles as fluorescence enhancers in apta-immunosensor for malaria test, Microchim. Acta. 188 (2021) 88. <https://doi.org/10.1007/s00604-021-04746-9>.
- [188] A. Minopoli, E. Scardapane, A. Acunzo, R. Campanile, B. Della Ventura, R. Velotta, Analysis of the optical response of a SARS-CoV-2-directed colorimetric immunosensor, AIP Adv. 11 (2021) 065319. <https://doi.org/10.1063/5.0050570>.
- [189] S. Goutelle, M. Maurin, F. Rougier, X. Barbaut, L. Bourguignon, M. Ducher, P. Maire, The Hill equation: A review of its capabilities in pharmacological modelling, Fundam. Clin. Pharmacol. 22 (2008) 633–648. <https://doi.org/10.1111/j.1472-8206.2008.00633.x>.
- [190] M. V. Khrolenko, P.P. Wiczorek, Determination of glyphosate and its metabolite aminomethylphosphonic acid in fruit juices using supported-liquid membrane preconcentration method with high-performance liquid chromatography and UV detection after derivatization with p-toluenesulphonyl chl, J. Chromatogr. A. 1093 (2005) 111–117. <https://doi.org/10.1016/j.chroma.2005.07.062>.
- [191] T. V. Nedelkoska, G.K.C. Low, High-performance liquid chromatographic determination of glyphosate in water and plant material after pre-column derivatisation with 9-fluorenylmethyl

chloroformate, *Anal. Chim. Acta.* 511 (2004) 145–153.  
<https://doi.org/10.1016/j.aca.2004.01.027>.

- [192] Y. Zhu, F. Zhang, C. Tong, W. Liu, Determination of glyphosate by ion chromatography, *J. Chromatogr. A.* 850 (1999) 297–301. [https://doi.org/10.1016/S0021-9673\(99\)00558-0](https://doi.org/10.1016/S0021-9673(99)00558-0).
- [193] J.S. Ridlen, G.J. Klopff, T.A. Nieman, Determination of glyphosate and related compounds using HPLC with tris(2,2'-bipyridyl)ruthenium(II) electrogenerated chemiluminescence detection, *Anal. Chim. Acta.* 341 (1997) 195–204. [https://doi.org/10.1016/S0003-2670\(96\)00493-X](https://doi.org/10.1016/S0003-2670(96)00493-X).
- [194] T. Guerrero-Esteban, C. Gutiérrez-Sánchez, E. Martínez-Periñán, M. Revenga-Parra, F. Pariente, E. Lorenzo, Sensitive glyphosate electrochemiluminescence immunosensor based on electrografted carbon nanodots, *Sensors Actuators, B Chem.* 330 (2021) 1–9. <https://doi.org/10.1016/j.snb.2020.129389>.
- [195] F. Bettazzi, A.R. Natale, E. Torres, I. Palchetti, Glyphosate determination by coupling an immuno-magnetic assay with electrochemical sensors, *Sensors (Switzerland)*. 18 (2018). <https://doi.org/10.3390/s18092965>.
- [196] J. Faraudo, J.S. Andreu, C. Calero, J. Camacho, Predicting the Self-Assembly of Superparamagnetic Colloids under Magnetic Fields, *Adv. Funct. Mater.* 26 (2016) 3837–3858. <https://doi.org/10.1002/adfm.201504839>.
- [197] S.L. Biswal, A.P. Gast, Rotational dynamics of semiflexible paramagnetic particle chains, *Phys. Rev. E - Stat. Physics, Plasmas, Fluids, Relat. Interdiscip. Top.* 69 (2004) 9. <https://doi.org/10.1103/PhysRevE.69.041406>.
- [198] M. Doi, S.F. Edwards, *The theory of polymer dynamics*, Oxford University Press, New York, 1986.
- [199] M. Li, G.W. Mulholland, M.R. Zachariah, Rotational diffusion coefficient (or rotational mobility) of a nanorod in the free-molecular regime, *Aerosol Sci. Technol.* 48 (2014) 139–141. <https://doi.org/10.1080/02786826.2013.864752>.
- [200] Z.M. Sherman, J.L. Pallone, R.M. Erb, J.W. Swan, Enhanced diffusion and magnetophoresis of paramagnetic colloidal particles in rotating magnetic fields, *Soft Matter*. 15 (2019) 6677–6689. <https://doi.org/10.1039/C9SM00890J>.
- [201] V. Arora, A. Sood, J. Shah, R.K. Kotnala, T.K. Jain, Synthesis and characterization of thiolated pectin stabilized gold coated magnetic nanoparticles, *Mater. Chem. Phys.* 173 (2016) 161–167. <https://doi.org/10.1016/j.matchemphys.2016.01.056>.
- [202] X. Zhang, N. Bao, X. Luo, S.N. Ding, Patchy gold coated Fe<sub>3</sub>O<sub>4</sub> nanospheres with enhanced catalytic activity applied for paper-based bipolar electrode-electrochemiluminescence aptasensors, *Biosens. Bioelectron.* 114 (2018) 44–51.

<https://doi.org/10.1016/j.bios.2018.05.016>.

- [203] H. Lai, W. Shang, Y. Yun, D. Chen, L. Wu, F. Xu, Uniform arrangement of gold nanoparticles on magnetic core particles with a metal-organic framework shell as a substrate for sensitive and reproducible SERS based assays: Application to the quantitation of Malachite Green and thiram, *Microchim. Acta.* 186 (2019). <https://doi.org/10.1007/s00604-019-3257-4>.
- [204] I.Y. Goon, L.M.H. Lai, M. Lim, P. Munroe, J.J. Gooding, R. Amal, Fabrication and dispersion of gold-shell-protected magnetite nanoparticles: Systematic control using polyethyleneimine, *Chem. Mater.* 21 (2009) 673–681. <https://doi.org/10.1021/cm8025329>.
- [205] L.E. Woodard, C.L. Dennis, J.A. Borchers, A. Attaluri, E. Velarde, C. Dawidczyk, P.C. Searson, M.G. Pomper, R. Ivkov, Nanoparticle architecture preserves magnetic properties during coating to enable robust multi-modal functionality, *Sci. Rep.* 8 (2018) 1–13. <https://doi.org/10.1038/s41598-018-29711-0>.
- [206] X. Luo, X. Zhao, G.Q. Wallace, M.H. Brunet, K.J. Wilkinson, P. Wu, C. Cai, C.G. Bazuin, J.F. Masson, Multiplexed SERS Detection of Microcystins with Aptamer-Driven Core-Satellite Assemblies, *ACS Appl. Mater. Interfaces.* 13 (2021) 6545–6556. <https://doi.org/10.1021/acsami.0c21493>.
- [207] H. Chen, H. Hu, C. Tao, R.M. Clauson, I. Moncion, X. Luan, S. Hwang, A. Sough, K. Sansanaphongpricha, J. Liao, H.J. Paholak, N.O. Stevers, G. Wang, B. Liu, D. Sun, Self-Assembled Au@Fe Core/Satellite Magnetic Nanoparticles for Versatile Biomolecule Functionalization, *ACS Appl. Mater. Interfaces.* 11 (2019) 23858–23869. <https://doi.org/10.1021/acsami.9b05544>.
- [208] A. Kostopoulou, K. Brintakis, M. Vasilakaki, K.N. Trohidou, A.P. Douvalis, A. Lascialfari, L. Manna, A. Lappas, Assembly-mediated interplay of dipolar interactions and surface spin disorder in colloidal maghemite nanoclusters, *Nanoscale.* 6 (2014) 3764–3776. <https://doi.org/10.1039/c3nr06103e>.
- [209] L. Lartigue, P. Hugounenq, D. Alloyeau, S.P. Clarke, M. Lévy, J.C. Bacri, R. Bazzi, D.F. Brougham, C. Wilhelm, F. Gazeau, Cooperative organization in iron oxide multi-core nanoparticles potentiates their efficiency as heating mediators and MRI contrast agents, *ACS Nano.* 6 (2012) 10935–10949. <https://doi.org/10.1021/nn304477s>.
- [210] D.L. Graham, H.A. Ferreira, P.P. Freitas, Magnetoresistive-based biosensors and biochips, *Trends Biotechnol.* 22 (2004) 455–462. <https://doi.org/10.1016/j.tibtech.2004.06.006>.
- [211] V.C. Martins, J. Germano, F.A. Cardoso, J. Loureiro, S. Cardoso, L. Sousa, M. Piedade, L.P. Fonseca, P.P. Freitas, Challenges and trends in the development of a magnetoresistive biochip portable platform, *J. Magn. Mater.* 322 (2010) 1655–1663. <https://doi.org/10.1016/j.jmmm.2009.02.141>.

- [212] J. Germano, T. Costa, F.A. Cardoso, J. Amaral, S. Cardoso, P.P. Freitas, M.S. Piedade, Electronic Platforms and Signal Processing for Magnetoresistive-Based Biochips, in: M. Sawan (Ed.), *Handb. Biochips*, Springer New York, New York, NY, 2017: pp. 1–39. [https://doi.org/10.1007/978-1-4614-6623-9\\_20-1](https://doi.org/10.1007/978-1-4614-6623-9_20-1).
- [213] A. Minopoli, B. Della Ventura, R. Campanile, J.A. Tanner, A. Offenhäusser, D. Mayer, R. Velotta, Randomly positioned gold nanoparticles as fluorescence enhancers in apta-immunosensor for malaria test, *Microchim. Acta.* 188 (2021) 88. <https://doi.org/10.1007/s00604-021-04746-9>.
- [214] A.C. Fernandes, C.M. Duarte, F.A. Cardoso, R. Bexiga, S. Cardoso, P.P. Freitas, Lab-on-chip cytometry based on magnetoresistive sensors for bacteria detection in milk, *Sensors (Switzerland)*. 14 (2014) 15496–15524. <https://doi.org/10.3390/s140815496>.
- [215] V.C. Romao, S.A.M. Martins, J. Germano, F.A. Cardoso, S. Cardoso, P.P. Freitas, Lab-on-Chip Devices: Gaining Ground Losing Size, *ACS Nano*. 11 (2017) 10659–10664. <https://doi.org/10.1021/acsnano.7b06703>.
- [216] V.C. Martins, F.A. Cardoso, J. Germano, S. Cardoso, L. Sousa, M. Piedade, P.P. Freitas, L.P. Fonseca, Femtomolar limit of detection with a magnetoresistive biochip, *Biosens. Bioelectron.* 24 (2009) 2690–2695. <https://doi.org/10.1016/j.bios.2009.01.040>.
- [217] G. Li, S. Sun, R.J. Wilson, R.L. White, N. Pourmand, S.X. Wang, Spin valve sensors for ultrasensitive detection of superparamagnetic nanoparticles for biological applications, *Sensors Actuators, A Phys.* 126 (2006) 98–106. <https://doi.org/10.1016/j.sna.2005.10.001>.
- [218] F.A. Cardoso, Design, optimization and integration of magnetoresistive biochips, Universidade Tecnica de Lisboa Instituto Superior Tecnico, 2011.
- [219] C. Tassa, S.Y. Shaw, R. Weissleder, Dextran-coated iron oxide nanoparticles: A versatile platform for targeted molecular imaging, molecular diagnostics, and therapy, *Acc. Chem. Res.* 44 (2011) 842–852. <https://doi.org/10.1021/ar200084x>.
- [220] V. Gehanno, P.P. Freitas, A. Veloso, J. Ferreira, B. Almeida, B. Sousa, A. Kling, M.F. Da Suva, Ion beam deposition of mn-ir spin valves, *IEEE Trans. Magn.* 35 (1999) 4361–4367. <https://doi.org/10.1109/20.799086>.
- [221] J. Germano, V.C. Martins, F.A. Cardoso, T.M. Almeida, L. Sousa, P.P. Freitas, M.S. Piedade, A portable and autonomous magnetic detection platform for biosensing, *Sensors*. 9 (2009) 4119–4137. <https://doi.org/10.3390/s90604119>.
- [222] W.M. Haynes, *CRC Handbook of Chemistry and Physics*, CRC Press, 2016.
- [223] A. Minopoli, A. Acunzo, B. Della Ventura, R. Velotta, Nanostructured Surfaces as Plasmonic Biosensors: A Review, *Adv. Mater. Interfaces*. n/a (n.d.) 2101133. <https://doi.org/https://doi.org/10.1002/admi.202101133>.

- [224] K.M.A. El-Nour, E.T.A. Salam, H.M. Soliman, A.S. Orabi, Gold Nanoparticles as a Direct and Rapid Sensor for Sensitive Analytical Detection of Biogenic Amines, *Nanoscale Res. Lett.* 12 (2017). <https://doi.org/10.1186/s11671-017-2014-z>.
- [225] I.Y. Tóth, D. Nesztor, L. Novák, E. Illés, M. Szekeres, T. Szabó, E. Tombácz, Clustering of carboxylated magnetite nanoparticles through polyethylenimine: Covalent versus electrostatic approach, *J. Magn. Magn. Mater.* 427 (2017) 280–288. <https://doi.org/10.1016/j.jmmm.2016.11.011>.
- [226] K. Saikia, D. Sen, S. Mazumder, P. Deb, Reassembling nanometric magnetic subunits into secondary nanostructures with controlled interparticle spacing, *RSC Adv.* 5 (2015) 694–705. <https://doi.org/10.1039/c4ra12115e>.
- [227] S. Bhattacharjee, Review article DLS and zeta potential – What they are and what they are not ?, *J. Control. Release.* 235 (2016) 337–351. <https://doi.org/10.1016/j.jconrel.2016.06.017>.
- [228] R. Tantra, P. Schulze, P. Quincey, Particuology Effect of nanoparticle concentration on zeta-potential measurement results and reproducibility, *Particuology.* 8 (2010) 279–285. <https://doi.org/10.1016/j.partic.2010.01.003>.
- [229] H. Zhou, J. Lee, T.J. Park, S.J. Lee, J.Y. Park, J. Lee, Ultrasensitive DNA monitoring by Au-Fe<sub>3</sub>O<sub>4</sub> nanocomplex, *Sensors Actuators, B Chem.* 163 (2012) 224–232. <https://doi.org/10.1016/j.snb.2012.01.040>.
- [230] I.Y. Goon, L.M.H. Lai, M. Lim, P. Munroe, J.J. Gooding, R. Amal, Fabrication and dispersion of gold-shell-protected magnetite nanoparticles: Systematic control using polyethyleneimine, *Chem. Mater.* 21 (2009) 673–681. <https://doi.org/10.1021/cm8025329>.